UNIVERSITY OF CALIFORNIA SAN DIEGO

Compositionally Complex Oxides For Energy Materials

A Dissertation submitted in partial satisfaction of the requirements
for the degree Doctor of Philosophy

in

Materials Science and Engineering

by

Dawei Zhang

Committee in charge:

Professor Jian Luo, Chair
Professor Renkun Chen
Professor Shyue Ping Ong
Professor Yu Qiao
Professor Kesong Yang

2023

The Dissertation of Dawei Zhang is approved, and it is acceptable in quality and form for publication on microfilm and electronically.

University of California San Diego

2023

DEDICATION

For my parents, Jie Zhang and Hongling Wang.

TABLE OF CONTENTS

LIST OF FIGURES

LIST OF TABLES

ACKNOWLEDGEMENTS

I received countless support throughout my PhD studies. First, I would like to thank my PhD advisor, Dr. Jian Luo, for his educational guidance on all my work. He provided me solid methodologies to investigate scientific questions and his kind and humble personality really impressed me throughout my whole PhD life. It was a great honor to work with and learn from him in the past four years. I would also like to thank my committee members, Dr. Renkun Chen, Dr. Shyue Ping Ong, Dr. Kesong Yang and Dr. Qiao Yu, for their valuable suggestions to improve my work.

Secondly, I would like to acknowledge my collaborators and co-authors, Dr. Wei Li, Dr. Yan Chen, Dr. Dunji Yu, Dr. An Ke, Dr. Joerg C. Neuefeind, Dr. Anthony H. McDaniel, Dr. Joshua D. Sugar, Dr. Jamie Trindell, Dr. Eric N. Coker, Dr. Yue Qi, Dr. Xingbo Liu, Hector A. De Santiago, Boyuan Xu, Jiyun Park and Cijie Liu with whom I had many valuable discussions.

I'm also grateful to my group members, Dr. Chongze Hu, Dr. Jiuyuan Nie, Dr. Andrew Wright, Dr. Qizhang Yan, Dr. Mingde Qin, Shu-Ting Ko, Keqi Song, Yi-Ting Yeh, Jingjing Yang, Jihong Min, Sashank Shivakumar, Yi Liu, Siyuan Shao and Heidy Vega, for the stimulating discussion and advice. I would like to thank other colleagues, Sicong Jiang, Hongpeng Gao and Yunxing Zuo, for their help and friendship.

Lastly and most importantly, I would like to thank my parents, Jie Zhang and Hongling Wang for their love, understanding and encouragement.

Chapter 1, in full, is a reprint of the materials as it appears in Chemistry of Materials 2023. D. Zhang, H. A. De Santiago, B. Xu, C. Liu, J. Trindell, W. Li, J. Park, M. A. Rodriguez, E. N. Coker, J. Sugar, A. McDaniel, S. Lany, L. Ma, Y. Wang, G. Collins, H. Tian, W. Li, Y. Qi, X. Liu and J. Luo. The dissertation author was the primary investigator and author of this paper.

Chapter 2, in full, is a reprint of the material as it appears in Dalton Transaction 2023. D. Zhang, J. Park, B. Xu, C. Liu, W. Li, X. Liu, Y. Qi and J. Luo. The dissertation author was the primary investigator and author of this paper.

Chapter 3, in full, is a reprint of the material as it appears in Advanced Powder Materials 2023. D. Zhang, Y. Chen, H. Vega, T. Feng, D. Yu, M. Everett, J. Neuefeind, K. An, R. Chen and J. Luo. The dissertation author was the primary investigator and author of this paper.

Chapter 4, in full, is a reprint of the material as it appears in Scripta Materials 2022. D. Zhang, Y. Chen, T. Feng, D. Yu, K. An, R. Chen and J. Luo. The dissertation author was the primary investigator and author of this paper.

VITA

2016 Bachelor of Science in Materials Science and Engineering, University of California Los Angeles

2018 Master of Science in Materials Science and Engineering, Stanford University

2023 Doctor of Philosophy in Materials Science and Engineering, University of California San Diego

PUBLICATIONS

1. D. Zhang, H. A. De Santiago, B. Xu, C. Liu, J. Trindell, W. Li, J. Park, M. A. Rodriguez, E. N. Coker, J. Sugar, A. McDaniel, S. Lany, L. Ma, Y. Wang, G. Collins, H. Tian, W. Li, Y. Qi, X. Liu and J. Luo. *Chem. Mater.*, 2023.

2. D. Zhang, J. Park, B. Xu, C. Liu, W. Li, X. Liu, Y. Qi and J. Luo, *Dalt. Trans*., 2023, 52, 1082–1088.

3. D. Zhang, Y. Chen, H. Vega, T. Feng, D. Yu, M. Everett, J. Neuefeind, K. An, R. Chen and J. Luo, *Adv. Powder Mater*., 2023, 2, 100098.

4. D. Zhang, Y. Chen, T. Feng, D. Yu, K. An, R. Chen and J. Luo, *Scr. Mater*., 2022, 215, 114699.

ABSTRACT OF THE DISSERTATION

Compositionally complex oxides for energy materials

by

Dawei Zhang

Doctor of Philosophy in Materials Science and Engineering

University of California San Diego, 2023

Professor Jian Luo, Chair

Solar thermochemical hydrogen (STCH) generation is a promising approach for eco-friendly H_2 production, but conventional STCH redox compounds cannot easily achieve desirable thermodynamic and kinetic properties and phase stability simultaneously due to a rather limited compositional space. Expanding from the nascent high-entropy ceramics field, this study explores a new class of compositionally complex perovskite oxides (CCPOs) $(La_{0.8}Sr_{0.2})(Mn_{(1-x)/3}Fe_{(1-x)/3}Co_xAl_{(1-x)/3})O_3$ with new non-equimolar designs for STCH. Entropy stabilization may contribute to the phase stability during

redox cycling without phase transformation, which enables STCH production for >50 cycles under harsh interrupted conditions.

Aliovalent doping on perovskite oxides can tune the oxygen vacancy formation energy. This work discovers normal *vs.* abnormal aliovalent doping effects on redox behaviors in medium-entropy compositionally complex perovskite oxides (CCPOs) $(La_{1-x}Sr_x)(Mn_{1/3}Fe_{1/3}Ti_{1/3})O_{3-\delta}$ (LS_MFT) *vs.* $(La_{1-x}Sr_x)(Mn_{1/3}Fe_{1/3}Cr_{1/3})O_{3-\delta}$ (LS_MFC). In the LS_MFC series, oxygen non-stoichiometry range $\Delta\delta$ ($= \delta_{red} - \delta_{ox}$) linearly depends on the Sr molar ratio *x*, while the LS_MFT series shows a V-shape dependence of $\Delta\delta$ on *x*. This unusual observation is investigated and explained based on the analysis of energy loss near edge structure (ELNES) in STEM electron energy loss spectroscopy, along with density functional theory (DFT) calculations. In LS_MFC, Cr-$L_{2,3}$, Mn-$L_{2,3}$ and Fe-$L_{2,3}$ peaks have a similar linear shift to higher energy with increasing *x*, which indicates higher oxidation states of Cr, Mn, and Fe with lower oxygen vacancy formation energies. In LS_MFT, the V-shape of $\Delta\delta$ *vs. x* curve is caused by the stable Ti^{4+} state and a V-shape Mn/Fe valency dependence on *x*. This study suggests the possible existence of different (including unexpected) coupled aliovalent doping effects in CCPOs with multiple B-site redox active elements.

Neutron diffraction and total scattering are combined to investigate a series of single-phase 10-component compositionally complex fluorite-based oxides, $[(Pr_{0.375}Nd_{0.375}Yb_{0.25})_2(Ti_{0.5}Hf_{0.25}Zr_{0.25})_2O_7]_{1-x}[(DyHoErNb)O_7]_x$, denoted as $10CCFBO_{xNb}$. A long-range order-disorder transition (ODT) occurs at $x = 0.81 \pm 0.01$ from the ordered pyrochlore to disordered defect fluorite. In contrast to ternary oxides, this ODT occurs abruptly without an observable two-phase region; moreover, the phase stability in 10CCFBOs deviates from the well-established criteria for simpler oxides. Rietveld refinements of neutron diffraction patterns suggest that this ODT occurs via the migration oxygen anions from the position 48*f* to 8*a*, with a small final jump at the ODT; however, the 8a oxygen occupancy changes gradually (without an observable discontinuous jump). We further discover diffuse scattering in Nb-rich compositions, which suggests the presence of short-range order. Using small-box modelling, four compositions near ODT ($x = 0.75$, 0.8, 0.85 and 1) can be better fitted by $C222_1$ weberite ordering for

the local polyhedral structure at nanoscale. Interestingly, $10CCFBO_{0.75Nb}$ and $10CCFBO_{0.8Nb}$ possess both long-range pyrochlore order and short-range weberite-type order, which can be understood from severe local distortion of the pyrochlore polyhedral structure. Thus, weberite-type short-range order emerges before the ODT, coexisting and interacting with long-range pyrochlore order. After the ODT, the long-range pyrochlore order vanishes but the short-range weberite-type order persists in the long-range disordered defect fluorite structure. Notably, a drop in the thermal conductivity coincides with emergence of the short-range order, instead of the long-range ODT.

Lastly, a redox induced pyrochlore to fluorite transition was discovered in $10CCFBO_{0.8Nb}$ via annealing in oxidized *vs.* reduced environments at 1600 °C. Notably, the 10-cation oxide remains a homogenous single-phase high-entropy solid solution before and after the ODT in the pyrochlore *vs.* fluorite structure that can be quenched. *In-situ* neutron diffraction reveals the oxygen vacancy formation and atomic displacement during this ODT. This study reveals a new pathway to induce ODT via a redox transition to tailor the properties of compositionally complex fluorite-based oxides.

INTRODUCTION

High-entropy ceramics (HECs) have been synthesized in several material families including rocksalt,[1,2] perovskite,[3] and fluorite[4–6] oxides, as well as other non-oxides such as borides,[7] carbides[8] and silicides.[9] Started from 2019, compositionally complex ceramics (CCCs) have been introduced to broaden the field of HECs by including non-equimolar compositions that reduce the configurational entropy but allow more engineering space to improve the properties.[10,11] However, the atomic level mechanisms of some physical properties, e.g., phase transformation in these many-component CCCs have not yet been fully investigated. Therefore, the development of solid methodologies to elucidate the related physical properties of the CCCs becomes a long-term scientific goal.

In **Chapter 1**, a new class of medium- to high-entropy CCPOs for two-step STCH with the chemical formula $(La_{0.8}Sr_{0.2})(Mn_{(1-x)/3}Fe_{(1-x)/3}Co_xAl_{(1-x)/3})O_3$ was designed. *In-situ* X-ray photoelectron spectroscopy shows preferential redox of Co. The extent of reduction increases, but the intrinsic kinetics decreases, with increasing Co content. Consequently, $(La_{0.8}Sr_{0.2})(Mn_{0.2}Fe_{0.2}Co_{0.4}Al_{0.2})O_3$ achieves an optimal thermodynamic and kinetic balance. The combination of a moderate enthalpy of reduction, a high entropy of reduction, and preferable surface oxygen exchange kinetics enables a maximum H_2 production of 89.97 mmol mol_{oxide}^{-1} in a short 1-hour redox duration. Entropy stabilization may contribute to the phase stability during redox cycling without phase transformation, which enables STCH production for >50 cycles under harsh interrupted conditions. The underlying redox mechanism is further elucidated by a density functional theory based parallel Monte Carlo computation approach.

In **Chapter 2**, two series of medium-entropy compositionally complex perovskite oxides (CCPOs) $(La_{1-x}Sr_x)(Mn_{1/3}Fe_{1/3}Cr_{1/3})O_3$ (denoted as "LS_MFC") and $(La_{1-x}Sr_x)(Mn_{1/3}Fe_{1/3}Ti_{1/3})O_3$ (denoted as "LS_MFT") were synthesized to investigate the aliovalent doping effect on oxygen vacancy formation, We discovered normal vs. abnormal behaviors in the reversible extent of reduction ($\Delta\delta$) *vs.* Sr molar ratio relations in LS_MFC (linear) and LS_MFT (V-shape). Combining the analysis of energy loss near edge structure (ELNES) in the electron energy loss spectra (EELS) in scanning transmission electron microscopy

(STEM) with density functional theory (DFT) calculations, we showed that the replacement of Ti with Cr alters the effect of Sr dopant due to the stable Ti^{4+} state. This new finding suggests that the simultaneous doping on A and B sites can have coupling effects, which can lead to both complexity and opportunities to tailor compositionally complex oxides with three or more primary redox active cations on one sublattice.

In **Chapter 3**, neutron diffraction and total scattering were used to characterize long- and short-range orders in 10-component compositionally complex ceramics. An unusual long-range order-disorder transition (ODT) from disordered defect fluorite to ordered pyrochlore occurs, which competes with emergence of weberite-type short-range ordering. Interestingly, reduced thermal conductivity coincides with the rise of short-range ordering, instead of occurrence of the long-range ODT.

In **Chapter 4**, we designed a 10-cation oxide $(Nd_{0.15}Pr_{0.15}Dy_{0.8}Ho_{0.8}Er_{0.8}Ti_{0.2}Yb_{0.1}Hf_{0.1}Zr_{0.1}Nb_{0.8})O_{7-\delta}$. This composition is obtained by mixing 20% of a compositionally complex pyrochlore oxide $[(Nd_{0.375}Pr_{0.375}Yb_{0.25})_2(Ti_{0.5}Hf_{0.25}Zr_{0.25})_2O_7]$ with 80% of a high-entropy (fluorite-structured) rare-earth niobate $[(DyHoErNb)O_7]$. The mixture forms a single-phase pyrochlore structure when it is synthesized in air, with the nominal formula: $(Pr_{0.075}Nd_{0.075}Dy_{0.4}Ho_{0.4}Er_{0.05})_2(Ti_{0.1}Zr_{0.05}Hf_{0.05}Nb_{0.4}Er_{0.35}Yb_{0.05})_2O_7$ (with smaller cations on the B sites, albeit anti-site defects; see Supplementary Discussion). We denote this 10-cation CCFBO as "$10CCFBO_{0.8Nb}$" for brevity, where the subscript denotes the Nb (or niobate) content. The composition of this $10CCFBO_{0.8Nb}$ is selected so that it is a barely ordered pyrochlore phase (as it would become a disordered defect fluorite structure in air if we further increased the Nb or fluorite-structured niobate content). This composition design enables us to explore a disordering transition induced by oxygen vacancy generation under a reduced environment, which has not been reported previously, to explore a new route to tailor the order/disorder and properties of CCFBOs (or CCCs in general).

CHAPTER 1. Compositionally Complex Perovskite Oxides for Solar Thermochemical Water Splitting

1.1 Introduction

Hydrogen has critical applications in modern industries and energy systems for future hydrogen economy.[12–16] To realize sustainable sunlight-driven water splitting and store the intermittent solar energy, two-step solar thermochemical hydrogen production (STCH) has attracted considerable attention due to its capability of utilizing the full solar spectrum energy to generate fuels.[17–22] The two-step STCH process involves an endothermic reduction step at a high temperature (≥1200 °C) under low oxygen partial pressure (P_{O_2}) with a suitable non-stoichiometric metal oxide to release oxygen and a subsequent oxidation step via flowing steam to the reduced oxide at a relatively lower temperature (~800–1100 °C). The most investigated non-stoichiometric metal oxide materials for STCH are undoped and doped ceria materials due to their phase stability and fast redox kinetics.[23–26] However, ceria ($CeO_{2-\delta}$, δ: oxygen non-stoichiometry) suffers from the requirement of extremely high reduction temperature (>1500 °C) to reach a small extent of reduction ($\Delta\delta \approx 0.03$-$0.06$), challenging the design of suitable reactors.[25,27] The perovskite oxides ($ABO_{3-\delta}$) are considered as a promising alternative candidate to ceria for STCH, as they have favorable merits including relative phase stability under large non-stoichiometry redox swing, tunable defect chemistry with A/B site doping, and a large compositional space.[28,29] For instance, $Ca(Ti_{0.5}Mn_{0.5})O_3$[30] and $(La_{1-x}Sr_x)(Mn_{1-y}Al_y)O_3$[31] perovskites have been investigated for STCH. Even though perovskites can have much larger redox capacities ($\Delta\delta > 0.15$), longer reaction time (total dwell time for reduction and oxidation steps > 2 h) is usually required to reach a fair H_2 production in the reports.[32–34] Understanding of the tradeoff between thermodynamic and kinetics properties is needed to optimize the perovskite composition to achieve high H_2 production within a short time (≤ 1h). Additionally, many reported perovskite oxides were found to show gradual phase transformation forming secondary phases with reduced or little redox capability in short-term

cycles,[32,35–45] which is detrimental to H_2 production cycling stability. Therefore, it is desirable to enhance the phase stability of perovskite oxides against thermochemical redox cycles.

High-entropy ceramics (HECs) have been synthesized in several material families including rocksalt,[1,2] perovskite,[3] and fluorite[4–6] oxides, as well as other non-oxides such as borides,[7] carbides[8] and silicides.[9] Notably, an equimolar poly-cation $(Fe_{0.25}Mg_{0.25}Co_{0.25}Ni_{0.25})O_x$ was reported for STCH undergoing reversible phase transformation between the spinel and rocksalt structure for 10 cycles.[46] However, the repetitive phase transformation is not desirable for long-term cycling stability, reversibility, and oxygen exchange kinetics due to its larger energy barrier. Fe was proposed as the redox active element, although the ex-situ characterization in that work may not precisely track the instantaneous redox change and the redox center valence may subject to change in the quenching/cooling process. It remains unclear why a particular cation dominates the redox chemistry and what factors govern the priority of redox behavior in the HECs during the STCH process. Recently, compositionally complex ceramics (CCCs) have been introduced to broaden the field of HECs by including non-equimolar compositions that reduce the configurational entropy but allow more engineering space to improve the properties.[10,11] CCCs can provide additional tunability of the physical properties *e.g.* thermomechanical properties in compositionally complex fluorite-based oxides.[47] Here, we hypothesize that a vast compositional space in compositionally complex perovskite oxides (CCPOs) will enable us to create a new class of stable STCH materials, where non-equimolar compositional designs can be leveraged to balance the thermodynamic and kinetic properties.

Herein, we designed a new class of medium- to high-entropy CCPOs for two-step STCH with the chemical formula $(La_{0.8}Sr_{0.2})(Mn_{(1-x)/3}Fe_{(1-x)/3}Co_xAl_{(1-x)/3})O_3$, denoted as "LS_MFC$_x$A" for brevity (Table 1.1). Unlike benchmark perovskite materials such as $La_{1-x}Sr_xCoO_3$[37,38,40,41] and $BaCe_xMn_{1-x}O_3$,[35] this LS_MFC$_x$A series of CCPOs did not show any phase transformation during the STCH redox cycling for $x < 0.61$ confirmed by the X-ray diffraction. In this series, the thermodynamic properties ($\Delta\delta$) are enhanced with the increasing Co content, whereas the intrinsic kinetic properties (oxygen surface exchange coefficient) are decreased with the increasing Co content. LS_MFC$_{0.4}$A ($(La_{0.8}Sr_{0.2})(Mn_{0.2}Fe_{0.2}Co_{0.4}Al_{0.2})O_3$)

showed the best balance between the thermodynamics and kinetics properties, rendering a high hydrogen production of 89.97 mmol mol_{oxide}^{-1} within a short 1 h duration at an optimized STCH condition. The in-situ X-ray photoelectron spectroscopy indicated that Co dominated the redox behavior. Furthermore, Monte Carlo (MC) sampling based on density functional theory (DFT) was applied in this field to demonstrate that oxygen vacancies prefer to form on the Co octahedron position among all B-site metal octahedron positions and the valence change of Co is the most obvious. Furthermore, we found that the Co-O bond in the CCPO is substantially weakened in comparison to both Mn-O, Al-O and Fe-O bonds in their respective simple perovskites, rationalizing the experimental observations. Moreover, LS_$MFC_{0.4}$A exhibited phase stability and moderate cycling durability even after 51 cycles under very harsh interrupted cycling conditions involving startup heating and shutdown cooling, which simulates the real-world day-night cycle conditions for STCH. This work opens up a new direction to explore novel CCCs for STCH and provides a new computation paradigm for mechanistic understanding of redox chemistries of STCH materials. The concept of design of CCCs may guide the future development of materials for other applications such as thermochemical looping, catalysis, and electrochemistry.

Table 1. 1 Compositions of CCPOs and abbreviations.

Sample Abbreviations	**Nominal Composition**	**Molecular Weight (mol g^{-1})**
LS_$MFC_{0.16}$A	$(La_{0.8}Sr_{0.2})(Mn_{0.28}Fe_{0.28}Co_{0.16}Al_{0.28})O_{3-\delta}$	224.65
LS_$MFC_{0.2}$A	$(La_{0.8}Sr_{0.2})(Mn_{0.267}Fe_{0.267}Co_{0.20}Al_{0.267})O_{3-\delta}$	225.22
LS_$MFC_{0.25}$A	$(La_{0.8}Sr_{0.2})(Mn_{0.25}Fe_{0.25}Co_{0.25}Al_{0.25})O_{3-\delta}$	225.82
LS_$MFC_{0.4}$A	$(La_{0.8}Sr_{0.2})(Mn_{0.2}Fe_{0.2}Co_{0.4}Al_{0.2})O_{3-\delta}$	227.78
LS_$MFC_{0.52}$A	$(La_{0.8}Sr_{0.2})(Mn_{0.16}Fe_{0.16}Co_{0.52}Al_{0.16})O_{3-\delta}$	229.34
LS_$MFC_{0.61}$A	$(La_{0.8}Sr_{0.2})(Mn_{0.13}Fe_{0.13}Co_{0.61}Al_{0.13})O_{3-\delta}$	230.51
LS_$MFC_{0.79}$A	$(La_{0.8}Sr_{0.2})(Mn_{0.07}Fe_{0.07}Co_{0.79}Al_{0.07})O_{3-\delta}$	232.85
LSC	$(La_{0.8}Sr_{0.2})CoO_3$	235.58

1.2 Experimental section

1.2.1 Material synthesis

The CCPO samples of LS_MFC$_x$A were prepared by solid-state reactions. The starting powders, La_2O_3 (99.99%), $SrCO_3$ (99.9%), MnO_2 (99.5%), Fe_2O_3 (99.99%), Co_3O_4 (99.9%) and Al_2O_3 (99.99%), were purchased from Alfa Aesar. The precursor powders were mixed based on the calculated stoichiometry and placed in a poly(methyl methacrylate) high-energy ball mill (HEBM) vial with endcaps and milling balls made by tungsten carbide. The vials were dry milled for 100 min (SPEX 8000D, SPEX SamplePrep, USA). Then, the mixed powder was annealed in air at 1300 °C for 10 hours to form the single perovskite phase. The synthesized powder was ground by pestle and mortar and further annealed in air at 1350 °C for another 10 hours to improve the homogeneity and single-phase purity of final products, similar to previous reports of solid-state synthesis of perovskite materials for STCH.[30,48] For all syntheses, the heating rate was 5 °C min^{-1} and natural furnace cooling (about 10 °C min^{-1}) was applied. In a typical synthesis batch, around 2 g of products were obtained.

1.2.2 Phase characterization

The phases were determined by X-ray diffraction (XRD) using Rigaku Miniflex with Cu Kα radiation with an operating voltage of 30 kV and a current of 15 mA. All XRD patterns were taken with 0.02° step size and 2 s dwell time. The Rietveld refinements were performed using GSAS-II software. The crystallographic information file (cif) of $LaAlO_3$ ($R\bar{3}c$) from Inorganic Crystal Structure Database (ICSD #92554) was used as a starting structure. In-situ high-temperature X-ray diffraction (HT-XRD) was performed on a Scintag PAD X powder X-ray diffractometer employing a sealed tube Cu Kα X-ray source, an incident beam mirror optic, fixed receiving slits and a Peltier-cooled germanium solid-state detector. The ancillary hot stage was a Buehler HTK 2400 furnace with a Pt/Rh heating strip and surround heater. The temperature of the hot stage was calibrated via thermal expansion of a known standard alumina material under similar testing conditions as the samples. Sample powders were ground under methanol and coated onto single crystal yttria stabilized zirconia (YSZ) substrates for loading onto the heating strip. Mass flow controllers provided controlled gas flow through the furnace chamber. The specimen in HT-XRD

experiments was heated up from room temperature to 1350 °C in flowing He and the spectra were recorded at different isotherm stages (about 30 min each) with an interval of 50 °C from 850 to 1350 °C. The isothermal duration at 1350 °C was 1 hour. The XRD patterns of cooling segments in flowing He were recorded at different isotherm stages of 1200, 1050, 900 and 800 °C (about 30 min each). Then, O_2 was introduced at 800 °C to oxidize the thermally reduced sample for 1 hour.

Scanning electron microscopy (SEM, FEI Apero) equipped with energy dispersive spectroscopy (EDS, Oxford N-MAX) were conducted to investigate the particle size, morphology, and elemental distributions. Nanoscale structure and elemental distribution were obtained by aberration-corrected scanning transmission electron microscopy (STEM, JEOL JEM-ARM300CF, Japan) with a high-angle annual dark field (HAADF) detector. The samples for STEM were prepared by a dual-beam focused ion beam (FIB, FEI Scios DualBeam, OR, USA).

1.2.3 Thermogravimetric analysis (TGA)

TGA was finished using a simultaneous thermal analyzer (NETZSCH STA 449 F3 Jupiter). For each test, 30 mg of sample was placed on an alumina crucible. The samples were heated up to 1350 °C with a 25 °C min^{-1} ramping rate and held isothermally for 45 min under ultra-high-purity (UHP) Ar. Then, the sample was cooled down to 1100 °C with the same ramp rate under Ar. Subsequently, 21 % O_2 balanced with Ar was introduced to re-oxidize the sample. The mass loss curves of samples were calibrated by a blank crucible run. The loss of mass was calculated to obtain the extent of reduction ($\Delta\delta=\delta_{re} - \delta_{ox}$) for all samples. The first cycle usually exhibited activation behaviors due to surface adsorption. Thus, we chose to report the TGA results in the stabilized second cycle for all LS_MFC$_x$A samples for consistent comparison. The plateau during the reoxidation step of the first cycle was considered as the reference (δ_{ox}) for calculating $\Delta\delta$.

1.2.4 In-situ X-ray photoelectron spectroscopy (XPS)

TGA was finished using a simultaneous thermal analyzer (NETZSCH STA 449 F3 Jupiter). For each test, 30 mg of sample was placed on an alumina crucible. The samples were heated up to 1350 °C with a 25 °C min^{-1} ramping rate and held isothermally for 45 min under ultra-high-purity (UHP) Ar. Then, the sample was cooled down to 1100 °C with the same ramp rate under Ar. Subsequently, 21 % O_2 balanced with Ar was introduced to re-oxidize the sample. The mass loss curves of samples were calibrated by a blank crucible run. The loss of mass was calculated to obtain the extent of reduction ($\Delta\delta=\delta_{re} - \delta_{ox}$) for all samples. The first cycle usually exhibited activation behaviors due to surface adsorption. Thus, we chose to report the TGA results in the stabilized second cycle for all LS_MFC$_x$A samples for consistent comparison. The plateau during the reoxidation step of the first cycle was considered as the reference (δ_{ox}) for calculating $\Delta\delta$.

1.2.5 Thermochemical water splitting

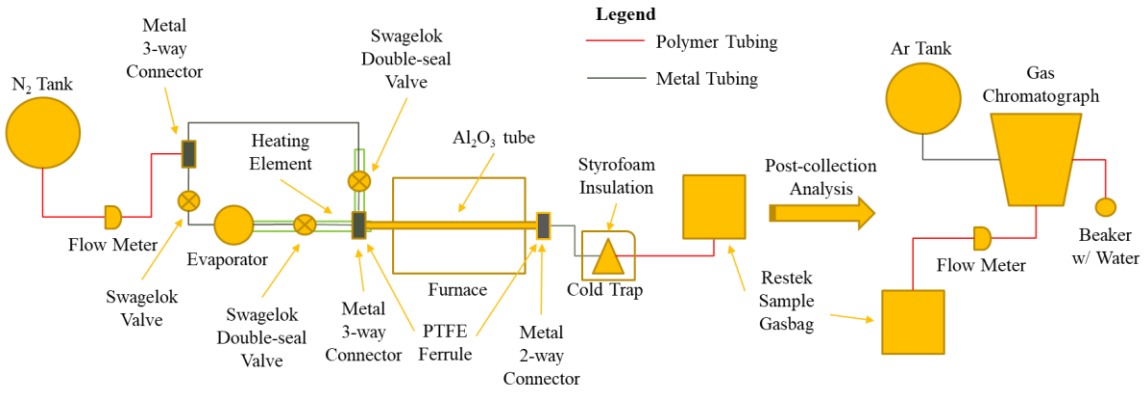

Figure 1. 1 Schematic of a home-made flow reactor for STCH production.

The STCH performances of materials were investigated using a homemade flow reactor (Figure 1.1). The powder (100 mg) was loaded into the middle point of a 24" alumina tube with an outer diameter of 1/4" and inner diameter of 3/16" and loaded horizontally close to the thermocouple within a high-temperature programmable electric furnace (Carbolite HTF 17/5). The powder was evenly dispersed inside the tube located in the center heating zone to ensure the sufficient gas-solid contact and mass transfer and there was

a void over the powder to avoid the sudden pressure drop and powder blowing off. N_2 (UHP, Matheson) was used as a carrier gas and the flow rate was controlled by a calibrated mass flow controller (Alicat Scientific). The steam (40 vol% H_2O) was generated using a water evaporator (humidity bottle, Fuel Cell Technologies, Inc.) with a target temperature of 85 ℃ and mixed with the N_2 gas by redirecting the flow of N_2 through a series of valves into the evaporator. The outlet was connected to a cold trap to condense and remove excess steam. To eliminate the inevitable errors of integrating the mass spectrometry response, the total H_2 production was collected with a gas sampling bag (Restek Multilayer Foil) for given time. The H_2 concentration was measured by gas chromatography (GC-2014, Shimadzu) which was calibrated by a series of standard calibration H_2 gases (GASCO, Cal Gas Direct Inc.) with different concentrations balanced by N_2. The reduction temperature was fixed at 1350 ℃. The oxidation temperatures were controlled at 800, 1000, 1100, and 1200 ℃. The gas flow rates were controlled at 100 or 200 sccm. Background H_2 production from catalytic water thermolysis at different temperatures was subtracted from the total H_2 production and only the H_2 production from the redox reaction was illustrated. To compare the kinetics and molar rate of gas production, some selected LS_MFC$_x$A compositions were tested in a stagnation flow reactor with mass spectrometry (MS) at Sandia National Laboratory (SNL). The oxygen uptake and release tests were also conducted at SNL. The testing condition has been described elsewhere.[31,35]

1.2.6 Electrical Conductivity Relaxation (ECR)

During ECR testing, the conductivity of the sample relaxes following a perturbation that alters its oxygen stoichiometry. In our case this perturbation is achieved through changes in p_{O_2}, with the transport of oxygen associated to this perturbation measured by monitoring the electrical conductivity as a function of time. The total transport of oxygen is described by the global transport parameters of oxygen chemical surface exchange coefficient (k_{ex}) and chemical diffusion coefficient (D), which can be obtained by fitting the solution of Fick's second law. The ratio of D to k_{ex} has been defined as characteristic thickness (l_c) and qualitatively describes the relative control of transport, either by the bulk diffusion or surface exchange. When normalized by membrane thickness d, the non-dimensional result indicates the primary source of transport resistance,

$$L = \frac{d}{l_c} = \frac{dk}{D} \tag{1.1}$$

For $0.1 < L < 10$, the oxygen transport process should be considered as a mixed control process. The in-depth discussion of the method and home-made setup for analyzing the relaxation profile has been described previously.[49]

The pellet samples for ECR were made using the synthesized powders. The powders were mixed with 3% PVB-ethanol solution in a 1:1 weight ratio and grinded until the ethanol evaporated, and the powder was thoroughly dried. Using a 20-mm die, the powders were axially pressed at 18,000 ft-lbs and sintered at 1350 ℃ in air for 4 hours, resulting in a plane disk. The pellets were then polished on both sides using a series of silicon carbide polishing papers and alumina suspension particles up to 0.3 μm in diameter on a fiber disk using a Buehler variable speed polisher. The bulk density of the sintered powder was calculated using the Archimedes method.

$$\rho_{bulk} = \frac{w_{dry} \times \rho_{liquid}}{\left(w_{closed} - w_{bouyant}\right)} \tag{1.2}$$

Thereafter, a bar was cut out of each pellet and platinum wire and paste were attached to each end of the bars to create terminals. The bars were then annealed at 1000 ℃ in air for 30 minutes to settle the platinum paste and create a good surface contact between the platinum wires and the bar.

1.2.7 Measurement of thermodynamic properties

The thermodynamic properties of the optimal composition, LS_$MFC_{0.4}$A was measured up to a maximum temperature of 1400 ℃ under six different pO_2 conditions ranging from 0.21–2.5×10^{-5} atm. Accordingly, ~300 mg of sample was loaded into the TGA chamber and pretreated at 1000 ℃ for 30 minutes under 21% O_2 balanced with UHP Ar with a heating and cooling rate of 30 K min^{-1} to remove any surface adsorbates from the sample. After the treatment, the temperature returned to 80 ℃. Then, the sample was heated to the reference temperature of 1000 ℃ under 0.028 atm at a heating rate of 5 K min^{-1} and kept at 1000 ℃ for 1 h to equilibrate the sample. Then, either a continuous or stepwise procedure was used for high P_{O_2} and low P_{O_2} conditions, respectively. The continuous conditions were performed for $P_{O_2} \geq 0.028$ atm. Accordingly, the P_{O_2} was adjusted to the targeted value and the temperature was heated to 1400 ℃,

kept at 1400 ℃ for 1 h, cooled to 300 ℃ and maintained at 300 ℃ for 1 hour. Then, it was heated again to 1400 ℃ and kept under isothermal conditions for 1 h. The heating and cooling were under a heating/cooling rate of 2 K min^{-1}. Thereafter, the temperature was cooled to the reference temperature of 1000 ℃ at 5 K min^{-1} under the reference P_{O_2} of 0.028 atm and held at 1000 ℃ for 1 h to confirm if the equilibrium values between the two reference points were kept at the similar level. The stepwise conditions were performed for $P_{O_2} \leq 1.70 \times 10^{-3}$ atm. Accordingly, the P_{O_2} was adjusted to the targeted value, and the temperature was increased to the initial testing condition at a ramp rate of 2 K min^{-1} and kept isothermally for 1–2 h until the sample was stabilized. Thereafter, the sample was treated in various isothermal conditions for 1–2 h with a temperature interval of 100 ℃. The tested isothermal temperatures depended on the P_{O_2} up to 1400 ℃. Thereafter, the temperature was cooled to the reference temperature of 1000 ℃ a 5 K min^{-1} under the reference P_{O_2} of 0.028 atm and held at 1000 ℃ for 1 h to confirm if the equilibrium values between the two reference points were kept at the similar level. The thermodynamic limit of equilibrium H_2 production was calculated using the obtained results (oxygen non-stoichiometry of LS_$MFC_{0.4}$A as a function of temperature and P_{O_2}) through an established method.[30,50,51] The thermodynamic limit of equilibrium H_2 production of LS_$MFC_{0.4}$A comes from the equilibrium change of $\Delta\delta = \delta_{re} - \delta_{ox,}$ where δ_{re} and δ_{ox} represent the equilibrium δ values of thermochemical reduction (1350 ºC under inert gas with 25 ppm P_{O_2}) and oxidative water splitting (1100 ºC under 40 vol% H_2O balanced with inert gas), respectively.

1.2.8 Monte Carlo (MC) and density functional theory (DFT) calculations

To sample the massive structural space of compositional complex perovskite oxides, we performed a density functional theory (DFT) based parallel Monte Carlo (MC) study for both LS_MFCA bulk and vacancy configurations to investigate the reduction mechanism. Four major initial perovskite structures, with space groups of *Pnma*, $R\bar{3}c$ and $Pm\bar{3}m$ as base structures, were used to generate randomly mixed 80-atom $(La_{0.75}Sr_{0.25})(Mn_{0.25}Fe_{0.25}Co_{0.25}Al_{0.25})O_3$ supercells (as the "seed"). Vacancy supercells were created by removing one of each nonequivalent oxygen from base structures before the cations were randomly

mixed. 10 seed structures were generated for each symmetry. The MC workflow was built upon a framework developed for crystal structure prediction.[52] Each seed structure was evolved following a Monte Carlo "path", by first randomly switching the position or the magnetic moment of the two A-site elements or/and two out of the four B-site elements, relaxing with DFT calculations, and applying the Metropolis Monte Carlo acceptance criterion at 1600 K with the DFT computed energies. Here, 2600 accepted bulk and 3000 vacancy structures were saved and used for the analysis.

DFT calculations were performed using the Projector Augmented Wave (PAW) method[53] implemented in the Vienna Ab initio Simulation Package (VASP). The generalized gradient approximation of Perdew, Burke, and Ernzerhof (PBE)[54] was used for the DFT exchange correlation functional. Hubbard U correction for 3d transition metal electrons was chosen to be 3.0 eV, and that for La 5*d* electrons was set to be 1.5 eV with an additional value for 4*f* electrons set to be 2.0 eV. The plane-wave cutoff energy was set to 320 eV, which is sufficient for the soft O pseudopotential, with a $2 \times 2 \times 2$ Gamma point Monkhorst-Pack k-point meshes. Initial magnetic moments are selected randomly to be half up and half down for {B} site elements. The electronic and atomic relaxation convergence criteria were 8×10^{-5} and 0.04 eV $Å^{-1}$, respectively. These settings provide a reasonable compromise between accuracy and efficiency for the large number of MC trial calculations.

Table 1. 2 Tabulated values for R_0 and b for both experimental and DFT calculated BVS

Experimental BVS values are from the ICSD reported high-quality structures. The DFT calculated BVS values are from GGA+U results. Low spin $LaCoO_3$ is selected as the ground state for Co^{3+}.

Cation	Anion	R_0	b	Compound	BVS (Exp.)	BVS (DFT)
Mn^{4+}	O^{2-}	1.750	0.374	$SrMnO_3$	4.036	3.715
Fe^{3+}	O^{2-}	1.766	0.360	$LaFeO_3$	3.051	2.850
Co^{3+}	O^{2-}	1.655	0.364	$LaCoO_3$	2.819	2.661
Al^{3+}	O^{2-}	1.634	0.390	$LaAlO_3$	3.090	2.882

A descriptor called Bond Valence Sum (BVS) developed by Brown and Shannon was adopted to analyze the relation between bond strength and bond length.[55] Note that the BVS values of the single

components from the DFT calculation with generalized gradient approximation (GGA) functionals are consistently lower than the experimental BVS, due to GGA+U method underbinding the structure.[55,56] We focused on the comparison of DFT-computed bond valence sum (BVS) between the single components ($SrMnO_3$, $LaFeO_3$, $LaCoO_3$, and $LaAlO_3$) and $(La_{0.75}Sr_{0.25})(Mn_{0.25}Fe_{0.25}Co_{0.25}Al_{0.25})O_3$ under the similar calculation conditions. The expression for a B element's Bond Valence Sum is defined as:

$$V = \sum_i exp\left(\frac{R_0 - R_i}{b}\right) \tag{1.3}$$

where R_0 and b are tabulated parameters from experiment (Table 1.2), R_i is corresponding B-O bond length, and the sum goes over all six B-O bonds for a B centered octahedron. The Bond Valence theory predicts an outcome that is close to oxidation state.

Local bond distortion occurs in compositionally complex materials and it can be measured by a discrepancy factor d:[56]

$$d_i = V_i - Z_i \tag{1.4}$$

where V_i is the BVS value for ion i, and Z_i is the oxidation number for ion i (positive for cation, negative for anion). A positive d_i represents a compression of ion surrounding bonds, while a negative one stands for stretching.

Furthermore, global instability index G,[56] the root-mean-square value of the discrepancy factors over the whole system that quantifies the strain experienced by the structure as a whole, is defined as:

$$G = \left(\frac{\sum_i {d_i}^2}{N}\right)^{\frac{1}{2}} \tag{1.5}$$

1.3 Results and Discussion

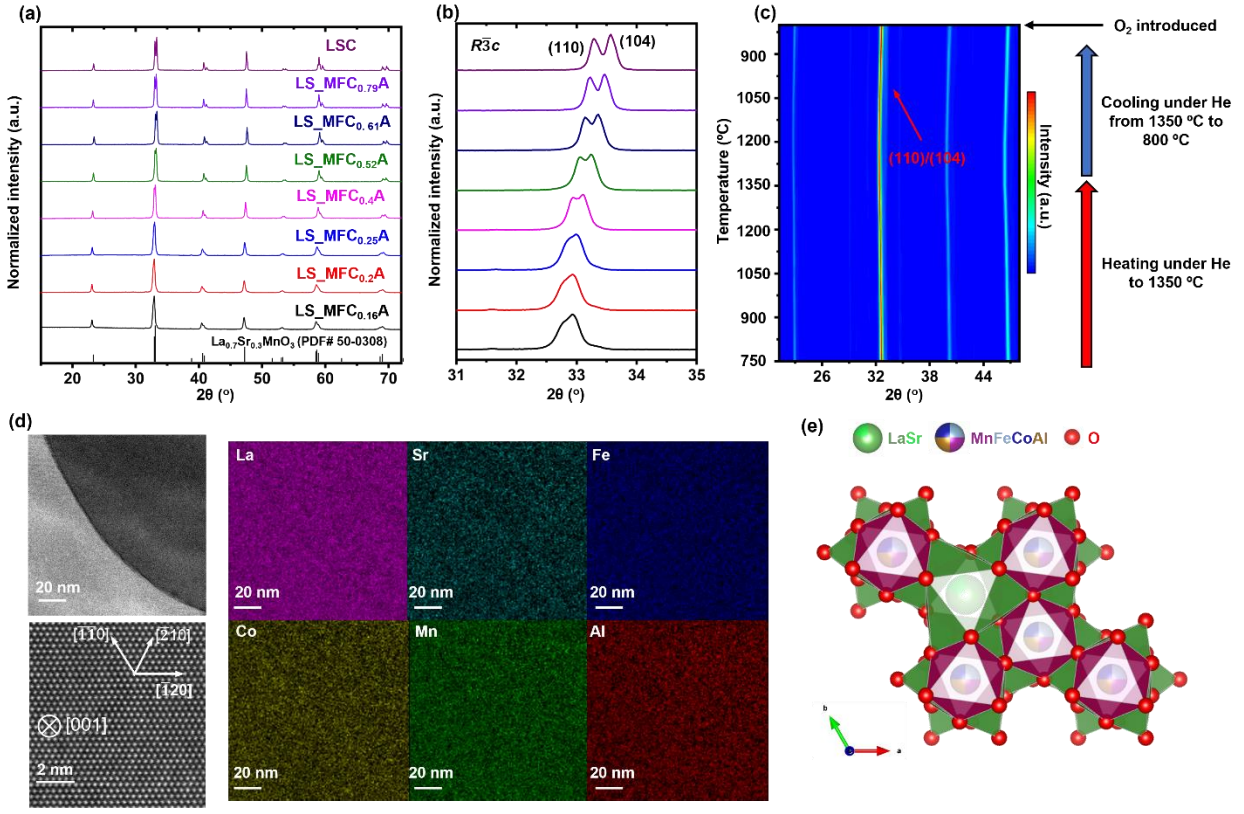

Figure 1. 2 Phase and structural characterization of LS_MFC$_x$A by XRD and STEM-EDS
(a) XRD patterns of LS_MFC$_x$A (x = 0.16, 0.2, 0.25, 0.4, 0.52, 0.61, 0.79, and 1). (b) The splitting of (110) and (104) peaks showing the $R\bar{3}c$ rhombohedral structure. (c) HT-XRD pattern of LS_MFC$_{0.16}$A. The sample was heated from room temperature to 1350 °C under a He flow. There was no phase transformation or separation occurring in LS_MFC$_{0.16}$A under thermally reduced and oxidation conditions. (d) STEM HAADF images of LS_MFC$_{0.25}$A (with a grain boundary) and its nanoscale EDS elemental maps. (e) Schematic illustration of the corresponding crystal structure of LS_MFC$_{0.25}$A.

The XRD pattern (Figure 1.2a) reveals that LS_MFC$_x$A adopted a rhombohedral structure ($R\bar{3}c$), with the peak splitting at 2θ of 32.8° (Figure 1.2b). Rietveld refinements confirm the $R\bar{3}c$ phase for all compositions by assuming random B site occupation of Mn, Fe, Co, and Al (Figure 1.3). As the Co content increases in LS_MFC$_x$A, the diffraction peaks gradually shift to higher 2θ angle indicating the decrease of lattice parameters, which is ascribed to the smaller ionic radius of Co^{3+} (0.545 Å) compared to an average ionic radius of other B site elements (0.553 Å),[32,57] and peak splitting becomes larger. To probe the phase stability of LS_MFC$_x$A under thermally reducing environments, LS_MFC$_{0.16}$A was selected to perform HT-XRD. Figure 1.2c displays that LS_MFC$_{0.16}$A showed phase stability at 1350 °C and maintained the $R\bar{3}c$

rhombohedral structure without phase transition under the reducing conditions, except for the slight peak shifts (lattice expansion) due to the thermal expansion and oxygen loss.[58–60] After the O_2 uptake at 800 °C, the lattice was recovered to the initial state. The atomic structure and elemental distribution of LS_MF$C_{0.25}$A were characterized by the scanning transmission electron microscopy (STEM) high-angle annular dark field (HAADF) imaging with the energy dispersive spectroscopy (EDS) (Figure 1.2d), which suggested a homogenous elemental distribution of cation elements. The XRD and EDS mapping results indicate a long-range random B site occupation. The schematic structure was shown in Figure 1.2e.

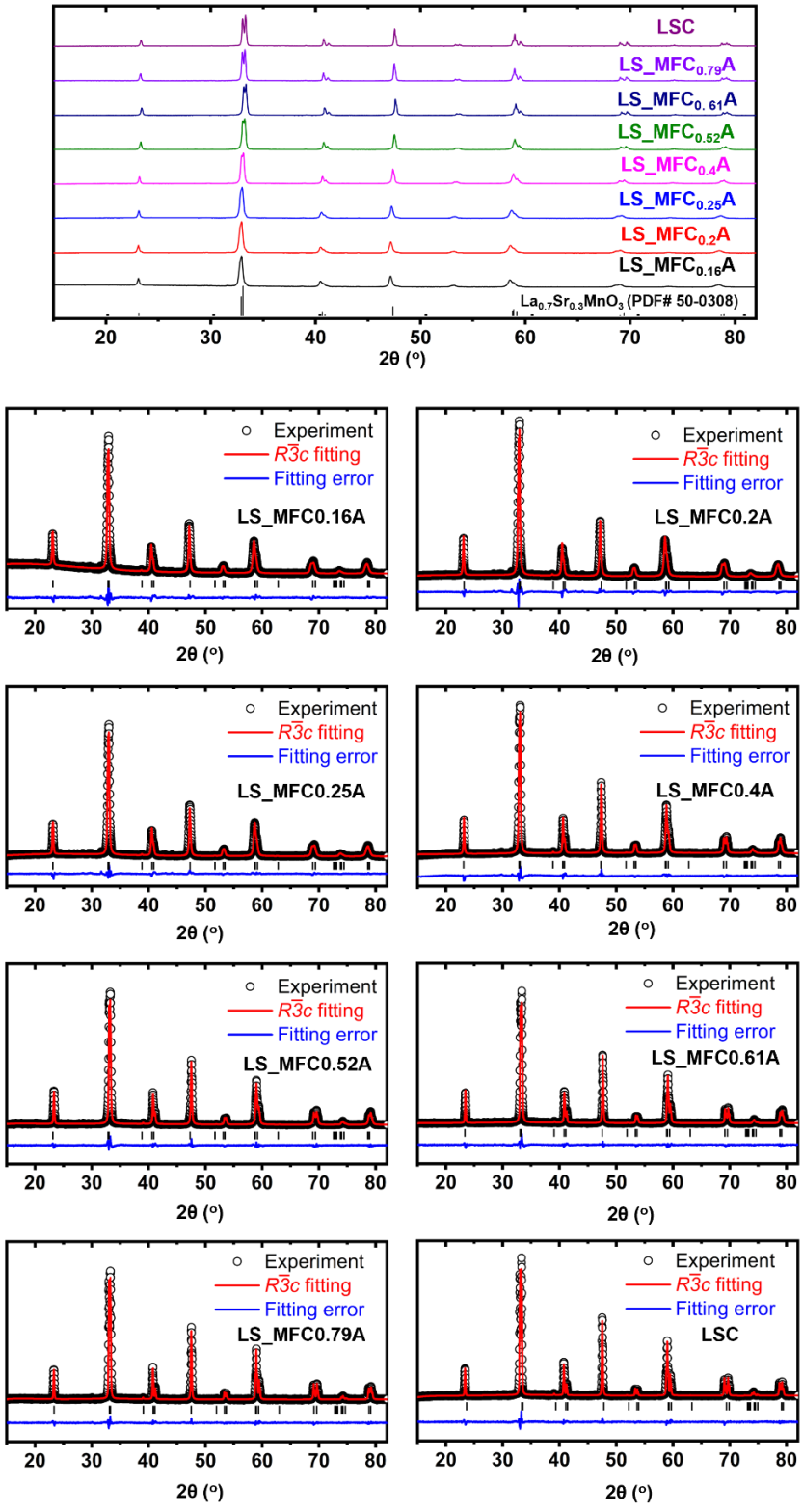

Figure 1. 3 Rietveld refinements of XRD patterns of all synthesized LS_MFC$_x$A

To quantify the redox capability, LS_MFC$_x$A samples were tested by TGA.[61] The reversible extent of reduction ($\Delta\delta$) displays a decreasing trend with narrower temperature swing (Figure 1.4). The reduction reaction is endothermic which is thermodynamically favored at a high temperature, while the oxidation reaction is exothermic that is thermodynamically favored at a low temperature (but it may be not kinetically favored at a very low temperature). Therefore, a wider temperature swing is a favorable driving force to enhance the reversible $\Delta\delta$.

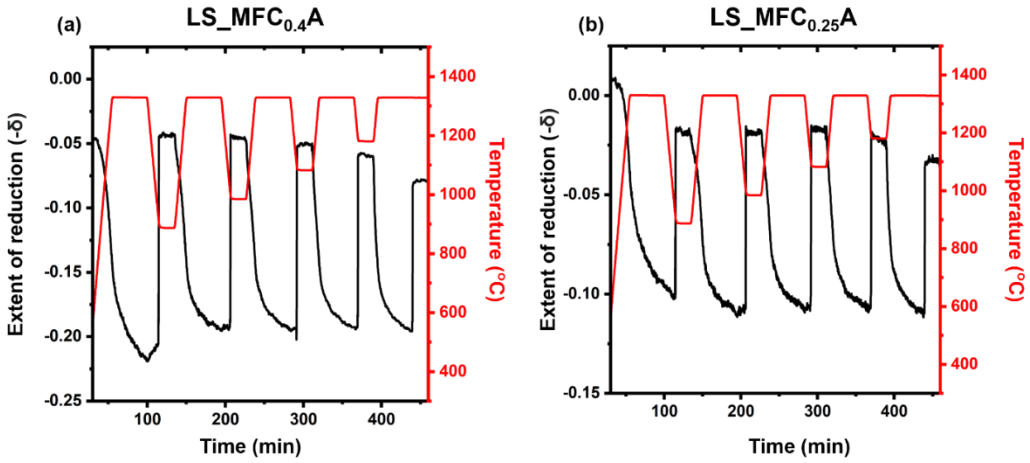

Figure 1. 4 Oxygen non-stoichiometry of LS_MFCA and LS_MFCA under different temperature swings. TGA measurements of (a) LS_MFC$_{0.4}$A and (b) LS_MFC$_{0.25}$A with different oxidation temperatures (900, 1000, 1100, 1200, and 1350 °C). The reduction temperature was fixed at 1350 °C.

The TGA experiments (Figure 1.5a) show that $\Delta\delta$ monotonically increases with the molar fraction of Co in the B site of LS_MFC$_x$A (Figure 1.5b). The endmember of simple perovskite LSC can greatly be reduced with $\Delta\delta = 0.37$ compared to LS_MFC$_{0.16}$A with the smallest $\Delta\delta = 0.06$. When $x \leq 0.52$, the reduced samples were fully re-oxidized under 21% O_2 environment in 1–2 seconds. In contrast, when x was increased beyond ~0.61, the samples underwent a sluggish reoxidation process and could not be recovered to a full oxidation state within 25 min under 21% O_2. The low reoxidation rate under a high P_{O_2} of 21% indicates that the driving force for reoxidation can be a limited factor for these compositions (LS_MFC$_x$A, $x \geq 0.61$). Moreover, the incomplete reoxidation process observed in LS_MFC$_x$A ($x \geq 0.61$) also implies a

potential irreversible phase transformation or secondary phase precipitation during the redox cycling. The XRD patterns for LS_MFC$_x$A before and after the TGA measurements were compared (Figure 1.5c and d). A Co-enriched Ruddlesden-Popper (RP) La_2CoO_4 secondary phase was formed in LS_MFC$_{0.61}$A, LS_MFC$_{0.79}$A and LSC, consistent with the reported poor phase stability of $La_{1-x}Sr_xCoO_3$.[37,38,40,41]

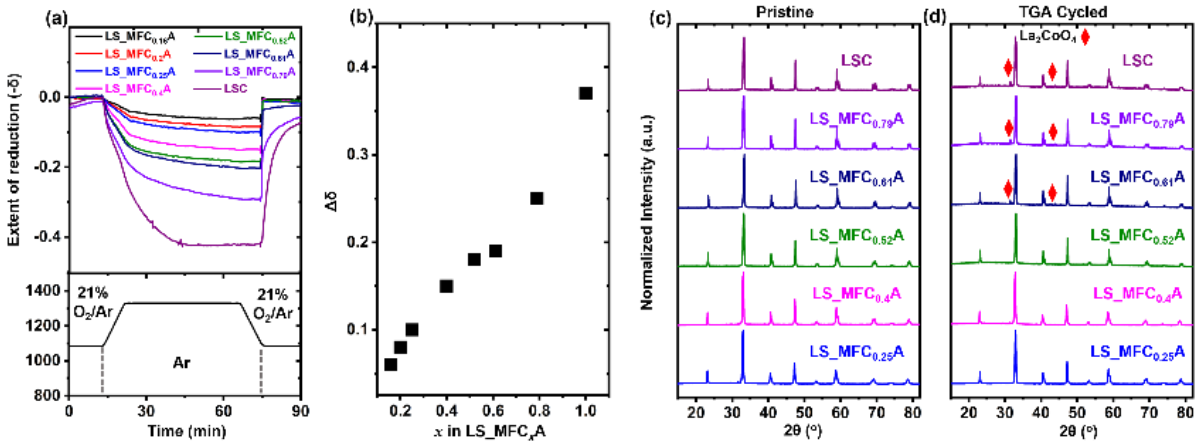

Figure 1. 5 TGA tests of the extent reduction of all LS_MFCA and phase stability measurements
(a) TGA tests of the LS_MFC$_x$A with x ranging from 0.16 to 1 to evaluate the extent of reduction (formation of oxygen vacancies) at 1350 °C for 45 min in Ar and reoxidation at 1100 °C in 21% O_2 balanced with Ar. (b) The correlation of $\Delta\delta$ with x in LS_MFC$_x$A. Comparison of XRD patterns before (c) and after (d) TGA experiments. La_2CoO_4 secondary phase formed in LS_MFC$_x$A ($x \geq 0.61$).

In addition, many other perovskite oxides have been reported to demonstrate phase transformation and even serious decomposition after a thermochemical redox process, including $BaCe_{0.25}Mn_{0.75}O_3$,[35,41,45] $Gd_{0.5}La_{0.5}Co_{0.5}Fe_{0.5}O_3$,[36] $La_{0.8}Sr_{0.2}MeO_3$ (Me=Co, Ni and Cu),[39] $La_{0.6}Ca_{0.4}CoO_3$,[42] $Y_{0.8}Sr_{0.2}Mn_{0.6}Al_{0.4}O_3$ and $Y_{0.8}Sr_{0.2}MnO_3$,[44] $LaGa_{1-y}Co_yO_{3-\delta}$ ($y \geq 0.1$) and $La_{1-x}Sr_xGa_{0.5}Co_{0.5}O_{3-\delta}$ ($x = 0$–0.5).[32] In contrast, LS_MFC$_x$A ($x \leq 0.52$) showed no detectable secondary phase in the XRD patterns and displayed rapid and complete reoxidation. Therefore, the phase stability and redox reversibility of LS_MFC$_x$A ($x \leq 0.52$) make them suitable for STCH. Besides Co, we also tuned other B site elements deviating from the equimolar composition or varied the fractions of Mn, Fe and Al but fixing Co fraction and measured their TGA results (Figure 1.6), which suggested that the Co content demonstrated the most significant influence on the extent of reduction compared to other B site elements.

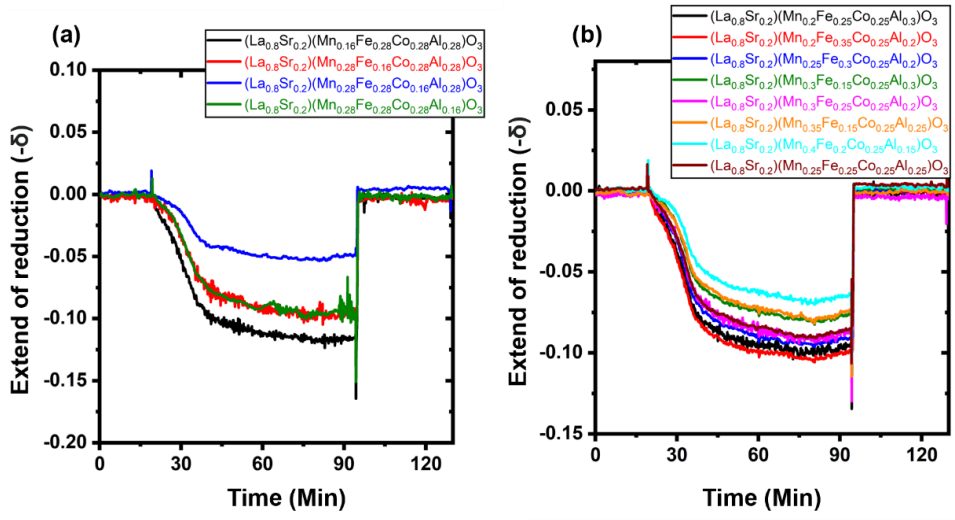

Figure 1. 6 TGA measurement of a set of non-equal molar specimens
(a) TGA measurements of a set of specimens where each B site element was away from equal molar. (b) TGA measurements of a set of specimens with fixed Co fraction but varied (non-equimolar) Mn, Fe and Al fractions. The reduction was conducted at 1350 °C under Ar and oxidation was conducted at 900 °C under 21% O_2 balanced with Ar.

To further confirm the redox sequence of B-site elements in the LS_MFC$_x$A, the in-situ XPS was conducted to study the redox behavior of all cations by heating LS_MFC$_{0.25}$A to 800 °C (XPS heating limit) under vacuum (Figure 1.7a). The high-resolution XPS spectra of all cations at 25 and 800 °C are shown in Figure 1.7b-g. LS_MFC$_{0.25}$A showed a measurable $\Delta\delta$ of 0.03 at 800 °C (Figure 1.8). For the A-site elements, the left peak area of La $3d_{5/2}$ slightly increased indicating pyrolysis of the surface absorbed $La(OH)_3$ species at 800 °C.

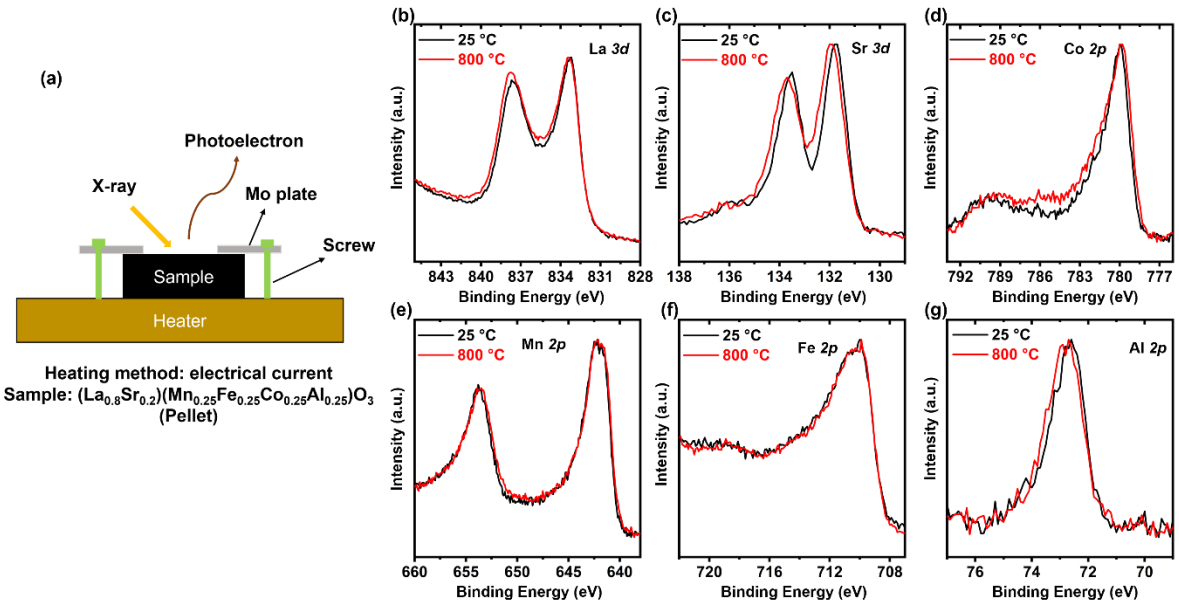

Figure 1. 7 *In-situ* XPS measurements of LS_$MFC_{0.25}$A
(a) Schematic of the in situ XPS set-up and the normalized (b) La 3d, (c) Sr 3d, (d) Co 2p, (e) Mn 2p, (f) Fe 2p and (g) Al 2p peaks of LS_$MFC_{0.25}$A at 25 and 800 °C.

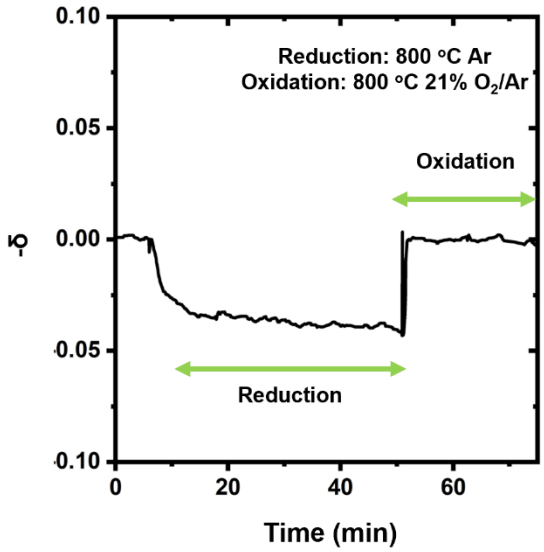

Figure 1. 8 Extent of reduction of LS_$MFC_{0.25}$A under an isothermal redox cycle at 800 °C.

Sr also exhibited a side peak evolution, which was assigned to slight Sr segregation that is widely found in solid oxide fuel cells.[62–64] For the B-site elements, Mn, Fe, and Co can be potentially redox active.

Al 2p showed negligible shift due to the stable Al^{3+} valence state. Co 2p showed an increased intensity and broadening of the side peak located at 787 eV, which is a Co^{2+} $2p_{3/2}$ satellite peak. This satellite peak evolution suggests that Co^{3+} is reduced to Co^{2+} during the in-situ heating process, in agreement with previous reports.[65–67] In contrast, Fe 2p and Mn 2p had negligible changes upon heating. Therefore, Co is likely the primary redox element, consistent with the correlation between Δδ and Co content in the TGA.

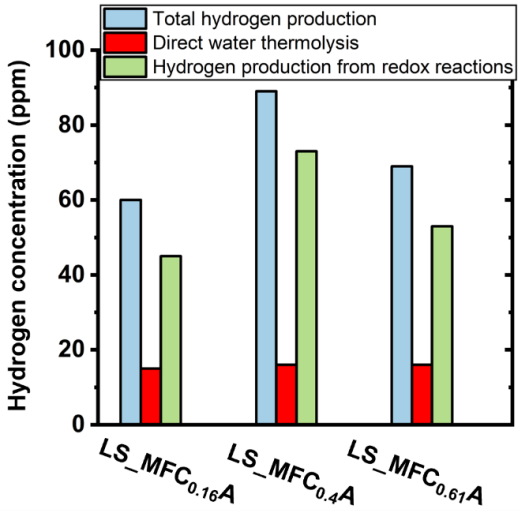

Figure 1. 9 Effect of direct catalytic water thermolysis in STCH reactions of LS_MFC$_x$A
The total hydrogen production was measured under T_{Re} 1350 °C for 45 min and T_{Ox} 1100 °C for 15 min. Water thermolysis was measured on oxidized samples (redox reaction was minimized) at 1100 °C with a same steam flow. All LS_MFC$_x$A compositions show very similar water thermolysis behavior. Then, the background H_2 production from catalytic water thermolysis was subtracted from the total H_2 yield and only the H_2 production from the redox reaction was illustrated.

It is worth noting that the water thermolysis catalyzed by the alumina tube and samples could take place at 1100 °C in 40 vol% steam flow producing a small quantity of H_2, which has been recently reported.[68–70] Thus, the H_2 production from direct catalytic water splitting was measured (Figure 1.9) and subtracted from the total H_2 production to extract the true H_2 production from the redox reaction. Figure 1.10a shows the molar H_2 production per mole of various LS_MFC$_x$A under the given conditions. The hydrogen production increased from LS_MFC$_{0.16}$A to LS_MFC$_{0.4}$A and then rapidly fell after x = 0.61. The relationship of H_2 production with the Co content has a volcano shape with the peak H_2 production achieved by LS_MFC$_{0.4}$A, similar to the observed trend in La(Ga$_{1-y}$Co$_y$)O$_3$.[32] Under this condition, LS_MFC$_{0.4}$A produced the highest H_2 production (49.88 mmol mol_{oxide}^{-1}) although it had a medium Δδ. In contrast, the simple perovskite LSC

showed the minimal H_2 production (4.48 mmol mol_{oxide}^{-1}) despite its largest Δδ. The molar ratio of H_2 to O_2 produced in the oxidation and reduction steps, respectively, is 2:1 (Figure 1.11), suggesting the water splitting is realized by the redox reaction.

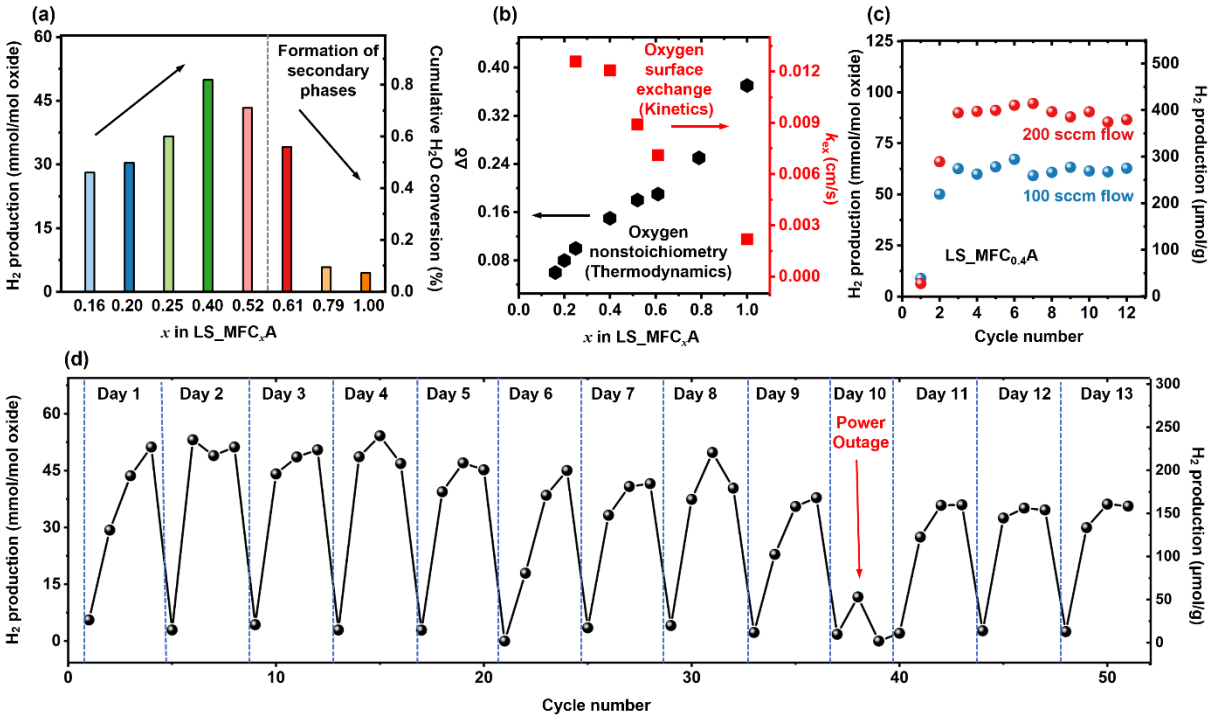

Figure 1. 10 Average hydrogen production and cumulative H_2O conversion extent measurements of LS_MFC$_x$A
(a) Average hydrogen production and cumulative H_2O conversion extent of two stabilized cycles for LS_MFC$_x$A. The reduction was conducted at 1350 °C (T_{Re}) in N_2 for 45 min and oxidation was performed at 1100 °C (T_{Ox}) in 40 vol% H_2O for 15 min with a gas flow rate of 100 sccm. H_2 production shows a volcano plot shape with respect to Co molar ratio in LS_MFC$_x$A. (b) The dependences of Δδ (measured by TGA) and oxygen surface exchange coefficient k_{ex} (measured by electrical conductivity relaxation) on the Co content in LS_MFC$_x$A. The thermodynamic (Δδ) and kinetic (k_{ex}) properties demonstrate opposite correlation with Co molar ratio in LS_MFC$_x$A. (c) H_2 production stability of LS_MFC$_{0.4}$A under different flow rate during the uninterrupted cycling (T_{Re} = 1350 °C for 30 min in N_2 and T_{Ox} = 1100 °C for 30 min in 40 vol% steam). (d) Long-term STCH cycling of LS_MFC$_{0.4}$A under harsh interrupted cycling conditions involving startup heating and shutdown cooling, at a STCH condition producing significant (but not maximized) H_2 production. Specifically, the sample was heated in the morning and cooled down to room temperature at night and four cycles were performed per day (using the STCH condition: T_{Re} = 1350 °C for 45 min in N_2 and T_{Ox} = 1100 °C for 15 min in 40 vol% steam with a gas flow rate of 100 sccm). This simulates the real day-night cycle conditions for STCH than uninterrupted cycling. Background H_2 production from catalytic water thermolysis was subtracted from the total H_2 production and only the H_2 production from the redox reaction was illustrated.

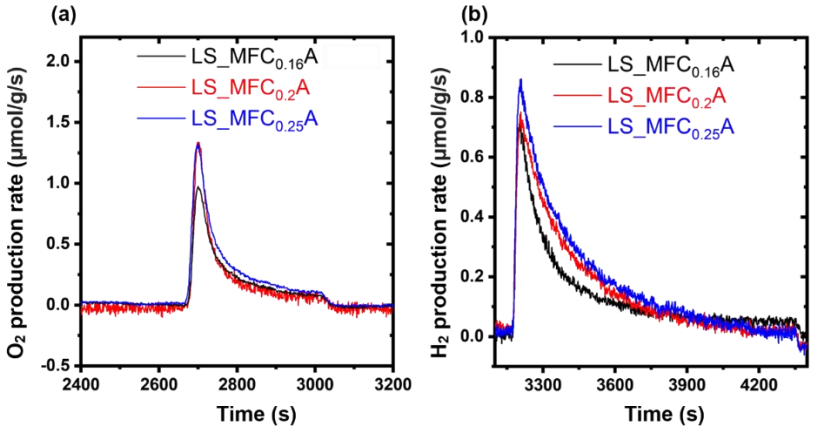

Figure 1. 11 STCH tests in a home-made reactor at the Sandia National Laboratory for LS_MFC$_x$A
The STCH tests were done at T_{Re} = 1350 °C for 330 s and T_{Ox} = 1100 °C with 40 vol% H_2O for 1200 s. The gas production rates of different samples as a function of time for (a) O_2 and (b) H_2. The H_2:O_2 molar ratio was close to 2:1 for all samples.

The volcano shaped plot of hydrogen production *vs.* Co molar ratio may relate to the trade-off between the thermodynamic and kinetic properties as shown in Figure 1.10b. The intrinsic kinetic properties of the LS_MFC$_x$A series were examined by using the electrical conductivity relaxation (ECR) technique, which can quantify the oxygen surface reaction coefficient k_{ex}, i.e. the proportionality between the rate of oxygen incorporation and deviation of surface oxygen concentration by monitoring the response of electrical conductivity to the change of P_{O_2}.[71,72] It is found that the thermodynamic and kinetic properties can be readily tailored by tuning the Co content in LS_MFC$_x$A. Figure 1.10b illustrates an opposite correlation of the thermodynamic ($\Delta\delta$) and kinetics (k_{ex}) properties with the Co content, where more Co decreases the kinetics but increases $\Delta\delta$. In this series, LS_MFC$_{0.4}$A likely achieved a balance between the thermodynamic and kinetic properties, delivering the highest H_2 production within the given duration. The oxygen uptake and release tests further confirm the superior oxygen incorporating kinetics of LS_MFC$_x$A with a lower Co content (Figure 1.12). Additionally, LS_MFC$_x$A with a high Co content (x > 0.52) showed inferior phase stability, where the formation of secondary RP phase (Figure 1.5c and d) is unfavorable for the H_2

production. Therefore, we focused on the optimal composition LS_MFC$_{0.4}$A to further investigate its STCH performance.

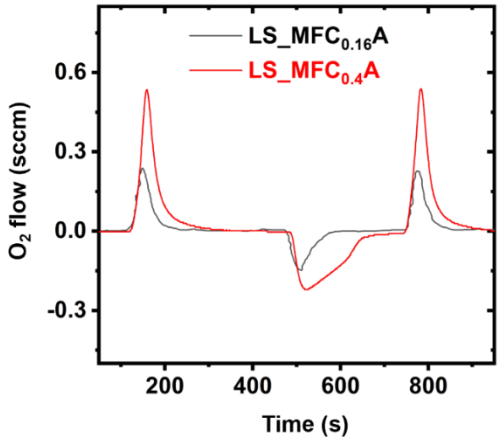

Figure 1. 12 Rate of O_2 released and absorbed by LS_MFC$_{0.16}$A and LS_MFC$_{0.4}$A at 0.2 mbar P_{O_2}
Samples heated at 20 ºC s^{-1} between 1000 and 1350 ºC and held isothermally at 1350 ºC for 300 s (O_2 release). The oxidation time was 250 s at 1000 ºC (O_2 uptake). The slope of LS_MFC$_{0.16}$A in the segment from peak O_2 release rate to the equilibrium is larger than that of LS_MFC$_{0.4}$A, indicating the superior oxygen incorporating kinetics in LS_MFC$_{0.16}$A.

Table 1. 3 Summary of STCH production results of LS_MFC$_{0.4}$A under different testing conditions.
The reduction was conducted at 1350 °C in N_2 and oxidation was performed in 40% steam with N_2 for all cases.
Cumulative H_2 production was reported in two units.

Condition #	Flow Rate (sccm)	T_{ox} (°C)	t_{Re} (min)	t_{Ox} (min)	Cumulative H_2 production (μmol g^{-1}) / (mmol mol^{-1})	H_2O conversion extent (%)
C1	100	800	45	15	49 / 11.16	0.18
C2	100	1000	45	15	194 / 44.19	0.72
C3	100	1100	45	15	219 / 49.88	0.82
C4	100	1100	30	30	270 / 61.50	0.50
C5	100	1100	30	60	351 / 79.95	0.33
C6	200	1100	30	30	395 / 89.97	0.74

The hydrogen production is influenced by the testing conditions, such as the gas flow rate, reaction temperature (T_{Re} and T_{Ox}) and reaction time (t_{Re} and t_{Ox}). Therefore, the effects of these factors on the H_2 production of LS_MFC$_{0.4}$A were systematically investigated. The reduction temperature was fixed at 1350

°C. Table 1.3 summarizes the cumulative H_2 production in the stabilized cycle under different conditions. A larger temperature swing by reducing the oxidation temperature (C1, C2 and C3) reduced the H_2 production in the 1-hour cycle, although the larger temperature swing is supposed to thermodynamically favor the H_2 production. The elevated oxidation temperature of (C3) rendered H_2 production four times higher than the lower oxidation temperature (C1) under the given reduction and oxidation durations and flow rate, as the former promoted the reaction kinetics. Therefore, the oxidative water splitting step ($ABO_{3-\delta} + \delta H_2O = ABO_3 + \delta H_2$) benefits from an increase in the oxidation temperature (C1 → C3), indicating that this H_2 production step is primarily limited by kinetics. A similar positive effect of elevated oxidation temperature on the H_2 production has been reported in $Sr(Ti_{0.5}Mn_{0.5})O_3$ and $Ca(Ti_{0.5}Mn_{0.5})O_3$.[30,48] Furthermore, when T_{Ox} was higher than 1200 °C, the alumina tube produced a substantial H_2 background level arising from its catalytic water thermolysis. Thus, we did not further investigate higher oxidation temperatures. The extended oxidation time enhanced the H_2 production, confirming the kinetically limited oxidative water splitting step. Increasing the flow rate of steam also boosted the H_2 production from 61.50 mmol mol_{oxide}^{-1} at 100 sccm to 89.97 mmol mol_{oxide}^{-1} at 200 sccm within 30-min oxidation time likely due to the improved mass transfer of steam and rapid removal of H_2 product. The oxidation reaction rate is limited by the supply of H_2O. The experimentally measured H_2 production (89.97 mmol mol_{oxide}^{-1}) is very close to the theoretically calculated thermodynamic limit value of 93.39 mmol mol_{oxide}^{-1} (see next discussion). The highest H_2 production of 89.97 mmol mol_{oxide}^{-1} in a short duration (30 min oxidation and 30 min reduction) for LS_$MFC_{0.4}$A is higher than those of reported STCH materials with longer oxidation and reduction durations (Table 1.4). For this fundamental research, we used an excess of steam feeding and a small quantity of perovskite oxide powder (~0.1 g) to ensure the sufficient steam/solid contact and mass transfer for measurement of the thermodynamic limit of H_2 production to analyze the correlation of H_2 production with material properties. Therefore, a large excess of steam feedstock makes the cumulative H_2O conversion extent less than 1% as shown in Figure 1.10a and Table 1.3. For future engineering design and evaluation of its viability for practical application, the steam reactant feeding should be limited, and a

large size of reticulated porous ceramic monolith should be used for improving the conversion extents to an industrially meaningful steam-to-H_2 conversion.[73]

Table 1. 4 Comparison of STCH performance of LS_$MFC_{0.4}$A with those of other reported materials

Material	Sample mass (g)	T_{TR} (°C)	t_{TR} (min)	T_{OX} (°C)	Oxidation gas pH_2O(atm)	t_{OX} (min)	Cumulative H_2 production (μmol g^{-1})/(mmol mol^{-1})	Cycle number	Reference
LS_$MFC_{0.4}$A	0.1	1350	30	1100	0.4	30	395/89.97[a]	12 (continuous)	This work
LS_$MFC_{0.4}$A	0.1	1350	45	1100	0.4	15	225/51.25 to 161/36.67[b]	51 (interrupted)	This work
$CaTi_{0.5}Mn_{0.5}O_3$	0.2559	1350	30	1150	0.4	60	441/61.51[a]	14 (continuous)	30
$SrTi_{0.5}Mn_{0.5}O_3$	0.2529	1350	30	1100	0.4	60	366/68.45[a]	8 (continuous)	48
$LaGa_{0.3}Co_{0.7}O_3$	0.5	1350	132.5	800	1.0	400	200/49.82[a]	1 (continuous)	32
$BaCe_{0.25}Mn_{0.75}O_3$	0.1	1350	5.5	1000	0.4	20	140/36.62[a]	50 (continuous)	35
$La_{0.6}Ca_{0.4}Mn_{0.6}Al_{0.4}O_3$	0.5	1400	140	1000	0.4	60	429/81.99 to 400/76.45[b]	5 (continuous)	33
$La_{0.6}Sr_{0.4}Mn_{0.6}Al_{0.4}O_3$	0.1	1350	30	1000	0.4	30	307/64.52[a]	1 (continuous)	31
$La_{0.6}Sr_{0.4}Mn_{0.6}Al_{0.4}O_3$	0.5	1350	80	800	1.0	230	254/53.38 to 179/37.62[b]	3 (continuous)	32
$La_{0.6}Sr_{0.4}MnO_3$	0.51	1400	70	800	0.2	60	392/86.76[a]	8 (continuous)	74
$YCr_{0.75}Zr_{0.25}O_3$ (75 wt.%) + CeO_2 (25 wt%)[c]	0.4	1400	40	1300	0.75	40	299.8/59.57 to 244.6/48.6[b]	11 (continuous)	75
$La_{0.6}Sr_{0.4}Co_{0.2}Cr_{0.8}O_3$	0.2	1200	60	800	0.025	60	50/10.99[a]	4 (continuous)	76

[a]STCH cycling was relatively stable in shown cycles and thus the stabilized H_2 production is given. [b]The highest and lowest H_2 production values are given to present the decay. [c]Only the molecular weight of $YCr_{0.75}Zr_{0.25}O_3$ is used to calculate the H_2 production per mole oxide.

We investigated the cyclability of LS_$MFC_{0.4}$A under both uninterrupted and harsher interrupted conditions. Figure 1.10c exhibits the uninterrupted cycling test results. After the initial two activation cycles, LS_$MFC_{0.4}$A maintained a stable H_2 production of 61.50 mmol mol^{-1} (270 ± 9 μmol g^{-1}) and 89.97 mmol mol^{-1} (395 ± 11 μmol g^{-1}) at a steam flow rate of 100 and 200 sccm for the following 10 consecutive cycles, respectively. The STCH cycling stability of LS_$MFC_{0.4}$A under the continuous testing conditions is comparable to that of reported STCH redox oxides, whereas the stable H_2 production of LS_$MFC_{0.4}$A is

higher (Table 1.4). The particle morphology and EDS mapping of pristine and cycled LS_$MFC_{0.4}$A are shown in Figure 1.13. The LS_$MFC_{0.4}$A after 12 cycles did not show significant element segregation despite apparent sintered particles. Note that the seemingly inhomogeneity in EDS maps of some elements such as Sr and Al compared to other elements is owing to the different element interaction volume rather than their inhomogeneous distribution. In general, the configurational entropy of a multi-component solid solution can be enhanced by mixing a large number of cations ideally in equiatomic proportions and a single solid-solution phase can be stabilized if the entropy contribution overcomes the enthalpy-driven phase separation.[1,77,78] Therefore, the phase stability of CCPO after redox cycling is possibly attributed to the entropy stabilization effect, stabilize a single solid-solution phase and inhibit precipitation during the thermal or electrochemical redox cycling.[79–83] For the practical STCH applications, the diurnal cycle of sunlight irradiation should be considered without the viable, efficient, large-scale, and stable thermal energy storage technology,[84–86] as the STCH materials may subject to drastic temperature swing between elevated temperatures under 8-hour strong sunlight irradiation (operation mode) in the day and low temperatures of long-time cooling stage (downtime mode) in the night. In stark contrast to the ideal uninterrupted cycling condition using a stable heat source, such interrupted cycling involving startup heating and shutdown cooling is a harsh condition to the STCH application, which can induce thermal fatigue, impair the structural integrity, and dramatically deteriorate the H_2 production cycle.[87,88] A similar challenge exists in other solar-driven hydrogen production technologies such as photovoltaic driven water electrolysis, where the startup and shutdown cycling due to the day-night cycle causes degradation of electrocatalysts.[89–92] Therefore, the interrupted cycling stability of LS_$MFC_{0.4}$A for thermochemical hydrogen production was evaluated under the daily startup and shutdown cycling for 13 days (51 cycles) to simulate the real diurnal cycle. Note that more cycles per day may be carried out in a real reactor with faster ramping rates, in comparison with our home-made testing reactor. Figure 1.10d demonstrates that LS_$MFC_{0.4}$A showed around 30% decay in H_2 production under this harsh condition after 13 days, indicating that its moderate cycling stability against thermal fatigue and redox degradation requires further improvement for practical application. To the best of our knowledge, few research on development of STCH materials has paid attention to the cyclability

under this harsh condition. However, the stability of Cu-ZnO-Al_2O_3 catalyst for simulated solar methanol production has been investigated under the daily startup-shutdown conditions, showing 27% activity degradation during 27 cycles (6.3-h operation and 17.7-h shutdown per cycle).[87] Future efforts are needed to enhance the cycling stability of thermochemical redox oxides under the interrupted conditions for real-world applications. The SEM images and EDS mapping (Figure 1.13c) of LS_$MFC_{0.4}$A after 51 cycles displayed sintered morphology but homogeneous elemental distribution.

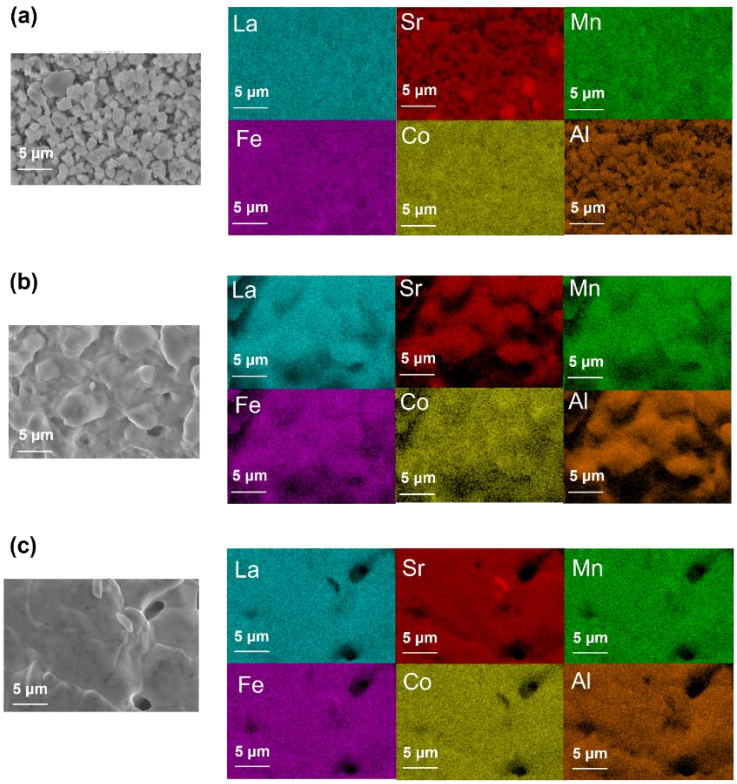

Figure 1. 13 SEM-EDS elemental mapping of LS_$MFC_{0.4}$A before and after STCH cycles.
(a) pristine specimen, (b) specimen after 12 continuous cycles of STCH test and (c) specimen after 51 interrupted cycles of STCH test.

In addition to the proven excellent thermal stability and intrinsic surface oxygen exchange kinetics, two thermodynamic properties, enthalpy and entropy of reduction, are important factors determining the performance of STCH materials.[51,93,94] Therefore, we carried out the measurements of the oxygen non-

stoichiometry over a range of temperatures and P_{O_2} values for LS_MFC$_{0.4}$A using a widely reported TGA protocol (Figure 1.14).[30,48,95–97]

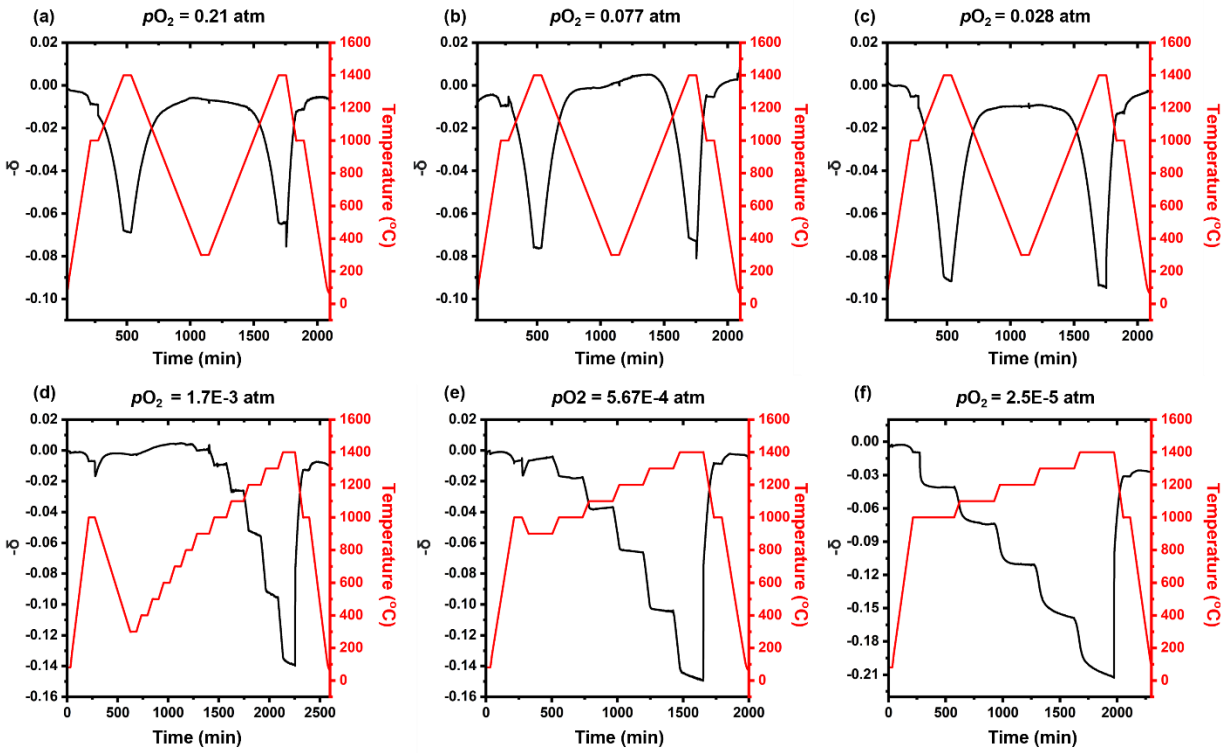

Figure 1. 14 Oxygen non-stoichiometry measured by the mass loss and temperature profiles under different P_{O_2}.

Figure 1.15a shows the oxygen non-stoichiometry of LS_MFC$_{0.4}$A as a function of temperature measured by continuous ($P_{O_2} \geq 0.028$ atm) and stepwise ($P_{O_2} \leq 1.7\times10^{-3}$ atm) heating under the given P_{O_2} values. Following the van't Hoff method,[30,98,99] the enthalpy and entropy of reduction can be correlated with temperature and P_{O_2} according to the following equation:

$$Rln(P_{O_2})^{\frac{1}{2}} = -\frac{\Delta_{red}H(\delta)}{T} + \Delta_{red}S(\delta) \qquad (1.6)$$

where R is the universal gas constant, and P_{O_2} is equal to the oxygen partial pressure referenced to the standard gas pressure (1 atm). T is the temperature in Kelvin. $\Delta_{red}H(\delta)$ and $\Delta_{red}S(\delta)$ are the standard

enthalpy and entropy of reduction, respectively, which are dependent on δ and defined on a per mole of oxygen basis but have negligible dependence on temperature.

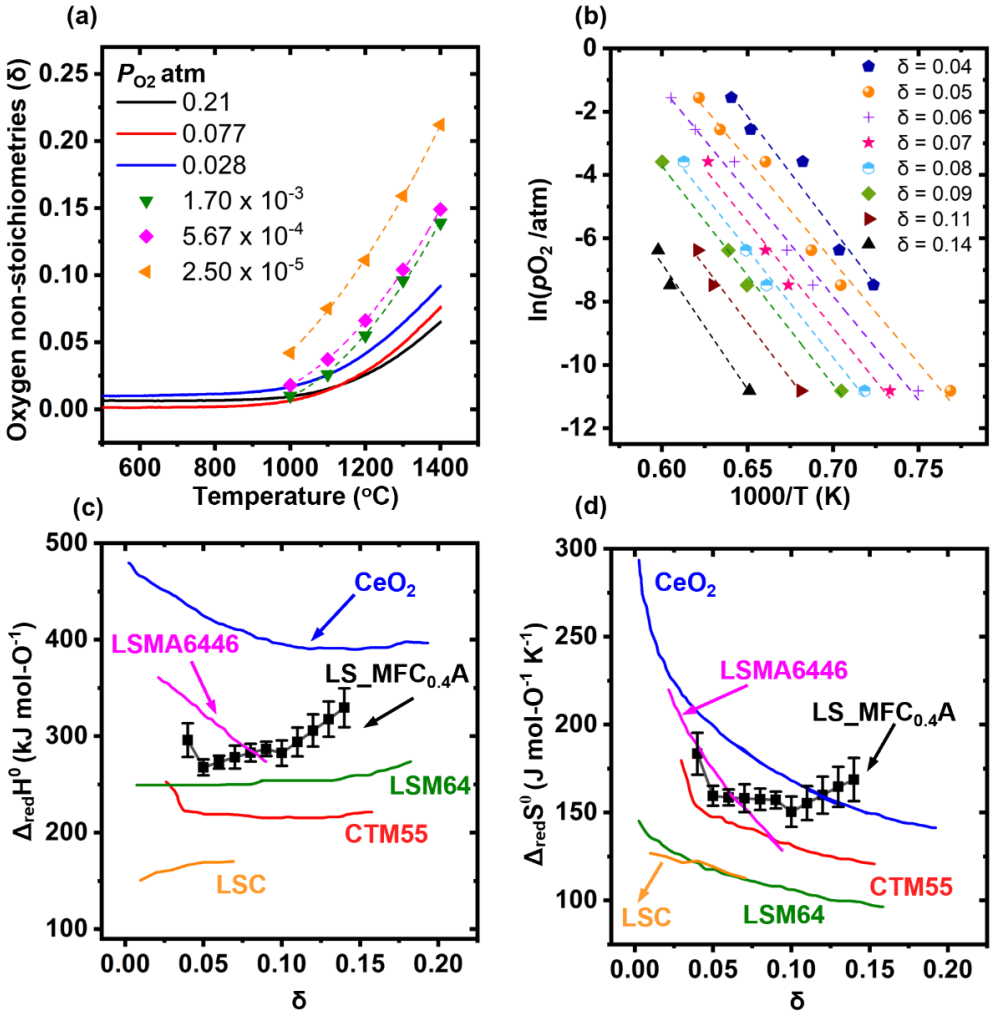

Figure 1. 15 Oxygen non-stoichiometry of LS_MFC$_{0.4}$A as a function of temperature and oxygen partial pressure. (a) Oxygen non-stoichiometry of LS_MFC$_{0.4}$A as a function of temperature as measured by continuous (solid lines) and stepwise (symbols) heating under the given P_{O_2} values. (b) Arrhenius representation of ln(P_{O_2}) *vs.* 1000/*T* for extraction of thermodynamic properties (e.g., enthalpy and entropy of reduction) by the van't Hoff method at typical fixed δ values as indicated. Symbols and dash lines in the profile represent the measured and linearly fitted results, respectively. (c) Standard enthalpy and (d) entropy of reduction calculated for LS_MFC$_{0.4}$A and comparison to those of some reported STCH and redox oxide materials. The error bars of LS_MFC$_{0.4}$A came from the error of its linear fitting. Data for CeO_2,[99] $La_{0.6}Sr_{0.4}Mn_{0.4}Al_{0.6}O_3$ (LSMA6446),[100] cubic $CaMn_{0.5}Ti_{0.5}O_3$ (CTM55),[30] $La_{0.6}Sr_{0.4}MnO_3$ (LSM64),[101] and $La_{0.8}Sr_{0.2}CoO_3$ (LSC)[96] are replotted from prior studies cited herein.

An Arrhenius plot of ln(P_{O_2}) *vs.* 1000/*T* at each specified δ value with linear fitting can be obtained (Figure 1.15b), from which $\Delta_{red}H(\delta)$ and $\Delta_{red}S(\delta)$ can be extracted from the slope and intercept,

respectively. In this way, the enthalpy and entropy of LS_MFC$_{0.4}$A as a function of δ are obtained (Figure 1.15c and d) and compared with those of some reported STCH and redox oxide materials such as CeO_2,[99] cubic $Ca(Mn_{0.5}Ti_{0.5})O_{3-\delta}$ (CTM55),[30] $La_{0.6}Sr_{0.4}MnO_{3-\delta}$ (LSM64),[101] $La_{0.6}Sr_{0.4}Mn_{0.4}Al_{0.6}O_{3-\delta}$ (LSMA6446),[100] and $La_{0.8}Sr_{0.2}CoO_3$ (LSC).[96]

Previous experimental and theoretical studies suggested that a combination of intermediate enthalpy and large entropy is favorable for STCH from water splitting.[30,97,100,102] For perovskite materials, the enthalpy of reduction can be tuned by the dopants,[103] and is desirably constrained to a certain moderate range (neither too high nor too low), which may follow a Sabatier principle. A low enthalpy of reduction usually accompanies a low entropy of reduction under the given conditions (temperature and P_{O_2}) for a variety of redox oxide materials, rendering favorable reduction reactions but not oxidative water splitting.[102,104] In contrast, a high enthalpy of reduction enables a high energy penalty for thermal reduction. LS_MFC$_{0.4}$A shows enthalpy and entropy values comparable to LSMA6446 and CTM55 which have been identified to have prominent hydrogen production with an appropriate combination of moderate enthalpy and relatively large entropy.[30,100] With the measured thermodynamic properties, the equilibrium H_2 production was calculated to be 93.39 mmol mol_{oxide}^{-1} under the condition C6 listed in Table 1.4. Compared with ceria, LS_MFC$_{0.4}$A possess a much lower enthalpy but similar entropy of reduction when Δδ is more than 0.1, suggesting its potential for high H_2 production under a lower reduction temperature. As shown in the TGA results (Figure 1.5), the Δδ value of LS_MFC$_x$A increases with *x*, possibly due to the decreased enthalpy of reduction upon the increasing content of Co. For example, LSC material shows a small enthalpy (< 200 kJ mol^{-1}) and entropy simultaneously, suggesting that it tends to have a large Δδ but poor oxidative water splitting capability. This is in good agreement with our TGA and STCH results for LSC. LS_MFC$_{0.4}$A displays the highest hydrogen production in this LS_MFC$_x$A series. This finding suggests that while maintaining a moderate enthalpy of reduction, multiple cations in LS_MFC$_x$A may introduce extra configurational entropy to fulfill the needs of oxygen vacancy formation and electronic and ionic configurational entropy change.[105,106]

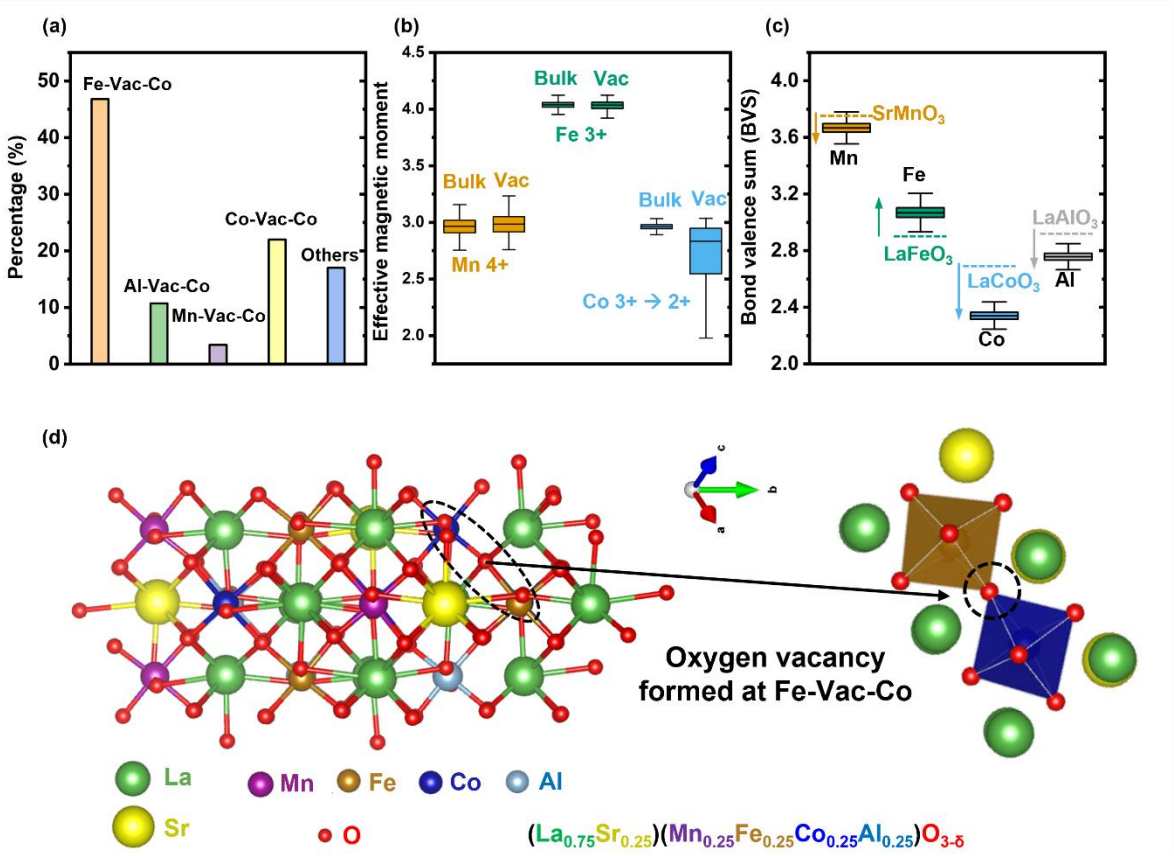

Figure 1. 16 Computational modeling of $(La_{0.75}Sr_{0.25})(Mn_{0.25}Fe_{0.25}Co_{0.25}Al_{0.25})O_3$ by MC/DFT
(a) Vacancy (Vac) B-site first nearest neighbors (FNN) distributions show dominant Co preference over other B-site elements. (b) Local magnetic moment evolution between bulk and vacancy configurations for 3d orbitals of Mn, Fe and Co from saved bulk structures (~2600 configurations) and vacancy structures (~3000 configurations) shows that Co goes through the largest magnitude change when a single neutral oxygen vacancy is formed. The bulk structure represents the supercell structure before introducing an oxygen vacancy. (c) Calculated bond valence sum (BVS) for Mn, Fe, Co, and Al octahedra in $(La_{0.75}Sr_{0.25})(Mn_{0.25}Fe_{0.25}Co_{0.25}Al_{0.25})O_3$ structure (solid lines for median BVS values and box plots). The dash lines present the BVS values of $SrMnO_3$, $LaFeO_3$, $LaCoO_3$, and $LaAlO_3$ simple perovskite references based on our DFT calculations. (d) Representative of the simulation cell containing oxygen vacancy with Fe and Co as FNN of the position with the largest percentage where an oxygen vacancy is formed.

To elucidate why Co is the most redox active in LS_MFC$_x$A and shed light on the factors governing the priority of redox behavior, we employed MC sampling based on DFT. It was found that *Pnma*, $R\bar{3}c$, and $Pm\bar{3}m$ structures have similar energies and configurations. Thus, only $R\bar{3}c$ results were reported here, consistent with the XRD patterns of LS_MFC$_x$A. For bulk structures without oxygen vacancies, the nearest neighbor check was adopted to confirm if there are any B-cations' configurational preferences. The oxygen atom is surrounded by four first nearest neighbor (FNN) with two A-site atoms and two B-site atoms in the

$R\bar{3}c$ structure. In the accepted low energy $(La_{0.75}Sr_{0.25})(Mn_{0.25}Fe_{0.25}Co_{0.25}Al_{0.25})O_3$ 80-atom supercell, the probability of finding oxygen FNN B-site elements to be the same type of B_1 element is $P(B_1 - O - B_1) = \frac{4}{16} \times \frac{3}{15} = 0.05$. The probability to find two atoms of different elements $B_1 - B_2$ is $P(B_1 - O - B_2) = 2 \times \frac{4}{16} \times \frac{4}{15} = \frac{2}{15} \approx 0.133$, suggesting no configurational preference for B-site cation combinations. Therefore, the cation configuration of the fully oxidized bulk structure is similar to a random distribution without signatures of B-site short-range ordering consistent with the defined CCPO structure. By introducing a single neutral oxygen vacancy, the configurational preference is changed. For the accepted vacancy containing configurations, the B-site distribution in Figure 1.16a shows that 83% of the combinations (incl. Fe-Vac-Co (46.8%), Al-Vac-Co (10.7%), Mn-Vac-Co (3.4%), and Co-Vac-Co (22.1%)) prefer to have at least one Co at its FNN position in $R\bar{3}c$ structure, strongly deviating from the probability in a random distribution (0.05+0.133×3=44.9%). One of the possible positions of formed oxygen vacancy is illustrated in Figure 1.16d (Fe-Vac-Co). Therefore, the computed probability of oxygen FNN {B} site strongly deviates from the probability in a random oxygen FNN {B} site distribution (83% versus 44.9%) for at least one Co in the B site, suggesting the Co preference in vacancy configurations owing to the parallel evolution setting in DFT-MC for bulk and vacancy configurations. A further analysis of the magnetic moments of the B-site transition metal elements excluding the non-magnetic Al in the accepted low energy bulk and vacancy systems was conducted to reveal how the oxygen vacancy changes the cation valence states. The magnetic moment magnitude is directly correlated with the oxidation state of the magnetic transition metal. The statistical distribution plotted in Figure 1.16b shows the respective magnetic moment magnitude changes of Mn, Fe, and Co in bulk and vacancy configurations. Before the vacancy is formed (i.e., bulk), the median magnetic moment magnitudes for Mn, Fe, and Co are 3.0, 4.0, and 2.9, corresponding to oxidation states of Mn^{4+}, Fe^{3+}, and Co^{3+}, respectively. After introducing a single oxygen vacancy, Co is the element that has the greatest magnetic moment magnitude change ($Co^{3+} \rightarrow Co^{2+}$) and broadest distribution. The magnetic moment distribution of Mn is slightly broadened. The magnetic

moment distribution of Fe is almost unchanged. Therefore, the Co^{3+}/Co^{2+} redox pair is the most active in response to the formation of oxygen vacancies in the LS_MFC$_x$A systems, possibly followed by Mn^{4+}/Mn^{3+}.

A possible reason for the Co preference in vacancy configurations is the Co-O bond stretching effect. Since neutral vacancy formation causes volume expansion in many oxides, and a tensile stress (bond stretching) in the bulk will lower the vacancy formation energy.[107–109] In the CCPOs, local bond stretching may create more space to favor oxygen vacancy formation. To capture the local bond strength, the bond valence sum (BVS) descriptor was analyzed.[55] The BVS for each B-site cation in a perfect structure is close to its oxidation number. A lower (higher) value is considered as an elongated (compressed) bond with weaker (stronger) bond strength. For example, using the tabulated parameters (Table 1.2) developed by fitting experiments,[110] the BVS for Mn^{4+} in $SrMnO_3$, Fe^{3+} in $LaFeO_3$, and Co^{3+} in $LaCoO_3$, and Al^{3+} in $LaAlO_3$ are very close to 4.0, 3.0, 2.9, and 3.0 for their experimentally reported structures, respectively. The DFT calculated BVS of ternary perovskites (e.g., $SrMnO_3$, $LaFeO_3$, $LaCoO_3$, and $LaAlO_3$) serves as the references to compare with that of the bulk $(La_{0.75}Sr_{0.25})(Mn_{0.25}Fe_{0.25}Co_{0.25}Al_{0.25})O_3$ (solid lines and box plots in Figure 1.16c). The distribution of BVS for Co in $(La_{0.75}Sr_{0.25})(Mn_{0.25}Fe_{0.25}Co_{0.25}Al_{0.25})O_3$ is greatly lowered compared to that in the DFT reference structure ($LaCoO_3$), indicating a distortion induced bond elongation and weakening effect. The distributions of BVS for Mn and Al in $(La_{0.75}Sr_{0.25})(Mn_{0.25}Fe_{0.25}Co_{0.25}Al_{0.25})O_3$ are slightly lower than those in their DFT-relaxed ternary perovskite references, while the BVS for Fe in $(La_{0.75}Sr_{0.25})(Mn_{0.25}Fe_{0.25}Co_{0.25}Al_{0.25})O_3$ is increased compared to that in $LaFeO_3$ reference. These results demonstrate greatly weakened Co-O bond, slightly weakened Mn-O and Al-O bonds and strengthened Fe-O bonds in CCPO.

We further evaluated the deviation of BVS on each cation in $(La_{0.75}Sr_{0.25})(Mn_{0.25}Fe_{0.25}Co_{0.25}Al_{0.25})O_3$ from its oxidation number, and the root-mean-square value of this deviation for all the cations i.e., the global stability index *G*. All Sr and Fe ions are under compression and all La, Mn, Co, Al are under tension, while Co shows the largest negative deviation from its perfect BVS. The calculated global instability index *G* for saved bulk structures ranges from 0.217 to 0.233 vu, indicating strongly strained structures. According

to the BVS theory, structures with $G > 0.2$ are rare.[56] Hence, we propose that the Co preference in vacancy configurations is due to Co-O bond stretching effect. Although Mn^{4+} may be more reducible than Co^{3+} based on the classical charges, the Co-O bond stretching outweighs the tendency to generate vacancies near Mn^{4+}, resulting in the tendency to form oxygen vacancies adjacent to Co at its FNN position.

1.4 Conclusion

In this study, we demonstrated a new class of medium- to high-entropy CCPOs, LS_MFC$_x$A with tunable thermodynamic and kinetics properties for two-step thermochemical water splitting. The reversible extent of reduction ($\Delta\delta$) increases with the rising Co content (x), whereas the intrinsic kinetics (oxygen surface exchange coefficient) shows a decreased trend with the increasing x. LS_MFC$_{0.4}$A ($(La_{0.8}Sr_{0.2})(Mn_{0.2}Fe_{0.2}Co_{0.4}Al_{0.2})O_3$) exhibits an optimal balance between intrinsic thermodynamics and kinetics, as well as exceptional phase stability during the redox cycling and a favorable combination of moderate reduction enthalpy (268–329 kJ (mol-O)$^{-1}$) and high entropy (150–180 J (mol-O)$^{-1}$ K^{-1}). These merits of LS_MFC$_{0.4}$A enable a maximum hydrogen production of 89.97 mmol mol$_{oxide}^{-1}$ within a short 1-hour duration (30 min reduction and 30 min oxidation) under optimized STCH conditions as well as fair STCH cycling durability. The preferred redox of Co over other B-site metals is revealed by the TGA and in-situ XPS. A combined MC/DFT computation demonstrates that an oxygen vacancy prefers to form in the vicinity of the position with at least one Co at its first nearest neighbor. An analysis of the magnetic moments of the B-site metals confirms that the Co redox valence change is the most active in response to the formation of oxygen vacancies. The bond valence sum results demonstrate greatly weakened Co-O bond, slightly weakened Mn-O and Al-O bonds, and strengthened Fe-O bonds. The Co-O bond stretching effect rationalizes the dependence of $\Delta\delta$ on Co content and its dominance in the redox behavior of LS_MFC$_x$A.

In general, we showed the importance of achieving a trade-off of thermodynamic and kinetic properties for optimized STCH performance. This study further exemplifies that non-equimolar compositions outperform their higher-entropy equimolar counterparts in this two-step STCH application. While an

entropy effect may stabilize the phase, maximizing configurational entropy is not always needed ($S_{configuration}$ = 0.943k_B per B-site cation in equimolar LS_$MFC_{0.25}$A versus $S_{configuration}$ = 0.916 k_B per B-site cation in non-equimolar LS_$MFC_{0.4}$A, where is the Boltzmann constant). The non-equimolar compositional design of CCPOs provide a way to balance the thermodynamic and kinetic properties to achieve better STCH performance.

This work explores CCPOs with tunable redox, thermodynamic, and kinetic properties for STCH and thermochemical looping and a new computation paradigm to predict the redox behavior. Future efforts will be focused on investigating the mechanical strength and thermodynamic stability of porous ceramic monoliths during the thermochemical redox cycling process. Although kilowatt-level reactors for thermochemical production of solar fuels have recently been demonstrated,[18,111] various technical challenges still exist towards realization of the industrial STCH deployment in terms of the material and system scaling-up, reactant conversion extent, reaction selectivity, product purity, energy and power densities, energy efficiency, cycling stability under interrupted conditions, heat management, thermal energy storage, system complexity, and rigorous technoeconomic analysis, requiring continuous efforts of scientific and engineering communities. We believe that the emergent compositionally complex ceramics (CCCs),[10,11] including (but are not limited to) high-entropy ceramics (HECs) as a subset, with tunable redox capability, thermodynamic, and kinetic properties and improved phase stability will be of broad interest to diverse applications such as thermochemical looping, heterogeneous catalysis, and electrochemical energy conversion and storage.

Acknowledgements

Chapter 1, in full, is a reprint of the materials as it appears in Chemistry of Materials 2023. D. Zhang, H. A. De Santiago, B. Xu, C. Liu, J. Trindell, W. Li, J. Park, M. A. Rodriguez, E. N. Coker, J. Sugar, A. McDaniel, S. Lany, L. Ma, Y. Wang, G. Collins, H. Tian, W. Li, Y. Qi, X. Liu and J. Luo. The dissertation author was the primary investigator and author of this paper.

CHAPTER 2. Unusual aliovalent doping effects on oxygen non-stoichiometry in medium-entropy compositionally complex perovskite oxides

2.1 Introduction

Non-stoichiometric $ABO_{3-\delta}$ perovskite oxides have been proposed and explored as competitive candidates for several energy related applications, including solar thermochemical renewable fuel production,[30,31,35,46] ferroelectric materials,[112–114] and energy conversion devices.[115–117] The oxygen vacancies in $ABO_{3-\delta}$ facilitates oxygen reduction reactions.[118–120] Tailoring the oxygen non-stoichiometry by aliovalent doping has been proven to be an effective way to tailor the properties of perovskite oxides. For instance, doping $LaMnO_3$ and $LaFeO_3$ with 2+ alkaline earth elements like Sr and Ba can reduce the enthalpies of oxygen vacancy formation.[51,101] The substitution of La^{3+} with 2+ cations can introduce extra holes to the perovskite oxides, which increase the B-site metal cation oxidation states.[121,122] Similarly, B-site doping can create mixed valence states and tune the thermodynamic properties of perovskite oxides. Qian *et al*.[30] reported that Ti substitution of Mn in $Ca(Mn_{0.5}Ti_{0.5})O_3$ resulted in a significant improvement of H_2 generation in thermochemical cycling. In addition, simultaneous doping both A- and B-sites can further tune the properties of perovskite oxides.[32,123] A recent high-throughput study of the oxygen chemical potential engineering of perovskite oxides via machine learning also suggested improved redox properties of perovskite with multiple cations on both A- and B-sites.[124]

The emergent high-entropy ceramics (HECs),[3,125–127] as well as a broader class of compositionally complex ceramics (CCCs),[11,46] with multiple primary elements on A- and/or B-site cation sublattices offer a new opportunity to search for redox materials with a vast and tunable compositional space. With the increasing number of primary elements on the cation sublattices, the aliovalent doping effects can become complicated, producing new phenomena of potential scientific and technological interests. To date, the redox mechanisms in perovskite oxides with multiple redox active elements on the B site, as well as how they may interact with A-site doping, remain elusive, which motivated this study.

In this study, we synthesized two series of medium-entropy compositionally complex perovskite oxides (CCPOs) $(La_{1-x}Sr_x)(Mn_{1/3}Fe_{1/3}Cr_{1/3})O_3$ (denoted as "LS_MFC") and $(La_{1-x}Sr_x)(Mn_{1/3}Fe_{1/3}Ti_{1/3})O_3$

(denoted as "LS_MFT"), where we changed Sr molar ratio (x) on the A site and investigated the oxygen non-stoichiometry under thermochemical cycles. We discovered normal vs. abnormal behaviors in the reversible extent of reduction ($\Delta\delta$) *vs.* Sr molar ratio relations in LS_MFC (linear) and LS_MFT (V-shape). Combining the analysis of energy loss near edge structure (ELNES) in the electron energy loss spectra (EELS) in scanning transmission electron microscopy (STEM) with density functional theory (DFT) calculations, we showed that the replacement of Ti with Cr alters the effect of Sr dopant due to the stable Ti^{4+} state. This new finding suggests that the simultaneous doping on A and B sites can have coupling effects, which can lead to both complexity and opportunities to tailor compositionally complex oxides with three or more primary redox active cations on one sublattice.

2.2 Experimental Section

2.2.1 Material Synthesis and phase characterization

$(La_{1-x}Sr_x)(Mn_{1/3}Fe_{1/3}Ti_{1/3})O_3$ (LS_MFT) and $(La_{1-x}Sr_x)(Mn_{1/3}Fe_{1/3}Cr_{1/3})O_3$ (LS_MFC) were synthesized by conventional solid-state reaction methods. Oxide precursors with specific stoichiometric amount of La_2O_3 (99.99%), $SrCO_3$ (99.9%), MnO_2 (99.5%), Fe_2O_3 (99.99%), TiO_2 (99.99%) and Cr_2O_3 (99.7%), purchased from Alfa Aesar, were weighted, and put into a high energy ball milling (HEBM) jar with 2 wt.% steric acid. The starting powder was ball milled for 100 min and then pressed into pellets with hydraulic press. The green body pellets were annealed under 1450 °C for 12 hours under air. After sintering, the pellets were crushed and grounded into powders, and subsequently re-pressed into new pellets for another 12 hours annealing process to improve the phase purity. Finally, the pellets (that formed pure phases) were crushed again into powder for further characterization.

The crystal structures of synthesized materials were checked by X-ray diffraction (XRD, Miniflex Rigaku, Japan) with Cu Kα radiation. The XRD operating at 30 kV and 15 mA with scan speed 2°/min and step size 0.02°. The microstructure and elemental homogeneity were examined by scanning electron

microscope (SEM, FEI Apero, OR, USA) with energy dispersive X-ray spectroscopy (EDS, Oxford N-Max^N) operating at 20 kV and 3.2 nA.

2.2.2 Temperature programmed reduction

Temperature-programmed-reduction (TPR) experiments were conducted using a thermal gravimetric analyzer (TGA, Netzsch STA 449 F3 Jupiter). The mass of the samples used in these experiments was kept at around 30 mg. The temperature ramping profile was set to the following steps: (1) heating up at 25 °C/min to 1350 °C in UHP Ar and hold isothermally for 45 min; (2) cooling down to 900 °C while introducing 21% O_2 balanced with Ar for 25 min reoxidation; and (3) repeating Steps (1) and (2) for another cycle. The mass loss during the cycling was measured and the extent of reduction was calculated based on the following equation:

$$\delta = \frac{\Delta m * M_s}{m_s * M_o} \quad 2.1$$

where δ is the extent of reduction, Δm stands for the mass loss measured by the TGA, M_s and M_O represent the molar mass of specimen and oxygen, respectively.

2.2.3 Electron energy loss spectroscopy (EELS)

EELS experiments were conducted using a ThermoFisher Talos 200X operating at 200 kV with EELS spectrometer (Continuum ER1065, Gatan). The EELS spectra were taken under the scanning transmission electron microscopy mode (STEM) with high-angle annular dark field (HAADF) detector. The imaging was performed with a 70 mrad collection angle. A dispersion of 0.2 eV per channel was used to collect all the energy edges including Ti-$L_{2,3}$, Cr-$L_{2,3}$, Mn-$L_{2,3}$, Fe-$L_{2,3}$, and O K edge. The background of core-loss EELS spectra (Mn, Fe, Ti, La and O) was fitted by power law in Gatan DigitalMicrograph 3 (GMS 3).

2.2.4 Density functional theory (DFT)

Density functional theory (DFT) calculations were performed to calculate the formation energy of a neutral oxygen vacancy. In order to avoid the interaction between oxygen vacancies, a 160-atom $2\sqrt{2} \times 2\sqrt{2} \times 2$ supercell of the orthorhombic $LaBO_3$ (B = Fe, Mn, Cr, and Ti) and $SrCrO_3$, and cubic

$SrBO_3$ (B = Fe, Mn, and Ti) structures were used. All DFT calculations were performed using the Vienna Ab initio Simulation Package[128] with the generalized gradient approximation along with Perdew, Burke, and Ernzerhof (GGA-PBE)[54] and Hubbard U correction (U_{eff} = 3, 3, and 3.5 eV for Fe, Mn, and Cr, respectively).[28,107] The convergence criteria were 10^{-5} eV for the energy and 0.02 eV/Å for the atomic forces, and the planewave cutoff was set to 380 eV. The initial magnetic ordering was randomly half up and half down for the B-site cations, thus the total magnetic moment was set to zero. Since magnetic ordering of perovskites depends on temperature and pressure and the error associated with different magnetic configurations is the order of 0.01-0.02 eV/atom,[129] only total magnetic moment was used as a constraint.[130,131] The formation energy of a neutral oxygen vacancy was calculated as $E_V^f = E_{defective} - E_{bulk} + \mu_O^{FERE}$ where $E_{defective}$ and E_{bulk} indicate the DFT-calculated energy of a 160-atom supercell with and without a vacancy, respectively, and μ_O^{FERE} is the fitted elemental-phase reference energy (FERE) of oxygen (-4.76 eV for an oxygen atom).[129] For orthorhombic structures, the smaller E_V^f between two different Wykoff oxygen positions was chosen for the analysis.

2.3 Results and Discussion

All CCPO specimens were synthesized by a conventional solid-state method listed in Table 2.1

Table 2. 1 A list of 10 compositions of the samples investigated and their abbreviations.

Sample Abbreviation	Sample Composition
L_MFT	$La(Mn_{1/3}Fe_{1/3}Ti_{1/3})O_3$
LS82_MFT	$(La_{0.8}Sr_{0.2})(Mn_{1/3}Fe_{1/3}Ti_{1/3})O_3$
LS55_MFT	$(La_{0.5}Sr_{0.5})(Mn_{1/3}Fe_{1/3}Ti_{1/3})O_3$
LS46_MFT	$(La_{0.4}Sr_{0.6})(Mn_{1/3}Fe_{1/3}Ti_{1/3})O_3$
LS28_MFT	$(La_{0.2}Sr_{0.8})(Mn_{1/3}Fe_{1/3}Ti_{1/3})O_3$
S_MFT	$Sr(Mn_{1/3}Fe_{1/3}Ti_{1/3})O_3$
L_MFC	$La(Mn_{1/3}Fe_{1/3}Cr_{1/3})O_3$
LS55_MFC	$(La_{0.5}Sr_{0.5})(Mn_{1/3}Fe_{1/3}Cr_{1/3})O_3$
LS37_MFC	$(La_{0.3}Sr_{0.7})(Mn_{1/3}Fe_{1/3}Cr_{1/3})O_3$
S_MFC	$Sr(Mn_{1/3}Fe_{1/3}Cr_{1/3})O_3$

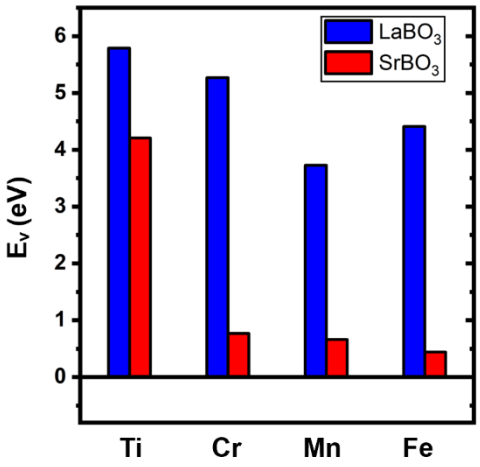

Figure 2. 1 DFT-calculated oxygen vacancy formation energies of all possible element combinations of ternary perovskite oxides $LaBO_3$ and $SrBO_3$ (B = Ti, Cr, Mn, or Fe).

Figure 2.1 displays the oxygen vacancy formation energy (E_v^f) of eight ternary perovskites with random combinations of elements in LS_MFT and LS_MFC calculated by density functional theory (DFT). The details of the calculations can be found in the ESI†. The blue and red bars represent DFT-calculated results for the $LaBO_3$ and $SrBO_3$ structures, respectively. In general, for a specific B-site element, $SrBO_3$ exhibits a lower oxygen vacancy formation energy than $LaBO_3$. Ternary perovskites with Ti on the B site maintain a higher oxygen vacancy formation energy ($LaTiO_3$ 5.79 eV, $SrTiO_3$ 4.21 eV) compared to other ternary perovskites. In addition, we notice that $LaTiO_3$ and $SrTiO_3$ have smaller differences on oxygen vacancy formation energies in contrast to the much larger differences present in Cr, Mn and Fe contained ternary perovskites. One reason for this phenomenon is due to the empty *d* orbital structure ($3d^0$) of Ti^{4+}. Even though the Sr substitution increases the oxidation state of Ti, the stable $3d^0$ valence structure also effectively prevents the Ti reduction and oxygen vacancy formation in $SrTiO_3$. Similarly, $LaFeO_3$ (4.41 eV) and $SrFeO_3$ (0.44 eV) have a large difference in oxygen vacancy formation energy because the half-filled $3d^5$ structure in Fe^{3+} allows much lower energy barriers of the Fe^{4+} to Fe^{3+} reduction, in comparison with that of Fe^{3+} to Fe^{2+}.

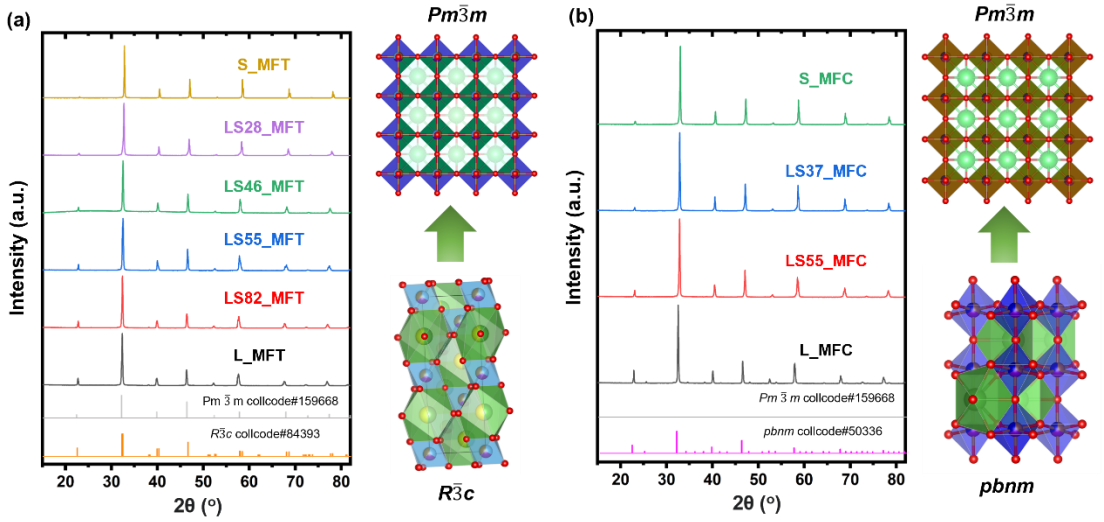

Figure 2. 2 XRD patterns of LS_MFC and LS_MFT series.
(a) synthesized LS_MFT series with a gradual transition from the rhombohedral R$\bar{3}$c (L_MFT) to cubic Pm$\bar{3}$m (S_MFT) structure and (b) synthesized LS_MFC series with a gradual transition from orthorhombic pbnm (L_MFC) to cubic Pm$\bar{3}$m (S_MFC) structure.

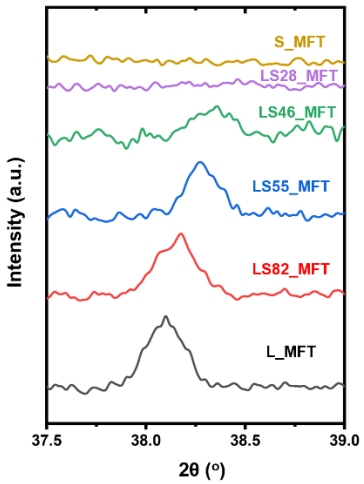

Figure 2. 3 Enlarged views of the XRD patterns of the (113) peak area

Figure 2.2a and b display the XRD patterns of the LS_MFT and LS_MFC series, respectively. From L_MFT to LS46_MFT, the XRD patterns can be indexed with a rhombohedral *R*$\bar{3}$*c* structure (ICSD collcode #84393). Higher Sr doping on the A site (with a larger A site ionic radius) leads to a structural transition to a cubic *Pm*$\bar{3}$*m* structure (ICSD collcode #159668) in LS28_MFT and S_MFT. The phase transition from rhombohedral to cubic structure was clearly evident by the evolution of peak (113) at around 38° shown in Figure 2.3. In the LS_MFT series, the rhombohedral (R$\bar{3}$c) to cubic (Pm$\bar{3}$m) phase transition

from is mainly controlled by the Goldschmidt tolerance factor, $t = (r_A + r_O)/[\sqrt{2}(r_B + r_O)]$, where r_A, r_B and r_O, respectively, are the ionic radiii of A- and B-site cations and O anions, respectively. The rhombohedral-to-cubic phase transformation takes place at around t = 1, as shown in the new Figure 2.4. In the LS_MFC series, L_MFC exhibited an orthorhombic *pbnm* structure (ICSD collcode #50336). The other three compositions showed the cubic $Pm\bar{3}m$ structure. To further examine the elemental homogeneity of these samples, we conducted high-resolution scanning electron microscopy SEM) energy dispersive X-ray spectroscopy (EDS) mapping. The SEM images and EDS elemental maps were shown in Figure 2.5 (LS_MFT) and 2.6 (LS_MFC). Most LS_MFT specimens maintain homogenous elemental distributions (except that LS82_MFT shows some minor La inhomogeneity). LS_MFC specimens show mostly uniform distribution albeit minor Cr enriched areas.

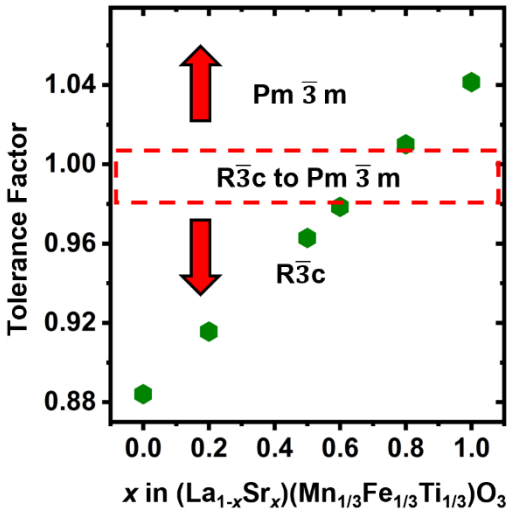

Figure 2. 4 The tolerance factor vs. *x* in $(La_{1-x}Sr_x)(Mn_{1/3}Fe_{1/3}Ti_{1/3})O_3$.

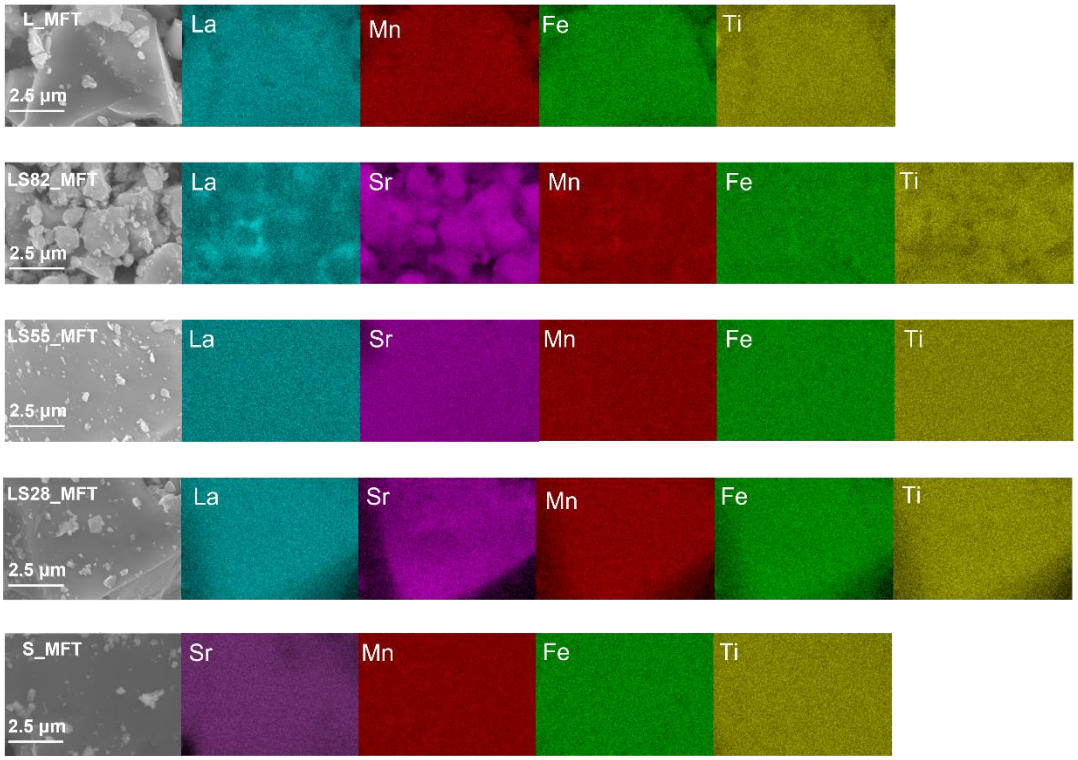

Figure 2. 5 High-resolution SEM images and EDS elemental maps of five LS_MFT compositions.

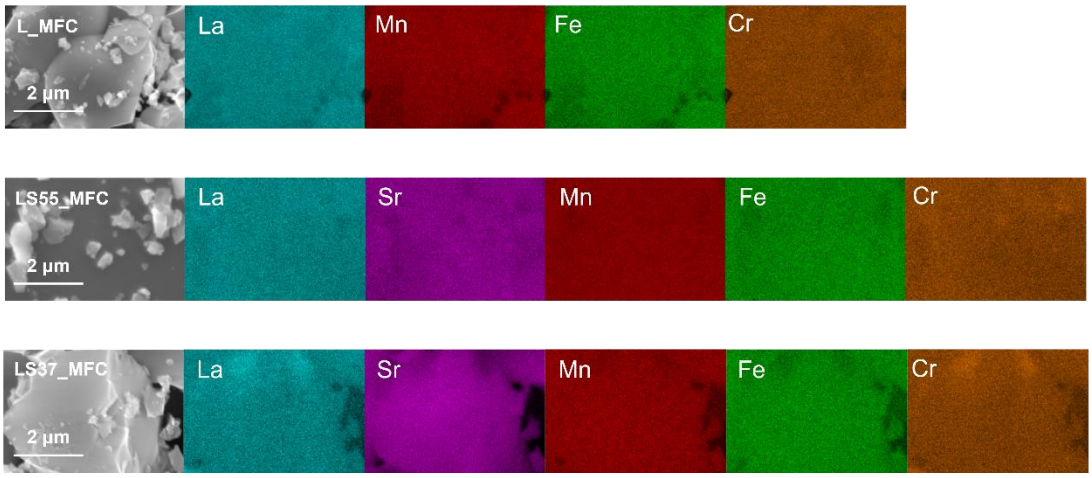

Figure 2. 6 High-resolution SEM images and EDS element maps of three LS_MFC compositions.

The redox capabilities were quantified by temperature programmed reduction (TPR) in thermogravimetric analysis (TGA) for all LS_MFT (for six different compositions) and LS_MFC (for four different compositions) by measuring Δδ, as shown in Figure 2.7a (LS_MFC) and b (LS_MFT). In thermochemical reactions (*e.g.*, solar thermochemical hydrogen production), perovskite oxides undergo the cycling between reduced ($ABO_{3-\delta red}$) and oxidized ($ABO_{3-\delta ox}$) states and $\Delta\delta$ ($= \delta_{red} - \delta_{ox}$) measures the

intrinsic amount of oxygen non-stoichiometry can be applied to generate renewable fuels such as H_2 (albeit at different specific P_{O2} conditions). For all TPR measurements, two consecutive redox cycles were performed with 45 min reduction at 1350 ºC under Ar and 25 min oxidation at 900 ºC under 21% O_2 balanced with Ar. The mass loss of the first cycle usually contains volatilization of surface absorbates like H_2O and amorphous carbon. Hence, the second cycles were reported here. The plateau of the oxidation step (21% O_2) of the first cycle was set as the zero reference to compare the oxygen non-stoichiometry ($\Delta\delta$) of different compositions. The temperature profile is presented as the dash line in the same figure.

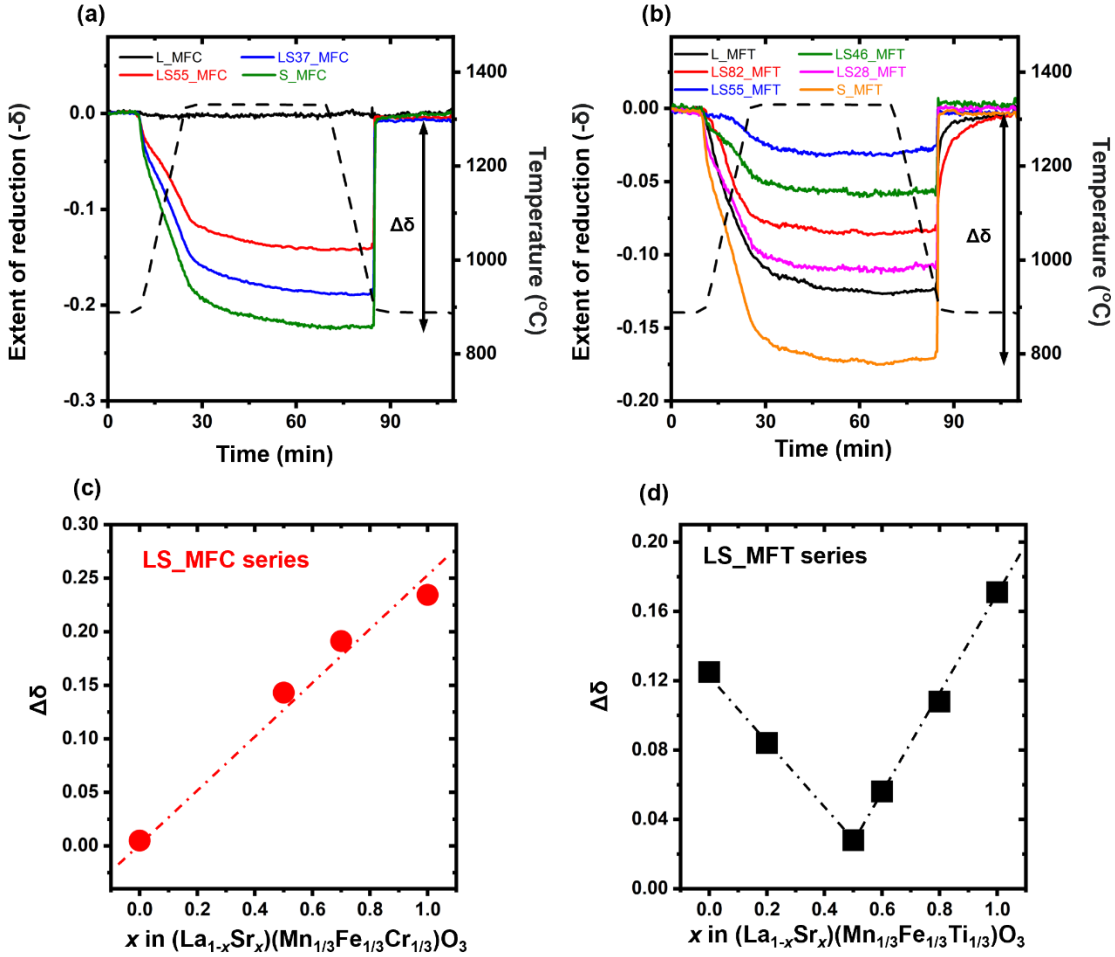

Figure 2. 7 Temperature programed reduction measurements of LS_MFC and LS_MFT series.
The reduction was conducted at 1350 °C for 45 min under Ar and the oxidation was conducted at 900 °C for 25 min under 21% O_2 balanced with Ar. The measurements contained two consecutive cycles and the second cycles were shown here (to exclude effects from volatile surface absorbates in the first cycle). The reference was calibrated to the oxidization state at the beginning of the second cycle. The calculated $\Delta\delta$ *vs.* *x* curves are shown in (c) for $(La_{1-x}Sr_x)(Mn_{1/3}Fe_{1/3}Cr_{1/3})O_3$ (LS_MFC) and in (d) for $(La_{1-x}Sr_x)(Mn_{1/3}Fe_{1/3}Ti_{1/3})O_3$ (LS_MFT) series, respectively. Noting that the δ values measured by TGA are relative and used to determine $\Delta\delta$ ($= \delta_{red} - \delta_{ox}$).

Figure 2.7c and 2.7d show the quantified Δδ *vs.* Sr molar ratio on the A site of LS_MFC and LS_MFT, respectively. The Δδ of LS_MFC exhibits an expected (normal) linear increasing trend with the Sr molar ratio on the A site. The linear trend is similar to those the widely reported compositions like (La,Sr)MnO_3,[31,32] corresponding to the increase of oxidation state of B site elements with Sr substitution of La on the A site.

Interestingly, Figure 2.7d displays an abnormal V-shape relation in Δδ *vs.* Sr molar ratio curve in LS_MFT, which is markedly different from the (normal) linear trend observed in LS_MFC. The Δδ of LS_MFT first descends with Sr doping level from $x = 0$ (Δδ = 0.124) to $x = 0.5$ (Δδ = 0.027) on the A site, and increases again to reach the maximum (Δδ = 0.170) when Sr fully occupies A site. In LS_MFT, the minimum of Δδ (0.027) occurs in LS55_MFT (*i.e.*, $x = 0.5$), in contrast to LS_MFC that has the minimum in L_MFC (*i.e.*, $x = 0$).

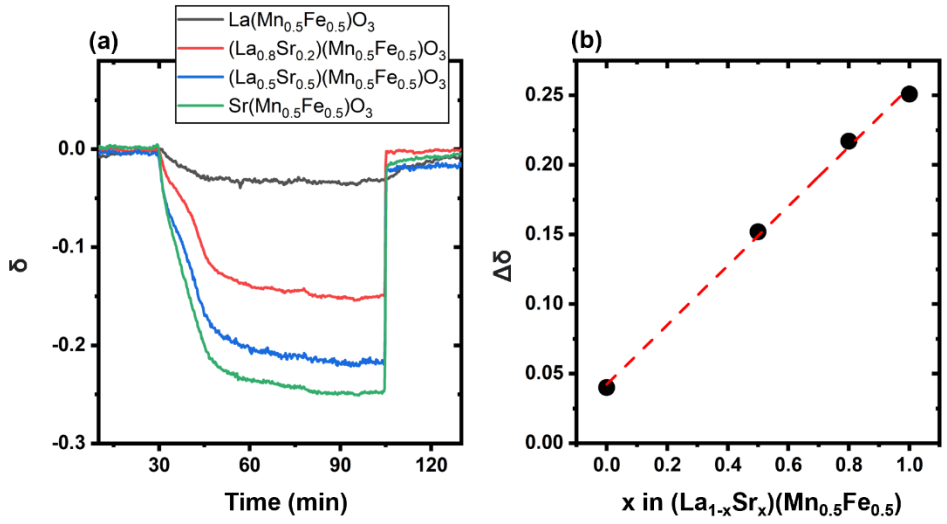

Figure 2. 8 Temperature programmed reduction measurements of $(La_{1-x}Sr_x)(Mn_{0.5}Fe_{0.5})O_3$
(**a**) Temperature programmed reduction measurements of $(La_{1-x}Sr_x)(Mn_{0.5}Fe_{0.5})O_3$. The reduction condition is at 1350 ºC for 45 min under Ar. The oxidation was conducted at 900 ºC for 25 min under 21% O_2 balanced with Ar. (**b**) The calculated Δδ vs. x in $(La_{1-x}Sr_x)(Mn_{0.5}Fe_{0.5})O_3$.

The only difference between LS_MFT and LS_MFC is the replacement of Cr by Ti, which caused the Sr doping effect to change from a linear to a V-shape trend. To further confirm that the V-shape correlates with Ti, a series of $(La_{1-x}Sr_x)(Mn_{0.5}Fe_{0.5})O_3$ were tested with the same TPR protocol and formed a linear

relation between Δδ and Sr molar ratio, as shown in Figure 2.8. Furthermore, we investigated how the Ti doping (with unchanged valence as we show latter) can tune the chemical properties of Mn and Fe at various Sr doping levels, which represents an interesting and intriguing finding.

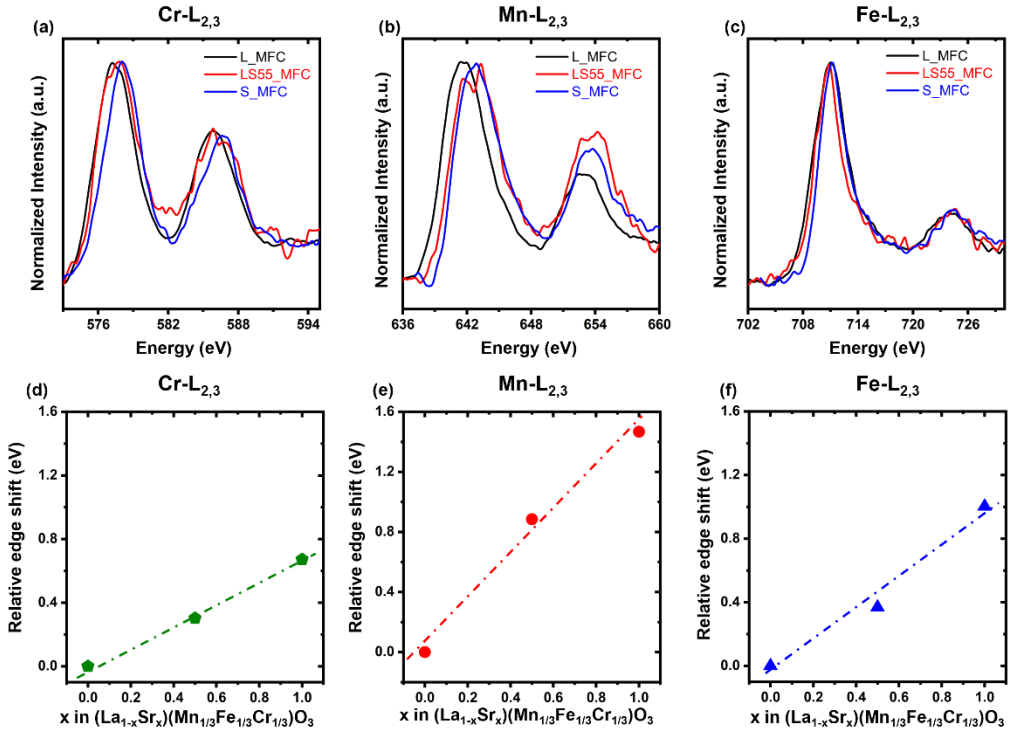

Figure 2. 9 Measured energy loss near edge structure of LS_MFC series.
(a) Cr-$L_{2,3}$, (b) Mn-$L_{2,3}$, and (c) Fe-$L_{2,3}$ The edge onset was calibrated to the energy with 20% of the maximum for the elements. The relative edge shift was calculated with respect to the edge energy of L_MFC. The relative edge shifts of (d) Cr-$L_{2,3}$, (e) Mn-$L_{2,3}$, and (f) Fe-$L_{2,3}$ in the LS_MFC series all show a linear relation vs. x in $(La_{1-x}Sr_x)(Mn_{1/3}Fe_{1/3}Cr_{1/3})O_3$.

To investigate the underlying mechanism that results in the different Δδ *vs.* Sr molar ratio curves shown in Figure 2.7c and d, we measured the chemical shift of B-site elements of LS_MFC and LS_MFT by EELS under an STEM in high-angle annular dark-field (HAADF) imaging mode. Figure 2.9 a-c show the energy loss near edge structure (ELNES) of the Cr-$L_{2,3}$, Mn-$L_{2,3}$ and Fe-$L_{2,3}$ peaks with different Sr molar ratios in the LS_MFC series. The intensities of all spectra were computed and normalized to the intensity of the highest peak (set to be 1 as the reference value). To quantify the chemical shift of specific elements, the energy loss where the edge energy reaches 20% of its peak maximum is taken as the edge onset. In general,

the energy onset position of 3*d* transition metals L edge shifts to higher energy-loss position for higher valence state.[132] Figure 2.9 d-f show the computed relative edge shift of the Cr-$L_{2,3}$, Mn-$L_{2,3}$, and Fe-$L_{2,3}$ peaks in the LS_MFC series, calculated by subtracting the energy edge from that of L_MFC (as the reference; relative edge shift = 0). The Cr-$L_{2,3}$, Mn-$L_{2,3}$ and Fe-$L_{2,3}$ peaks all shift linearly to higher energy with increasing Sr molar ratio, which suggests increased valence of Cr, Mn, and Fe. The increasing oxidation state of B-site elements with higher Sr molar ratio correlates well with the oxygen non-stoichiometry measurements of the LS_MFC series shown in Figure 2.7c.

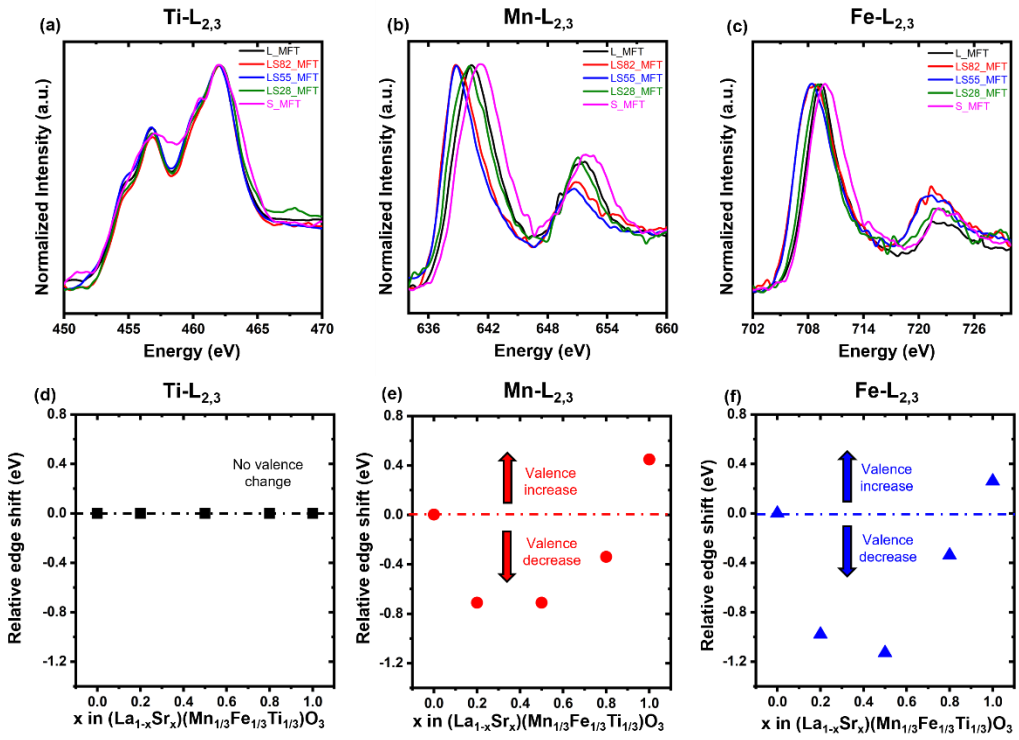

Figure 2. 10 Measured energy loss near edge structures in LS_MFT series.
(a) Ti-$L_{2,3}$, (b) Mn-$L_{2,3}$, (c) Fe-$L_{2,3}$. The edge onset was calibrated to the energy with 20% of the maximum for the elements. The relative edge shifts were calculated with respect to the edge energy of the L_MFT. The relative edge shift of the (d) Ti-$L_{2,3}$ was at zero, indicating no chemical shift of Ti. (e, f) The relative edge shifts of Mn and Fe, which shows a shift to lower energy (decreasing valence state), followed by a shift to higher energy (increasing valence state) as *x* in $(La_{1-x}Sr_x)(Mn_{1/3}Fe_{1/3}Ti_{1/3})O_3$ is increased.

As a comparison, Figure 2.10 a-c shows the Ti-$L_{2,3}$, Mn-$L_{2,3}$ and Fe-$L_{2,3}$ in the LS_MFT series with the calculated relative shift of the corresponding elements. The dash lines drawn in Figure 2.10 d-f represent the reference state (L_MFT) for comparison. The Ti-$L_{2,3}$ peak stays at the zero-edge shift, which implies no oxidation state change of Ti regardless of the Sr molar ratio. Compared to Mn and Fe, Ti has a much

higher oxygen vacancy formation energy in both $SrTiO_3$ and $LaTiO_3$, based on the DFT calculations shown in Figure 2.1. Therefore, we conclude that aliovalent doping keeps Ti at 4+ charge state and Ti^{4+} does not participate in the redox reaction. Meanwhile, the relative edge shift of the Mn-$L_{2,3}$ and Fe-$L_{2,3}$ peaks maintained a parabolic shape first (x = 0 to 0.5) with an edge shift (0 to -0.4 eV) to a lower energy (oxidation) state, but then shift (-0.76 to 0.45 eV) to a higher energy (oxidation) state as from x = 0.5 to 1. The evolution of Mn and Fe in terms of the oxidation state followed the similar the V-shape behavior in the previous $\Delta\delta$ measurements shown in Figure 2.7d. This suggests that the oxygen non-stoichiometry of LS_MFT is controlled by oxidation state of Mn and Fe. In LS_MFT82 and LS_MFT55, the edge onset positions of Fe and Mn were close to each other because the edge onset might be sensitive to the lowest oxidation state. Therefore, it is possible that charge states like Mn^{2+} exist in LS82_MFT and LS55_MFT.

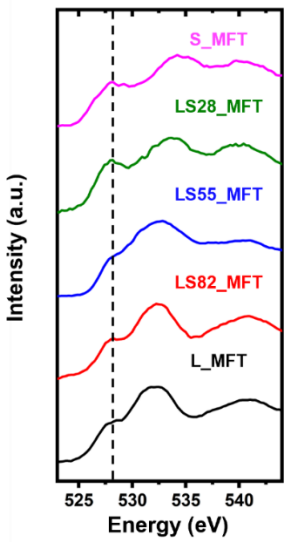

Figure 2. 11 O K-edge EELS spectra of LS_MFT with varying Sr molar ratio.

Another important scientific question we investigated is the charge balance in the LS_MFT series. Sr doping should introduce extra holes in the perovskite structure. However, with 0 to 50% Sr molar ratios, we only observed a fixed-valence Ti and valence-decreasing Mn/Fe. Hence, there must be other components in the LS_MFT series to accommodate the extra holes from Sr doping. We suggest that the charge compensation can be accomplished by the oxygen vacancy formation. Thus, we further investigated the O K edge EELS spectra in the LS_MFT series, as shown in Figure 2.11. The vertical dash line labels

the pre-peak that has been correlated to the oxygen vacancy formation in prior work.[133] The decrease in pre-peak intensity implies oxygen vacancy formation. In Figure 2.11. we can observe that the pre-peak has an obvious intensity decrease from L_MFT to LS55_MFT, followed by an increase from LS55_MFT to S_MFT. This finding indicates that oxygen vacancy formation in LS55_MFT and the oxygen vacancy participated in the charge compensation of Mn and Fe with decreasing oxidation state. We also applied a similar method to quantify the relative shift of O K shown in Figure 2.12. Here, we noticed that the relation of O K edge shift with the Sr molar ratio also shows a volcan like shape. The increasing Sr doping from 0 to 50% resulted in a +0.5 eV increase in the relative energy shift in O K edge, which can be correlated with the energy shift of Mn and Fe to lower energy direction.

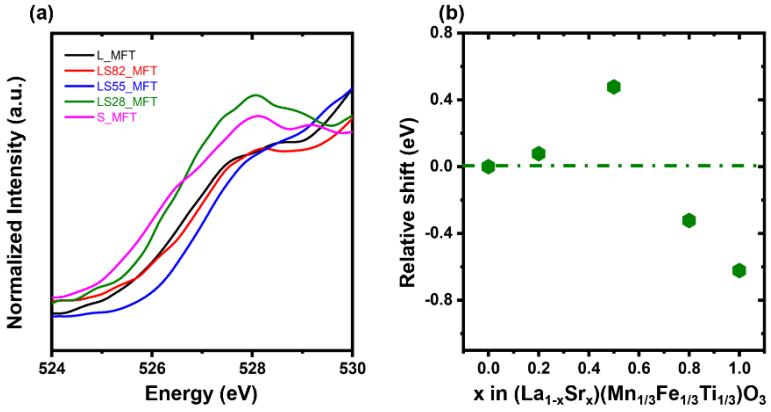

Figure 2. 12 O K edge onset of LS_MFT
(**a**) O K edge onset of LS_MFT. (**b**) Calculated relative shift of the O K edge with different Sr molar ratios in the LS_MFT series.

2.4 Conclusion

We discovered normal *vs.* abnormal Sr doping effects on oxygen non-stoichiometry (Δδ) in two series of medium-entropy CCPOs or compositionally complex perovskite oxides with three potentially redox active elements on the B site at equimolar fractions. The crystal structure depends on the La/Sr ratio on the A site, and it can vary from rhombohedral/orthorhombic to cubic. In the LS_MFC series with Mn, Fe and Cr on the B site, the Δδ exhibited a (normal) linear increasing relation with increasing Sr molar ratio on the A site. The linear relation between Δδ and Sr molar ratio was caused by the higher oxidation states of B

site elements as verified directly in EELS measurements. In the LS_MFT series with Mn, Fe and Ti on the B site, the $\Delta\delta$ exhibited an abnormal V-shape correlation with the Sr molar ratio, which follows the oxidation state evolution of Mn and Fe that also shows a V-shape dependence on the Sr molar ratio.

This study exemplifies that the coupling of A- and B-site doping effects in the emerging class of compositionally complex perovskite oxides can result in unexpected phenomena. Understanding of the complex interplays of multiple redox active elements on the B site, interacting with aliovalent doping on the A site, can provide new opportunities and strategies to search and tailor new redox active compositionally complex oxides for thermochemical looping.

Acknowledgement

Chapter 2, in full, is a reprint of the material as it appears in Dalton Transaction 2023. D. Zhang, J. Park, B. Xu, C. Liu, W. Li, X. Liu, Y. Qi and J. Luo. The dissertation author was the primary investigator and author of this paper.

CHAPTER 3. Long- and short-range orders in 10-component compositionally complex ceramics

3.1 Introduction

Fluorite-based oxides are a fascinating class of functional and structural ceramics with applications in solid oxide fuel cells (SOFCs)[134,135] and thermal barrier coatings (TBCs), [136–138] amongst other areas. They exhibit versatile compositional space and structural diversity. Here, the cubic fluorite ($AO_{2-\delta}$), as well as the disordered defect fluorite (A_4O_7), is the basis structure. The cubic pyrochlore ($A_2B_2O_7$) and orthorhombic weberite-type (A_3BO_7) structures represent two common derivative superstructures (of $2 \times 2 \times 2$ and $\sim 2 \times \sim\sqrt{2} \times \sim\sqrt{2}$, respectively) with ordered cations and oxygen vacancies[139]. The phase transformations between these structures further enable tailoring of thermal, mechanical, and other physical properties, including the radiation resistance[140,141]. Researchers have investigated the order-disorder transition (ODT) in fluorite-based oxides using X-ray diffraction,[142,143] Raman spectroscopy,[144] transmission electron microscopy, [145,146] X-ray absorption near edge spectroscopy (XANES),[147] and neutron total scattering.[148,149] The investigation can be conducted at different length scales to probe both long- and short-range orders. Researchers discovered that the oxygen anion displacement from 48*f* to 8*a* is the major cause of the long-range fluorite-to-pyrochlore ODT in 2- or 3-component oxides.[142,149,150] In addition, weberite-type short-range ordering has been reported in long-range-disordered defect fluorite structure. [139,151,152] For example, Drey *et al.* proposed that oxygen anion migration can create seven-coordinated Zr sites to form weberite-type short-range ordering in $Ho_2(Ti_{2-y}Zr_y)O_7$.[153] These authors suggested that the formation of weberite-type nanodomains of different orientation can trigger the long-range disordering to form defect fluorite. In general, how the long- and short-range ordering *vs.* disordering form, interact, and affect various physical properties represent open scientific questions. In a fundamental and broader perspective, elucidating and controlling ordering *vs.* disordering at different length scales can open a window to tailor various physical properties.

In the last a few years, high-entropy ceramics (HECs), which possess high configurational entropy and compositional disorder, attracted great research interest. Many studies have been conducted to fabricate and characterize high-entropy rock-salt,[154] perovskite, [155,156] fluorite [6,157–161] (including defect fluorite [6,158,159]), pyrochlore, [161–164] weberite,[164] fergusonite,[164] spinel oxides, [165] as well as high-entropy (MB_2, MB, M_3B_4, MB_4 and MB_6) borides, [7,166–169] carbides, [2,8,170] (MSi_2 and M_5Si_3) silicides,[171] nitrides,[172,173] and fluorides[174], amongst others.[175,176] In particular, high-entropy fluorite-based oxides have been reported for potential applications as thermal barrier coatings (TBCs) due to their low and reduced thermal conductivity and proper mechanical properties (*e.g.*, moderate Young's moduli).[6,159–164] Furthermore, it was proposed to broaden HECs to compositionally complex ceramics (CCCs) to include non-equimolar compositional designs and/or long- and short-range ordering, which reduce the configurational entropy, but provide additional dimensions to tailor or improve physical properties. [164,175,177] The vast majority of prior studies focused on equimolar five-component (occasionally four- or six-component) HECs.[175,176] Three recent studies further explored many-component (*i.e.*, 10- to 21-compoment) non-equimolar CCCs (including ultrahigh-entropy compositions with long-range ordering).[164,178,179] Here, long-range pyrochlore-to-fluorite [178,179] and pyrochlore-to-weberite[164] phase transformations (including a redox-induced ODT[179]) have been reported. However, the atomic level phase transformation and ordering/disordering mechanisms in these many-component CCCs have not yet been investigated.

Thanks to their sensitivity, neutron diffraction and total scattering can provide high-quality data to characterize both long- and short-range orders. In 2020, Jiang *et al.* reported a study to combine neutron diffraction and total scattering to analyze high-entropy pyrochlore oxides.[180] In 2022, Wright *et al.* reported a neutron total scattering study to characterize the short-range ordering in five high-entropy rare earth niobates and tantalates (all in the long-range disordered defect fluorite structure).[158] Both studies investigated 4- to 6-component equimolar or near-equimolar compositions, and they did not observe (therefore did not investigate) any ODT. Thus, the atomic level mechanisms of the compositionally induced ODT in HECs and CCCs, as well as the interaction and competition of short- and long-range ordering *vs.*

disordering, have not yet been characterized by neutron diffraction or total scattering. These open scientific questions, which become more interesting and intriguing in many-component CCCs with high (or ultrahigh) configurational entropy and compositional disorder, motivated this study.

Herein, we designed a series of 10-component compositionally complex fluorite-based oxides with the following formula: $[(Pr_{0.375}Nd_{0.375}Yb_{0.25})_2(Ti_{0.5}Hf_{0.25}Zr_{0.25})_2O_7]_{1-x}[(DyHoErNb)O_7]_x$, denoted as "10CCFBO$_{x\text{Nb}}$" for brevity, where x represents the fraction of Nb or niobate in the formula. This series of 10CCFBO$_{x\text{Nb}}$ composites all possesses single phase as confirmed by multi-scale characterization, with a long-range pyrochlore to defect fluorite ODT occurring at $x \sim 0.81 \pm 0.01$. In addition, weberite-type short-range ordering was found for $x > 0.5$, interacting and competing with the long-range ODT. The weberite-type short-range ordering and pyrochlore long-range ordering and their interplay in 10CCFBO$_{x\text{Nb}}$, along with how the ODT takes place at the atomic scale, were revealed by combining the state-of-the-art neutron diffraction and neutron total scattering, along with Rietveld refinements and small-box modelling of pair distribution functions (PDFs). In addition to uncovering the atomic level ODT mechanism and the competition of long- and short-range ordering *vs.* disordering, we observed unusual phase stability in the 10CCFBO$_{x\text{Nb}}$ (in contrast to well-established criteria for ternary oxides) and the correlation of thermal conductivity with the emergent of short-range ordering instead of the long-range ODT.

3.2 Experimental Section

3.2.1 Synthesis and Fabrication of Materials

All oxide precursors were purchased from US Research Nanomaterials Inc (Houston, TX). Powder precursors of the pyrochlore endmember $(Pr_{0.375}Nd_{0.375}Yb_{0.25})_2(Ti_{0.5}Hf_{0.25}Zr_{0.25})_2O_7$ and fluorite endmember $(DyHoErNb)O_7$ were first prepared separately. For each endmember, binary oxides were weighted, put in Y_2O_3-stablized ZrO_2 jars with 10 mL isopropanol, and planetary ball milled for 24 hours (using a PQN04 planetary miller, Across International) in parallel. After drying the powder at 75 °C overnight, we mixed the powder of two endmembers with appropriate molar ratios to fabricate a series of twelve 10CCFBO$_{x\text{Nb}}$

or $[(Pr_{0.375}Nd_{0.375}Yb_{0.25})_2(Ti_{0.5}Hf_{0.25}Zr_{0.25})_2O_7]_{1-x}[(DyHoErNb)O_7]_x$ specimens for x = 0, 0.02, 0.25, 0.5, 0.75, 0.8, 0.812, 0.825, 0.85, 0.9, 0.98 and 1, respectively. The nominal compositions are based on the weights of oxide precursors used in the synthesis, which are consistent with energy dispersive X-ray spectroscopy (EDS) measurements of the synthesized specimens within the typical EDS quantitative errors. The mixtures were placed in poly(methyl methacrylate) vials with tungsten carbide inserts and balls for high-energy ball milling for 100 min (875 cycles/min using a SPEX 8000D miller, SPEX SamplePrep, USA). Finally, the powder was uniaxially pressed into 13 mm diameter pellets and placed on a Pt foil covered Al_2O_3 crucibles for sintering. The Pt foil prevented the reaction between green body pellets and crucibles. The pellets were sintered at 1600 °C in air for 24 hours and furnace cooled to room temperature. The sintered pellets were grinded and polished for characterization.

3.2.2 Phase Identification and Compositional Analysis

Synthesized specimens were characterized by X-ray diffraction (XRD, Miniflex II diffractometer, Rigaku, Japan) to probe the crystal structure. XRD was operated at 30 kV and 15 mA to collect the spectra with 0.02° step size and 2 s dwell time. Rietveld refinements of XRD were conducted using GSAS II to confirm the crystal structure and measure the lattice parameters and theoretical density.

Scanning electron microscopy (SEM, FEI Apero) was applied to examine the microstructure and elemental homogeneity of all specimens. Specimens for SEM characterization were hot mounted in acrylic and polished [178]. Elemental maps were generated using energy dispersive X-ray spectroscopy (EDS, Oxford N-MAX) to examine the compositional homogeneity with a 20kV and 3.2A electron beam.

Scanning transmission electron microscopy (STEM) specimens were prepared by a dual-beam focused ion beam (FIB, FEI Scios Dualbeam). The STEM images and EDS analysis were obtained using a 300 kV, double aberration-corrected STEM (JEOL JEM-ARM300CF, Japan) with a high-angle annual dark field (HAADF) detector.

3.3.3 Neutron Diffraction and Rietveld Refinements

Neutron diffraction data were collected at the VULCAN diffractometer, at the Spallation Neutron Source (SNS), at the Oak Ridge National Laboratory (ORNL) [181]. Ten 10CCFBO$_{x\text{Nb}}$ samples were sintered pellets with 10 mm in diameter and 2.5 mm in thickness. The diffraction experiments were carried out at 290 K. All data shown in this paper used diffraction data from detector Bank 2 by optimizing the neutron path to reduce the neutron absorption.

The Rietveld refinements of all diffraction patterns were done with GSAS software. The refined parameters included the histogram scale factor, lattice parameter, isotropic atomic displacement parameters for A and B site metal cations and all oxygen positions (U_{a}, U_{b}, $U_{\text{O}(48f)}$, $U_{\text{O}(8b)}$, $U_{\text{O}(8a)}$), 36 coefficients of Chebyshev polynomial background, 2 coefficients describing Gaussian contributions to the Bragg peak shapes and finally the absorption factor due to elements like Dy. The pyrochlore structure does not have much flexibility for a cation position change and the only positional parameter allowed to be refined is the position u of O(48*f*) at (u, 1/8, 1/8); noting that we adopt "u" here for the positional variable since "x" is used to denote the composition. The occupancy of three oxygen sites were also refined while maintaining the site balance: 48 × O(48*f*) + 8 × O(8*b*) + 8 × O(8*a*) = 56 O sites per unit cell.

3.3.5 Neutron Diffraction and Rietveld Refinements

Pair distribution function (PDF) $G(r)$ were obtained via neutron total scattering at Nanoscale-Ordered Materials Diffractometer (NOMAD BL-1B) at the SNS, ORNL. For 10CCFBO$_{x\text{Nb}}$ powder specimens (x = 0.75, 0.8, 0.85 and 1) were loaded into a 2.8 mm ID, 3 mm OD quartz capillary to a height of 30 cm with around 0.6 g total mass. The total scattering experiments were carried out at 290 K for a total accelerator proton charge of 8C, corresponding to about 92 min acquisition time at the full power. To produce the total scattering function $S(Q)$, the background was subtracted for the data from six defector bank and the data were normalized to the intensity of vanadium. This function was Fourier-transformed with a sliding Q_{max} to obtain the neutron weighted pair distribution functions, $G(r) = r[g(r) - 1]$. The shortest distance

correlations were transformed with a $Q_{max} = 31.4$ Å^{-1}. The momentum transfer, Q, is given as $Q = \frac{4\pi sin\theta}{\lambda}$, where θ and λ are the scattering angle and the neutron wavelength, respectively.

The analysis of PDF data was done with small-box modelling by the PDFgui software. Three different structures used to model the data were pyrochlore ($Fd\bar{3}m$), defect fluorite ($Fm\bar{3}m$) and weberite-type ($C222_1$) structures. The refined parameters for the pyrochlore, defect fluorite, and weberite-type structures are listed in the Supplementary Method section (in Supplementary Material). We note that there are more degrees of freedom for cation and anion displacements for the weberite-type ($C222_1$) structure. Hence, 27 parameters were refined for the space group $C222_1$. Multiple elements occupying A or B site were refined with the same XYZ position and ADP.

3.3.6 Thermal Conductivity Measurements

The thermal diffusivity was measured using a Laser Flash Analyzer (LFA 467 HT HyperFlash, NETZSCH, Germany). All measurements were conducted from room temperature (25 °C) up to 600 °C in an Ar gas environment, with five individual measurements at each temperature point. Thermal conductivity was determined from thermal diffusivity (α), density (ρ), and specific heat (c_p) with the following equation:

$$k_{measured} = \alpha \rho c_p \tag{3.1}$$

The thermal conductivity was further corrected for porosity based on the following equation [182]:

$$k = \frac{k_{measured}}{(1-P)^{\frac{3}{2}}} \tag{3.2}$$

3.3 Results and Discussion

3.3.1 Single-Phase Formation in 10-Component Oxides

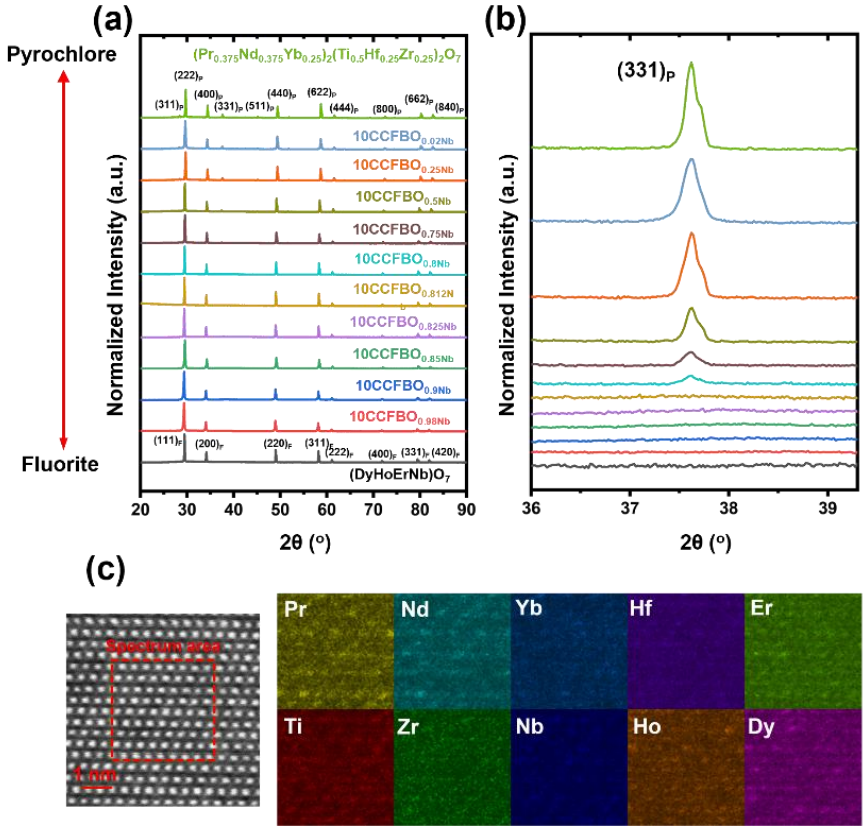

Figure 3. 1 phase characterization of 10CCFBO$_{x\text{Nb}}$ by XRD and STEM
(a) XRD spectra of the 10CCFBO$_{x\text{Nb}}$ series with pyrochlore and fluorite peaks indexed. **(b)** The enlarged pyrochlore superstructure $(331)_p$ peak area (36° to 39°). The long-range order-disorder transition (ODT) takes place between 10CCFBO$_{0.8\text{Nb}}$ (cyan) and 10CCFBO$_{0.812\text{Nb}}$ (dark yellow). Note that the small side peaks on the left of the $(331)_p$ peaks were resulted from Cu Kα1 and Kα2 radiation doublets. **(c)** STEM HAADF image of the pyrochlore 10CCFBO$_{0.5\text{Nb}}$ taken along the [110] zone axis and corresponding EDS elemental maps of the area indicated by the dashed red square in the STEM HAADF image. Bright spots in elemental maps mostly correspond to atomic columns. Since the TEM specimen thickness is > 20 nm, compositional clustering (*e.g.*, chemical short-range ordering) at ~1 nm scale cannot be measured by STEM EDS mapping. Thus, variations in the intensities of the bright spots in the EDS elemental maps are likely due to measurement noises or statistical fluctuations at the atomic scale (because there is only a limited number of atoms of a given element in an atomic column, particularly in a 10-component system). Additional STEM ESD mapping at a lower magnification shown in Suppl. Fig. S2 demonstrates compositional homogeneity at ~20-100 nm scale.

All XRD patterns of the 10CCFBO$_{x\text{Nb}}$ specimens exhibit either single-phase defect fluorite A_4O_7 ($Fm\bar{3}m$) or single-phase pyrochlore $A_2B_2O_7$ ($Fd\bar{3}m$) structure (Figure 3.1a), which can be differentiated by the $(331)_p$ superstructure peak due to the cation and oxygen anion ordering in the pyrochlore structure. No secondary phase was detected in XRD (Figure 3.1a) or EDS elemental mapping (Figure 3.2). There is an ODT from ordered pyrochlore to disordered defect fluorite structure between 10CCFBO$_{0.8\text{Nb}}$ and

$10CCFBO_{0.812Nb}$, evident by the vanished $(331)_p$ superstructure peak in Figure 3.1b. Here, we monitor the ODT via examining the $(331)_p$ peak, which has the highest intensity among the pyrochlore superstructure peaks. To further exclude the possible existence of fluorite and pyrochlore dual-phase region, SEM/EDS was applied to check the elemental homogeneity of $10CCFBO_{xNb}$, as shown in Figure 3.2. The images were taken by backscattered electron on polished pellet samples and EDS mapping showed homogeneous elemental distribution with no detectable secondary phase in all samples examined. The nanoscale elemental homogeneity was further confirmed by STEM based EDS elemental mapping, as shown in Figure 3.3 at the length scale of ~20-100 nm (including a grain boundary) and Figure 3.1c at the atomic scale (noting that the compositional inhomogeneity at ~1 nm scale cannot be measured by STEM EDS since the TEM specimen thickness is > 20 nm; thus, the variations in the ESD intensities at ~1 nm scale are likely due to measurement noises and statistical fluctuations at the atomic scale). Combining both microscale and nanoscale EDS mapping and XRD patterns confirms the formation of single-phase 10CCFBO with homogenous chemical distribution, to the best that we can reasonably characterize.

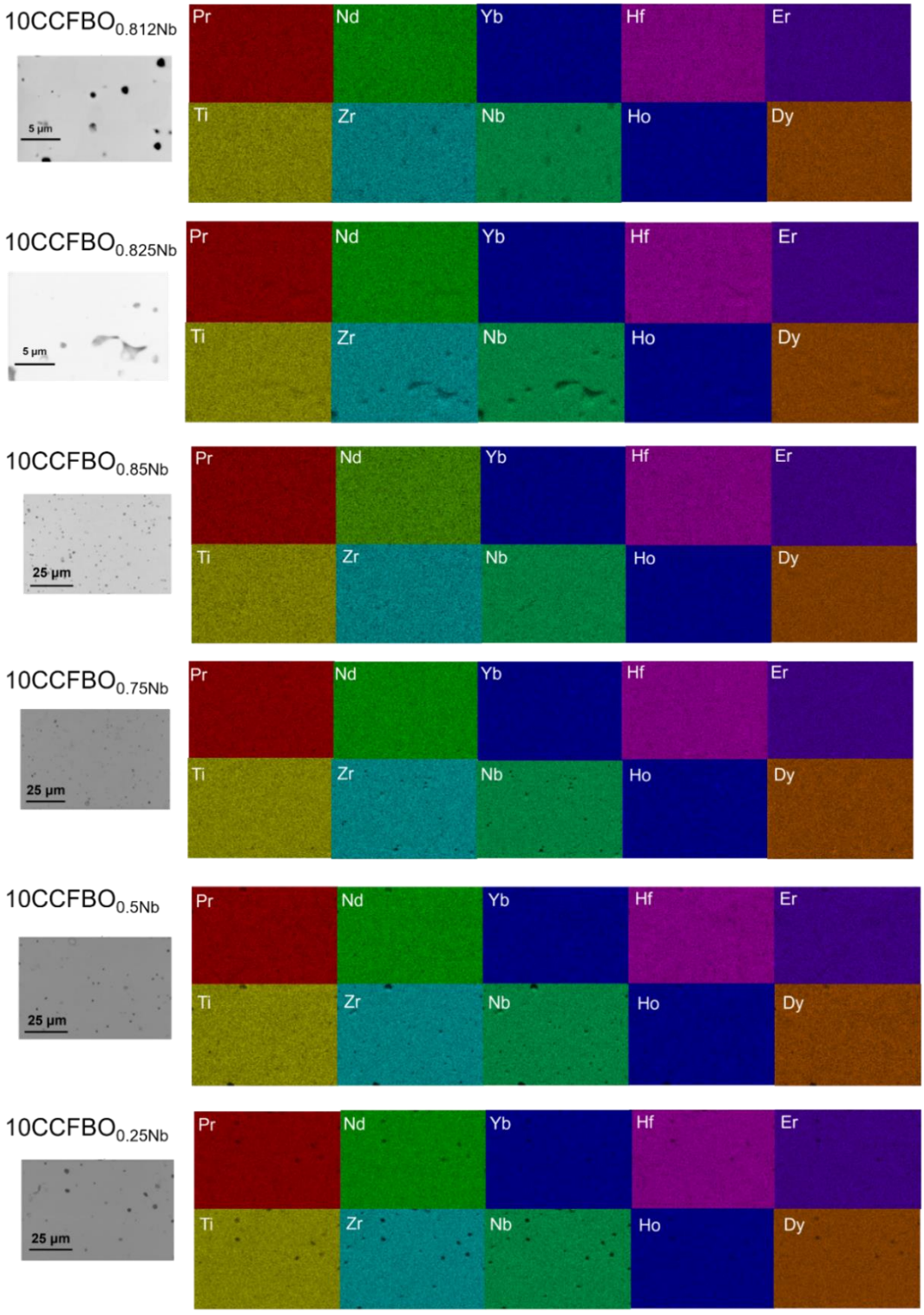

Figure 3. 2 SEM-EDS of six selected $10CCFBO_{xNb}$

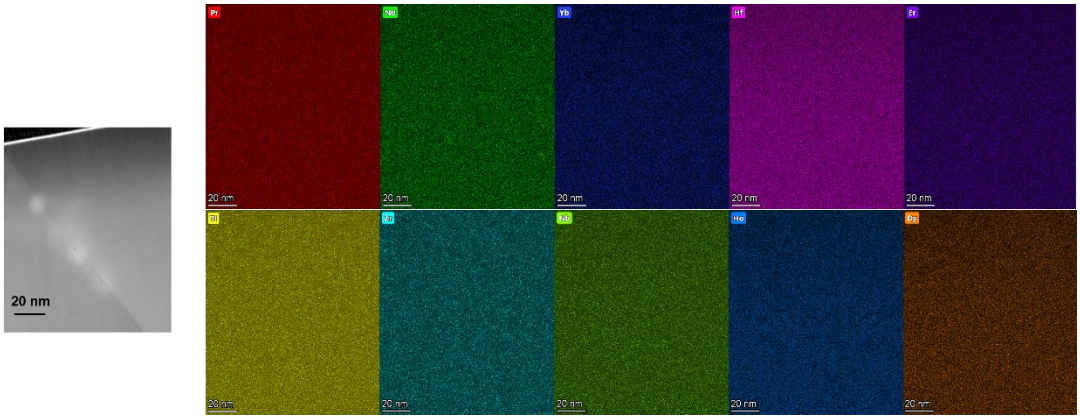

Figure 3. 3 STEM EDS elemental maps of 10CCFBO$_{0.5Nb}$
The mapping shows composition homogeneity at ~20-100 nm scale (including a grain boundary). The white spots along the grain boundary resulted from the beam damage (where EDS revealed no compositional inhomogeneity).

We recognize that inhomogeneous distribution of metal elements caused by chemical short-range ordering (noting that it differs from the weberite-type structural short-range disordering) likely exist in these 10CCFBOs. However, it is extremely challenging, if not infeasible, to directly characterize such compositional inhomogeneity at ~1 nm scale in these specimens with 10 different metal cations. For example, STEM EDS mapping averages the composition along the TEM specimen thickness direction (for at least > 20 nm) so that the compositional inhomogeneity at ~1 nm scale cannot be measured by the EDS elemental maps. Nonetheless, such compositional inhomogeneity caused by chemical short-range ordering likely exists, and it can further interact with long- and short-range structural orders to produce new and interesting phenomena.

The finding that the ODT takes place between x = 0.8 and 0.812 (where the percentage differences in many elements are close to errors so we cannot probe finer compositional step) without observable dual-phase region is somewhat a surprise. This finding in 10-component oxides (10CCFBO$_{xNb}$) is also in contrast to prior reports of a similar ODT in simpler $Ho_2Ti_{2-y}Zr_yO_7$, which suggested a pyrochlore and defect fluorite coexisting dual-phase region during ODT at y ~ 1.2.[148,153] In a 10-component system, the Gibbs phase rule allows the co-existence of up to 10 phases at equilibrium. Yet, this series of 10CCFBO$_{xNb}$ specimens all possess single-phase, where a pyrochlore-fluorite phase transformation occurs with increasing compositional variable x abruptly without a detectable dual-phase (or multi-phase) region. This may be

related to the so-called "high-entropy effect" (*i.e.*, the stabilization a single solid-solution phase due to its high configurational entropy [183–185]) that reduces or suppresses the dual- or multi-phase region (that will have lower configurational entropies). However, the underlying mechanism needs to be further investigated via thermodynamic modeling (that is non-trivial for a 10-component system and beyond the scope of this work).

3.3.2 Atomistic Mechanism of the Long-Range ODT

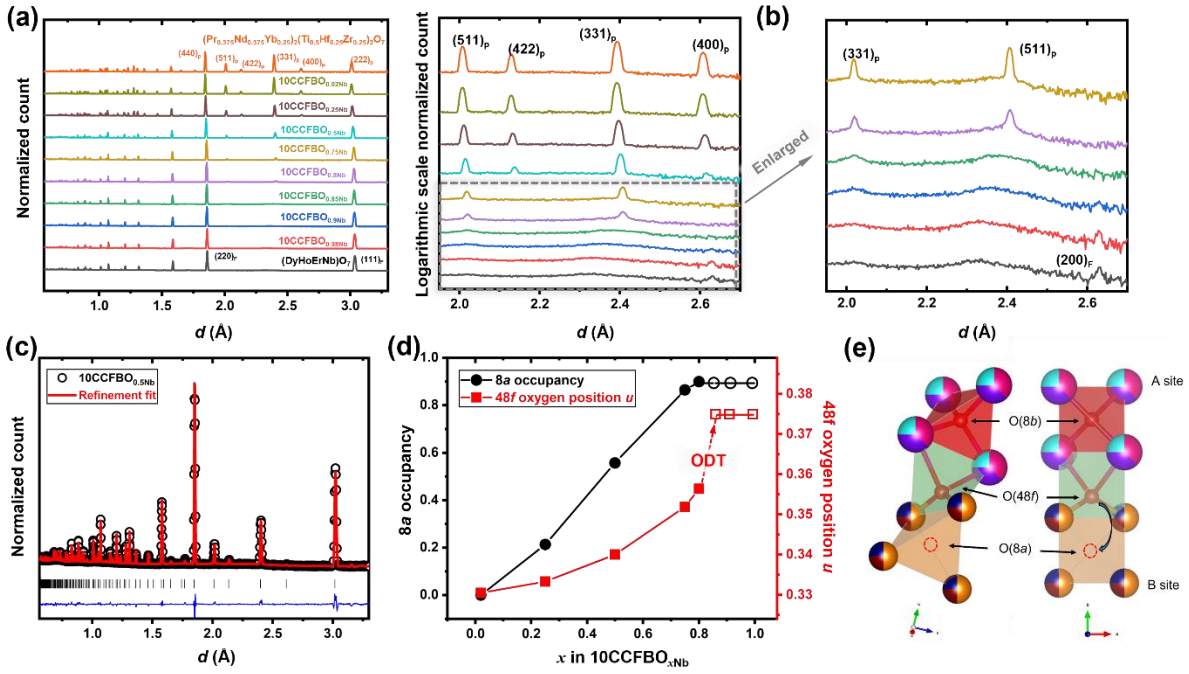

Figure 3. 4 Neutron diffraction analysis of 10CCFBO$_{x\text{Nb}}$
(a) Neutron diffraction patterns of the 10CCFBO$_{x\text{Nb}}$ series of specimens. **(b)** Enlarged area showing the (331) pyrochlore superstructure peaks. The long-range pyrochlore to fluorite transition (ODT) happens in between 10CCFBO$_{0.8\text{Nb}}$ and 10CCFBO$_{0.85\text{Nb}}$. Broad background peaks appear for 10CCFBO$_{x\text{Nb}}$ specimens with high Nb contents (for x = 0.75, 0.8, 0.85, 0.9, and 1), which are attributed to the presence of short-range weberite-type orders based on a subsequent analysis. **(c)** A measured neutron diffraction pattern of 10CCFBO$_{0.5\text{Nb}}$ (black circles) and the best Rietveld refinement fit with the $Fd\bar{3}m$ space group (red line). The blue line underneath represents the difference between experiment data and the refinement fit. The data fit for 10CCFBO$_{0.5\text{Nb}}$ with $Fd\bar{3}m$ yields R_w = 0.031, which indicates a good fit. The short black lines under experimental data show the peaks index for the $Fd\bar{3}m$ structure. **(d)** Positional parameter u for 48*f* oxygen at the (u 1/8 1/8) and equivalent positions in the pyrochlore unit cell and occupancy of oxygen vacancy at position 8*a* (1/8 1/8 1/8) with increasing x in 10CCFBO$_{x\text{Nb}}$. The dense symbols stand for the pyrochlore compositions, and the hollow ones illustrate the corresponding 8*a* occupancy and u in defect fluorite composition. The oxygen anion has an abrupt movement close to the ODT, indicated by the dash line. **(e)** Schematic illustration of oxygen position and migration from 48*f* to 8*a* with increasing x.

To analyze the atomic level mechanism of the long-range ODT, we conducted neutron diffraction experiments at VULCAN, at SNS, ORNL. Ten 10CCFBO$_{x\text{Nb}}$ specimens were tested in a sequence at 290

K in air for structural analysis. Figure 3.4a shows all neutron diffraction patterns of the $10CCFBO_{x\mathrm{Nb}}$ series with a transition from pyrochlore to defect fluorite structure. Within the enlarged region of pyrochlore $(331)_p$ and $(511)_p$ superstructure peaks shown in Figure 3.4b the intensity of superstructure peaks gradually decreases and completely vanishes after $x > 0.8$, which confirms the ODT observed from XRD. In the neutron diffraction, the $10CCFBO_{x\mathrm{Nb}}$ near the ODT (x = 0.75, 0.8, 0.85, 0.9, 0.98 and 1) also show diffuse scattering background peaks near the pyrochlore $(331)_p$ and $(511)_p$ peaks (but a careful analysis later suggests that they are not from pyrochlore ordering, but from short-range weberite ordering). These diffuse scattering background indicates short-range ordering in these $10CCFBO_{x\mathrm{Nb}}$, akin to previously reported fluorite systems, [142,149,186] which will be discussed in detail later.

The atomic level long-range structural evolution was analyzed by Rietveld refinements of the neutron diffraction patterns. For the pyrochlore ($Fd\bar{3}m$) structure, we chose to maintain an exact A:B ratio (1:1) and designate the larger ions to occupy A sites and smaller ions to take the B sites. Thus, the general ordered chemical formula for the $A_2B_2O_7$ pyrochlore can be written as:

- $[(Pr_{0.375}Nd_{0.375})_{1-x}(Dy_{0.5}Ho_{0.5})_xEr_{x/2}Yb_{(1-3x)/4}]_2[Yb_x(Ti_{0.5}Hf_{0.25}Zr_{0.25})_{1-x}Nb_{x/2}]_2O_7$ for $x < 1/3$ or
- $[(Pr_{0.375}Nd_{0.375})_{1-x}(Dy_{0.5}Ho_{0.5})_xEr_{(1-x)/4}]_2[Er_{(3x-1)/4}Yb_{(1-x)/4}(Ti_{0.5}Hf_{0.25}Zr_{0.25})_{1-x}Nb_{x/2}]_2O_7$ for $x > 1/3$.

To further verify this hypothesized configuration, we conducted Rietveld refinements of the neutron diffraction assuming several different cation arrangements, which all produced larger fitting errors (Figure 3.5). For example, the ordered pyrochlore structure of $10CCFBO_{0.8\mathrm{Nb}}$ has the ideal configuration of $(Pr_{0.075}Nd_{0.075}Dy_{0.4}Ho_{0.4}Er_{0.05})_2(Hf_{0.05}Ti_{0.1}Zr_{0.05}Nb_{0.4}Er_{0.35}Yb_{0.05})_2O_7$ (albeit some inevitable anti-site defects due to entropic effects). This structure can preserve exact A:B (1:1) stoichiometry and generate the best refinement fittings (with weighted profile residual $R_w \approx 0.03$).

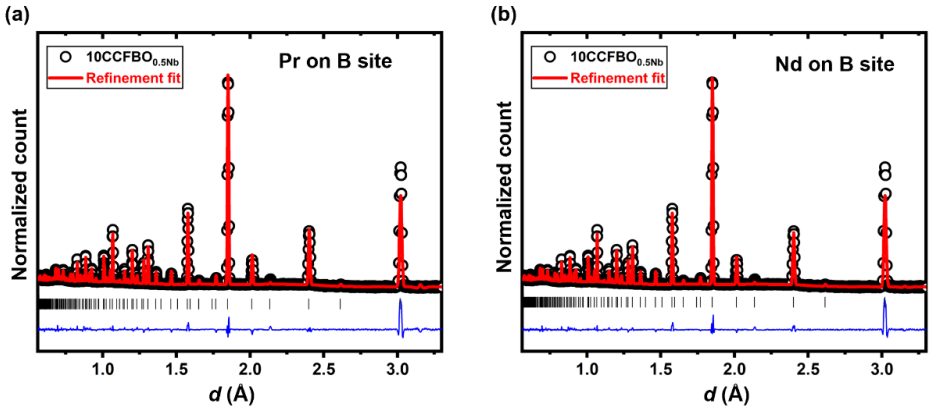

Figure 3. 5 The effects of different cation arrangements on the 10 CCFBO$_{0.5Nb}$ refinement results.
(a) $(Nd_{0.188}Dy_{0.25}Ho_{0.25}Er_{0.25}Yb_{0.125})_2(Pr_{0.188}Ti_{0.25}Hf_{0.125}Zr_{0.125}Nb_{0.25})_2O_7$ ($R_w \approx 0.052$) and
(b) $(Pr_{0.188}Dy_{0.25}Ho_{0.25}Er_{0.25}Yb_{0.125})_2(Nd_{0.188}Ti_{0.25}Hf_{0.125}Zr_{0.125}Nb_{0.25})_2O_7$ ($R_w \approx 0.055$).
It is noted that the (222) peak at around d = 3Å cannot be fitted well in these two scenarios, in comparison with proposed cation arrangement based on their radii.

In Rietveld refinements, cations on the A site were constrained to have the same isotropic atomic displacement parameters U_a as that for the B site (U_b). For oxygen anions in the pyrochlore structure ($Fd\bar{3}m$), there are three different positions: (1) 48*f* (*u*, 1/8, 1/8) (again, we used *u* here to differentiate *x* in 10CCFBO$_{x\text{Nb}}$); (2) 8*b* (3/8, 3/8, 3/8); (3) 8*a* (1/8, 1/8, 1/8) (vacant site). In the initial refinement of the pyrochlore endmember $(Pr_{0.375}Nd_{0.375}Yb_{0.25})_2(Ti_{0.5}Hf_{0.25}Zr_{0.25})_2O_7$, we assumed the O(48*f*) and O(8*b*) were fully occupied and O(8*a*) were fully vacant as a starting point. With increasing *x* in 10CCFBO$_{x\text{Nb}}$, the prior refinement results of oxygen anion parameters were used as an initial state for the subsequent compositions.

Table 3. 1 Parameters obtained via Rietveld refinements of 10CCFBO$_{x\text{Nb}}$

Sample	Lattice Parameter (Å)	Positional Parameter *a* of O1	O1 (48f) Occupancy	O3 (8a) Occupancy	Isotropic Thermal Vibration Parameters				Error R_w (%)
					U_{O1}	U_{O3}	U_A	U_B	
10CCFBO$_{0.02Nb}$	10.422	0.3305	1	0	0.01650	0	0.0146	0.0119	3.58
10CCFBO$_{0.25Nb}$	10.436	0.3333	0.9623	0.2067	0.0219	0.8	0.0145	0.0154	3.20
10CCFBO$_{0.50Nb}$	10.4578	0.34	0.8802	0.5703	0.0278	0.587	0.0107	0.0259	3.23
10CCFBO$_{0.75Nb}$	10.4786	0.3519	0.8661	0.8647	0.0458	0.164	0.0212	0.0184	3.47
10CCFBO$_{0.8Nb}$	10.4856	0.3564	0.8604	0.8802	0.0550	0.1104	0.0283	0.0182	3.56

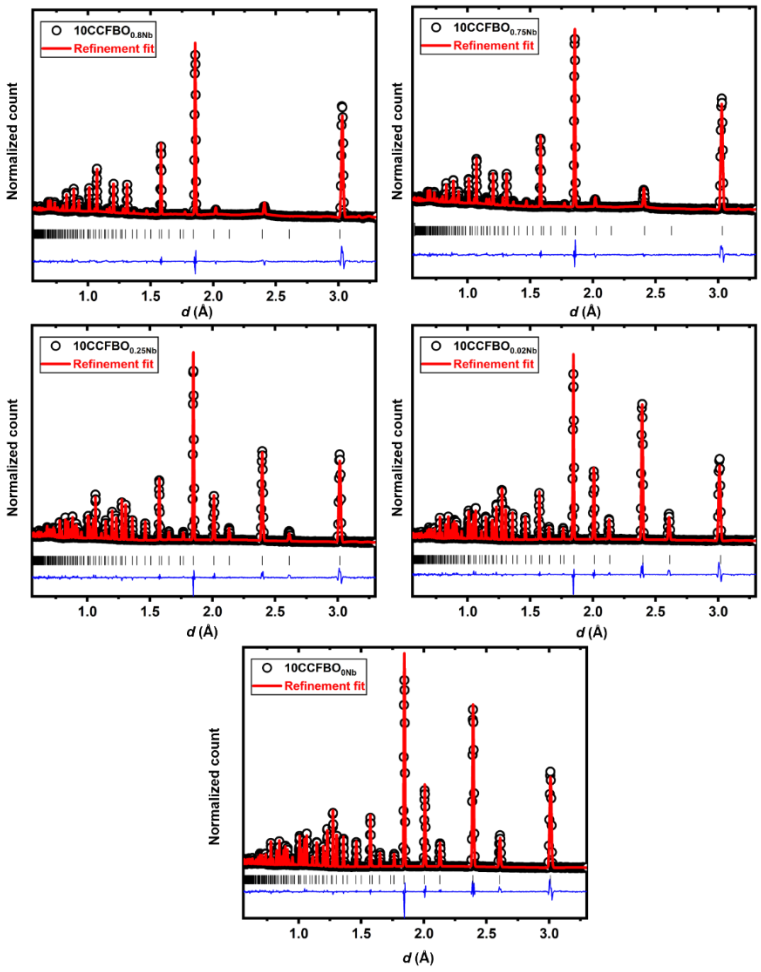

Figure 3. 6 Rievteld refinements of $10CCFBO_{xNb}$ with pyrochlore ($Fd\bar{3}m$) structure.

Figure 3.4c displays an example refinement result of $10CCFBO_{0.5Nb}$ with a R_w = 0.031, where the experimental data can be well fitted by the cubic pyrochlore model. All other Rietveld refinement results were documented in Figure 3.6, which all produced low fitting errors. There are two important parameters to understand the pyrochlore to defect fluorite transition: (1) the positional parameter *u* of O(48*f*) and (2) the occupancy of O(8*a*) site. During the ODT, *u* will move towards 0.375 and O(8*a*) will reach 0.875, which were reported for simpler ternary or quaternary fluorite-based oxides.[149,150,186]

Figure 3.4d shows the evolution of the refined O(8*a*) site occupancy and O(48*f*) positional parameter *u* with increasing compositional variable *x* in $10CCFBO_{xNb}$. The dense and hollow symbols represent the best fitted parameters in pyrochlore and defect fluorite, respectively. With increasing compositional variable *x*,

the oxygen atoms at occupied O(48*f*) position appear to migrate to nominally vacant O(8*a*) site, and "fill" some vacant O(8*a*) sites (with increasing 8a occupancy), while O(8*b*) site is kept fully occupied. In pyrochlore structure, O(48*f*) and O(8*a*) are the nearest neighbors, so that the migration between those two sites is possible (Figure. 3.4e). As *x* increases from 0 to 0.8 near the ODT, the occupancy of O(8*a*) increases from 0 (for $x = 0$) to 0.89 (for $x = 0.8$, which is almost equal to the ideal value of 0.875 for defect fluorite) with an almost linear increase and apparently no discontinuous jump at the ODT. The positional parameter *u* of O(48*f*) increases from 0.330 ($x = 0$) to 0.358 ($x = 0.8$) but with a rather abrupt jump from 0.358 ($x = 0.8$) to 0.375 ($x = 0.85$) during the ODT. This behavior indicates that the oxygen anions need to cross an energy barrier during the ODT. Thus, the ODT is likely a discontinuous phase transformation (with an order parameter vanished discontinuously).

3.3.3 Unique Character of the ODT and Unusual Phase Stability

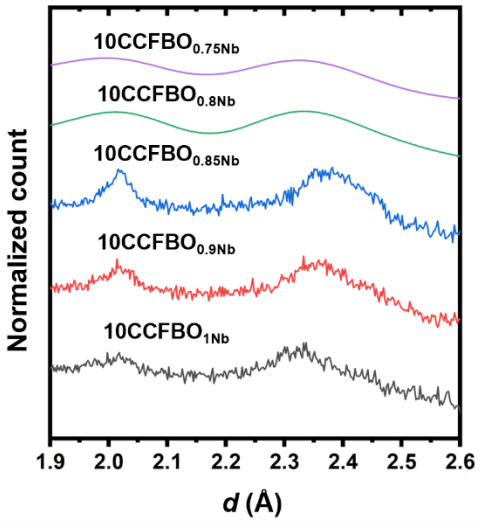

Figure 3. 7 Diffuse scattering background in neutron diffraction patterns of $10CCFBO_{x\mathrm{Nb}}$

On the one hand, our 10-component $10CCFBO_{x\mathrm{Nb}}$ series behave similarly in terms of oxygen anion movement during the long-range ODT as that reported for simpler 3-component $Y_2(Zr_yTi_{1-y})_2O_7$ [149,186]. The oxygen anion migration remains the key for the long-range ODT in this series of 10-component oxides, regardless of the ultrahigh-entropy compositions. On the other hand, one interesting difference between our $10CCFBO_{x\mathrm{Nb}}$ and simpler quaternary systems is that there is no observable dual-phase region (coexistence

of defect fluorite and pyrochlore) to the best that we can characterize. Such dual-phase regions were suggested for $Ho_2(Zr_yTi_{1-y})_2O_7$ [153] and $Y_2(Sn_yZr_{1-y})_2O_7$ [142]. In contrast, there was no detectable phase separation in $10CCFBO_{xNb}$ by neutron diffraction, XRD, and EDS elemental mapping in different length scales (Figure 3.1-3.4). However, we note that diffuse scattering of weberite-type shorting-range ordering was observed in both ordered pyrochlore $10CCFBO_{xNb}$ (x = 0.75 and 0.8) and disordered defect fluorite structures (Figure 3.7), which will be discussed in the subsequent section.

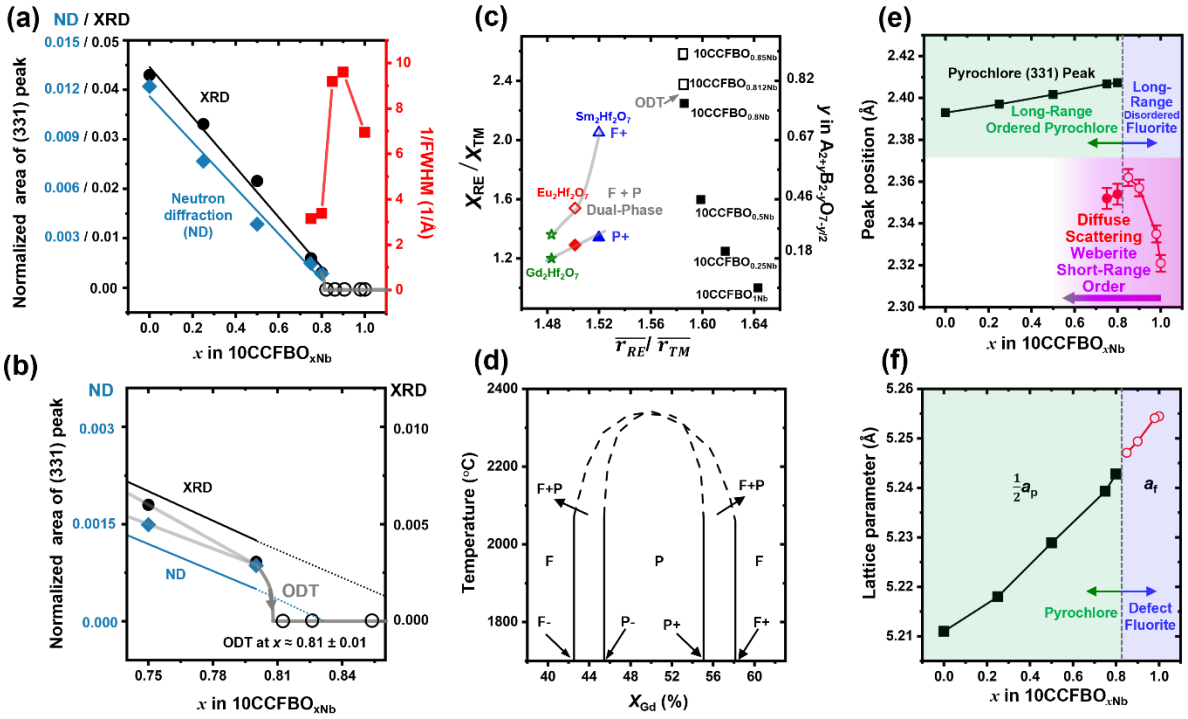

Figure 3. 8 Unusual character of ODT and phase stability

(a) Normalized area of the (331) peak *vs. x* curves for the 10CCFBO$_{x}$Nb series and linear least square fittings. The normalized peak areas were calculated based on the neutron diffraction (ND) patterns (indicated by the diamond symbols) and XRD (circle symbols). The left *y* axis was labeled with two scales for the data points calculated based on neutron/X-ray patterns. Reciprocal Full Width Half Maximum (1/FWHM) was determined from fitting the broad diffuse scattering peaks in neutron diffraction. The extrapolated *x* value for the vanishing of superstructure peaks from the best linear fittings are 0.82 $\pm$ 0.02 for neutron diffraction and 0.87 $\pm$ 0.03 for XRD, respectively. **(b)** Enlarged region near ODT. This analysis suggests an abrupt $(331)_p$ vanishment of the (331) superstructure peak during the ODT occurring at $x \sim 0.81$ (accelerated from the linear extrapolated values, suggesting a final discontinuous jump). **(c)** The position of the $(331)_p$ (represented by square symbols) and the diffuse scattering in long-range pyrochlore (dense circles for $x = 0.75$ and 0.8) and defect fluorite (hollow circles for $x = 0.85$, 0.9, 0.98 and 1) *vs. x* curves in the 10CCFBO$_{x}$Nb series. **(d)** Lattice parameter *vs. x* in the 10CCFBO$_{x}$Nb series. The pyrochlore lattice parameters (square symbols) are divided by two to correlate with those of the defect fluorite structure (circle symbols). All results here are based on neutron diffraction patterns obtained at the Vulcan diffractometer. **(e)** Plot of averaged cation radii ratio ($\overline{r_{RE}}/\overline{r_{TM}}$) and molar ratio ($X_{RE}/X_{TM}$) for the 10CCFBO$_{x}$Nb series, where a rather abrupt ODT occurs between $x = 0.8$ and $x = 0.812$. For references, the r_{RE}/r_{TM} *vs.* molar ratio (X_{RE}/X_{TM}) for the pyrochlore-fluorite dual-phase equilibria (phase boundaries) for three ternary $RE_2Hf_2O_7$ oxides are also plotted based on phase diagrams [ACerS-NIST database: $Gd_2Hf_2O_7$ (No. 9299), $Eu_2Hf_2O_7$ (No. 11158) and $Sm_2Hf_2O_7$ (No. 9333)], where the dual-phase compositional region increases with increasing r_{RE}/r_{TM} ratio. **(f)** The replotted phase diagram of $Gd_2Hf_2O_7$ (No.9299) to illustrate the dual-phase regions. The solid and hollow icons for the ternary hafnates in Panel (a) stand for the equilibrium compositions of pyrochlore (denoted as P+) and fluorite phase (denoted as F+) for the A/B > 1 or $X_{Gd} > 0.5$ side of the tie-line of the dual-phase region. Unlike ternary $RE_2Hf_2O_7$ oxides, the ODT in the10CCFBO$_{x}$Nb series takes place almost abruptly without an observable dual-phase region, despite it has a higher averaged cation radii ratio $\overline{r_{RE}}/\overline{r_{TM}}$.

To further analyze the character of this long-range ODT in 10CCFBO$_{x}$Nb, we plotted the normalized peak area of $(331)_p$ *vs. x* from both neutron diffraction and XRD patterns (Figure 3.8a). The diffuse

scattering identified (Figure 3.7) was also fitted as a single Gaussian/Lorentz peak, and the 1/FWHM (reciprocal Full Width Half Maximum) was calculated and also shown in Figure 3.8a. We note that the integrated peak area of $(331)_p$ has a virtually linear relation with compositional variable x for both neutron diffraction and XRD results (R^2 = ~0.99); the extrapolated x value of zero peak area was found to be 0.82 $\pm$ 0.02 for neutron diffraction and 0.87 $\pm$ 0.03 for XRD, respectively. Figure 3.8b displays the enlarged region of the ODT and the hollow symbols stood for $10CCFBO_{x}Nb$ with defect fluorite structure, for which the area of $(311)_p$ was set to 0. The ODT can be narrowed down to 0.81 ± 0.01 (between 0.8 and 0.812 according to XRD shown in Figure 3.1). A close-up shown in Figure 3.8b also suggests a rather abrupt vanishing of $(331)_p$ superstructure peak intensity near the ODT, deviated from the linear extrapolation of peak intensities far away from the actual ODT. Thus, both neutron diffraction and XRD exhibit an abrupt (accelerated) disappearance of the $(331)_p$ peak at the ODT (at x = 0.81 ± 0.01, *vs.* 0.82 and 0.87 projected from linear extrapolations). This observation can be explained from the abrupt O(48*f*) migration during the ODT revealed by Rietveld refinements of the neutron diffraction patterns (Figure 3.4d). It again suggests that this ODT is likely discontinuous phase transformation, where an order parameter (*e.g.*, that represented by the superstructure peak intensity) vanishes discontinuously at the ODT). In summary, the long-range order of $10CCFBO_{x}Nb$ vanishes almost continuously with increasing x, but with a final small abrupt (discontinuous) transition at the ODT that can be attributed to a small jump of the O(48*f*) position (Figure 3.4e).

Interestingly, as x decreases from 0.85 to 0.8 (passing through ODT with the merging of long-range pyrochlore order), a concurrent decrease of the 1/FWHM in the diffuse scattering is observed, which may represent the shrinkage of the domain (coherent) size of the short-range weberite-type order (discussed later) as a result of the interaction with the long-range pyrochlore order.

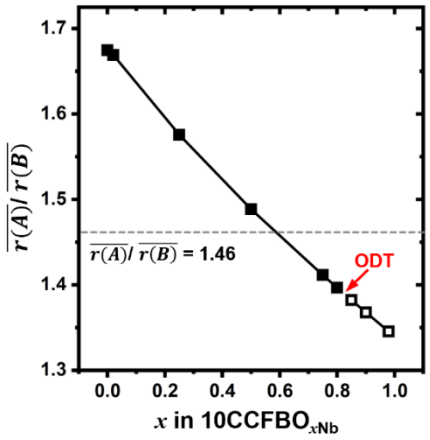

Figure 3. 9 The ratio of cation radii ($\overline{r(A)}/\overline{r(B)}$) vs. x curves in the 10CCFBO$_{x\text{Nb}}$ series
Here, $\overline{r(A)}/\overline{r(B)}$ is calculated assuming that smallest rare-earth cations Yb^{3+} and Er^{3+} occupy B site in the 10CCFBO$_{x\text{Nb}}$ series to maintain the exact $A_2B_2O_7$ stoichiometry. The dash line (r_A/r_B = 1.46) indicates the typical ODT (pyrochlore-fluorite) transition threshold for ternary $A_2B_2O_7$ oxides.[187] The ODT of these high-entropy compositions takes place at smaller $\overline{r(A)}/\overline{r(B)}$ ~ 1.39.

Prior studies suggested the ionic radii ratio (r_A/r_B) can determine the pyrochlore *vs.* fluorite phase stability in ternary $A_2B_2O_7$ (with ordered pyrochlore forming at r_A/r_B >1.46) [187]. In the 10CCFBO$_{x\text{Nb}}$ series, $\overline{r(A)}/\overline{r(B)}$ was calculated based on the chemical formula discussed above assuming that Yb^{3+} and Er^{3+} occupy the B site to keep an exact 1:1 ratio of A:B. The weighted average ionic radii ratio $\overline{r(A)}/\overline{r(B)}$ *vs.* x for the 10CCFBO$_{x\text{Nb}}$ series is shown in Figure 3.9. As x increases, the averaged ionic radii ratio ($\overline{r(A)}/\overline{r(B)}$) decreases. Compared to the pyrochlore formation threshold of r_A/r_B > ~1.46 in simpler $A_2B_2O_7$ ternary oxides, the 10CCFBO$_{x\text{Nb}}$ series show an ODT with a lower threshold of ~1.39 between 10CCFBO$_{0.8\text{Nb}}$ and 10CCFBO$_{0.85\text{Nb}}$. This appears to even more surprising as we have Yb^{3+} and Er^{3+} occupy the B site in 10CCFBO$_{x\text{Nb}}$, which intuitively should make the ordered pyrochlore structure unstable (prone to disorder). In most pyrochlores, larger sized rare earth elements usually occupy A site and smaller transition metal elements like Ti and Zr occupy B site. Thus, in the proposed model for 10CCFBO$_{x\text{Nb}}$, large size Yb^{3+} and Er^{3+} dwell at the B site to maintain exact A:B stoichiometry. Hence, $\overline{r(B)}$ has a larger value compared to the ionic radii of Zr and Hf in the typical ternary oxides [187].

We also calculated the ionic radii and molar ratio between all rare earth elements (RE = Pr^{3+}, Nd^{3+}, Yb^{3+}, Dy^{3+}, Ho^{3+}, and Er^{3+}) and all other transition metal elements (TM = Ti^{4+}, Zr^{4+}, Hf^{4+} and Nb^{5+}). Figure 3.8c shows the molar ratio X_{RE}/X_{TM} *vs.* ionic radii ratio $\overline{r_{RE}}/\overline{r_{TM}}$ for the $10CCFBO_{x\text{Nb}}$ series, along with those for three selected ternary $RE_2Hf_2O_7$ hafnates. For ternary hafnates, there are two phase boundary compositions (denoted at "P+" and "F+" for the rare earth element rich side of dual-phase tie-line), representing the equilibrium pyrochlore and fluorite compositions in the pseudo-binary phase diagram; see Figure 3.8d for an example of $Gd_2Hf_2O_7$ (replotted after ACerS-NIST phase diagram No. 9299). For these ternary hafnates, the molar ratio range of the dual-phase (F + P) region increases with the ionic radii ratio r_{RE}/r_{TM}. In contrast, the $10CCFBO_{x\text{Nb}}$ series has a virtually abrupt phase transition (ODT) between $10CCFBO_{0.8\text{Nb}}$ and $10CCFBO_{0.812\text{Nb}}$ without an observable (F + P) dual-phase region. This again suggests the uniqueness of this abrupt ODT (lacking a discernible dual-phase region) in the 10-component CCFBOs, deviating from the projection from ternary oxides (Fig. 3.8).

3.3.4 Short-Range Order and Its Interaction with Long-Range ODT

Diffuse scattering was found in $10CCFBO_{x\text{Nb}}$ near the ODT (for x = 0.75, 0.8, 0.85, 0.9, 0.98, and 1), which can be attributed to nanoscale weberite-type ordering (akin to those observed in simple oxides [147,188,189]), based on analysis of the peak position and its shift (Figure 3.8e), which are further confirmed by small-box modeling (discussed later). Interestingly, the short-range order can form in both disordered defect fluorite (x = 0.85, 0.9, 0.98 and 1) and barely ordered pyrochlore (x = 0.75 and 0.8).

To further illustrate this interaction, both the $(331)_p$ peaks in the pyrochlore structure (for x = 0, 0.25, 0.5, 0.75 and 0.8) and the diffuse scattering for weberite-type short-range ordering (for x = 0.75, 0.8, 0.85, 0.9, 0.98 and 1), respectively, were fitted as single Gaussian and Lorentz peaks, respectively. The peak position *vs.* x is displayed in Figure 3.8e. The square and circle symbols, respectively, in Figure 3.8e stand for the positions of $(331)_p$ and diffuse scattering, respectively. The reciprocal peak width (1/FWHM) *vs.* x of the fitted diffuse scattering is shown in Figure 3.8a.

As shown in Figure 3.8e, the peak position of $(331)_p$ undergoes a small increase with increasing x, which follows the same trend as in the measured lattice parameter because the defect fluorite endmember $(DyHoErNb)O_7$ has the larger lattice parameter than the pyrochlore endmember $(Pr_{0.375}Nd_{0.375}Yb_{0.25})(Ti_{0.5}Hf_{0.25}Zr_{0.25})O_7$ (Figure 3.8f). During the ODT (x = 0.8 to 0.85), the $(331)_p$ peak disappears, and peak position of the diffuse scattering moves slightly towards the higher d spacing. The appreciable position difference of $(331)_p$ peak (d = 2.407 Å) and diffuse scattering (d = 2.35 Å) at x = 0.8 suggests that the diffuse scattering cannot be attributed to broadening of the $(331)_p$ peaks, but it may represent weberite-type short-range ordering (*e.g.*, the (041) peak in the weberite-type structure $C222_1$ that broadens and merges with other peaks to become diffuse scattering).

Passing the ODT into ordered pyrochlore region with reducing x, the short-range order interacts with the long-range order, resulting in changes in both the width (Figure 3.8a, implying reduced domain sizes in long-range ordered region) and position (Figure 3.8e, virtually continuous at ODT, but with an altered slope with varying x) of the diffuse scattering.

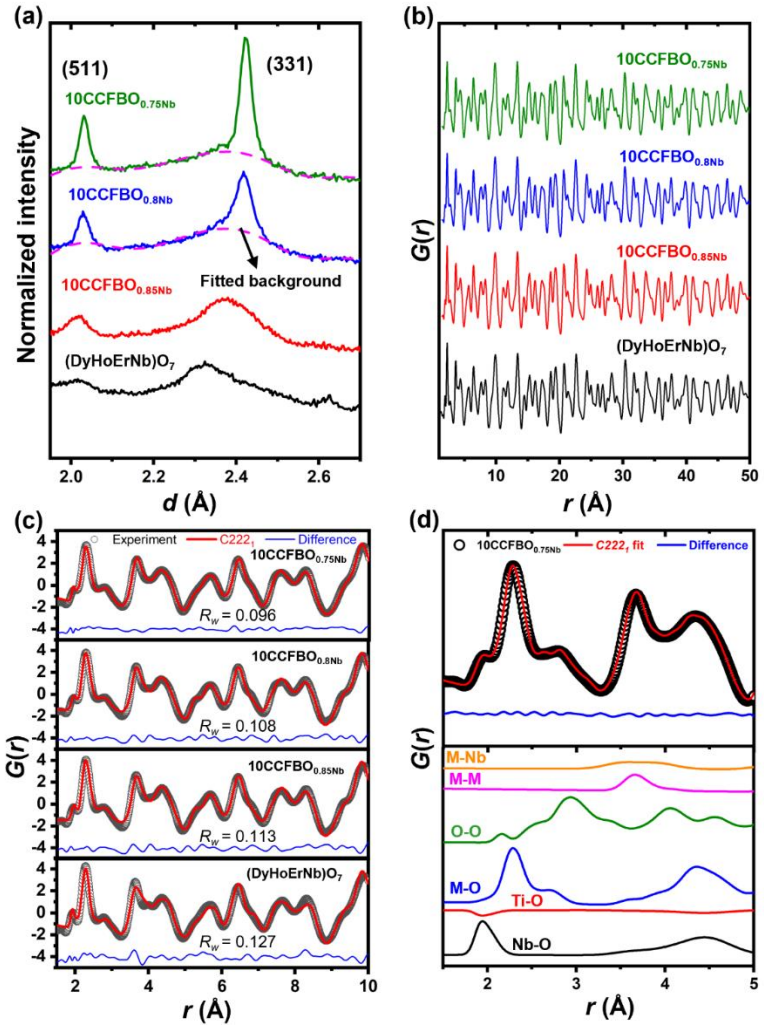

Figure 3. 10 Neutron total scattering results of 10CCFBO$_{x\text{Nb}}$
(a) Neutron total scattering patterns with background fitting near the (331) peak from NOMAD (for better probing short-range ordering) and **(b)** neutron pair distribution functions (PDF) of the compositions near the ODT. **(c)** Small-box modelling of four selected 10CCFBO$_{x\text{Nb}}$ (x = 0.75, 0.8, 0.85 and 1) with weberite-type $C222_1$ structures. **(d)** Partial PDFs of 10CCFBO$_{0.75\text{Nb}}$ modeled based on the weberite $C222_1$ structure. Here, M stands for Pr, Nd, Dy, Ho, Er, Zr and Hf. Black circles are the experimental data and red lines represent the model fittings. The partial PDFs for Nb-O and Ti-O show opposite trends in neutron scattering at the same position. The peak around 1.95 Å gradually vanishes with decreasing x in 10CCFBO$_{x\text{Nb}}$ because of the decreasing Nb content and increasing Ti content.

To further confirm hypothesized weberite-type short-range ordering in 10CCFBO$_{x\text{Nb}}$ more directly, we conducted neutron total scattering to probe the compositions near the ODT (x = 0.75, 0.8, 0.85 and 1) using the Nanoscale-Ordered Materials Diffractometer NOMAD (SNS, ORNL), which offer much improved sensitivity to probe short-range orders (in comparation with conventional neutron diffraction). The total

radial distribution function $G(r)$ is obtained by Fourier transform of the structure factor, $S(Q)$ for further analysis.

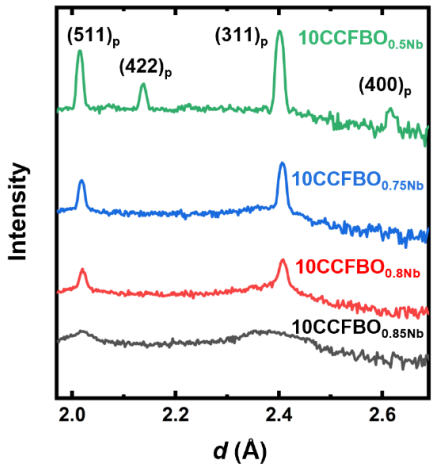

Figure 3. 11 Neutron diffraction patterns of $10CCFBO_{xNb}$ near the ODT

Figure 3.10a shows neutron diffraction data from bank 3 of the NOMAD in $(331)_p$ peak region for four $10CCFBO_{xNb}$ compositions (x = 0.75, 0.8, 0.85 and 1) near the ODT. Here, clearer diffuse scattering can be observed for all four compositions. The diffuse scattering of $10CCFBO_{0.75Nb}$ and $10CCFBO_{0.8Nb}$ were plotted by fitted Chebyshev backgrounds. Notably, no diffuse scattering can be observed at the $(331)_p$ region when x reaches 0.5 (Figure 3.11), suggesting the vanishing of the short-range order. Neutron pair distribution functions (PDFs) of the $10CCFBO_{xNb}$ series (Figure 3.10b) can provide information of short-range atomic arrangement. As x increases, the peaks at larger r values (r > 15 Å) slightly shift to higher r, which corresponds to the expansion of unit cell in concert with lattice parameters measured by conventional neutron diffraction at the Vulcan diffractometer (Figure 3.8f).

For the peaks at small r values (< 10 Å), all four compositions exhibit similar curve shapes, which suggest similar first and second nearest neighbors' environments. On a close look, the intensity of peak at around 1.95 Å decreases as x decreases.

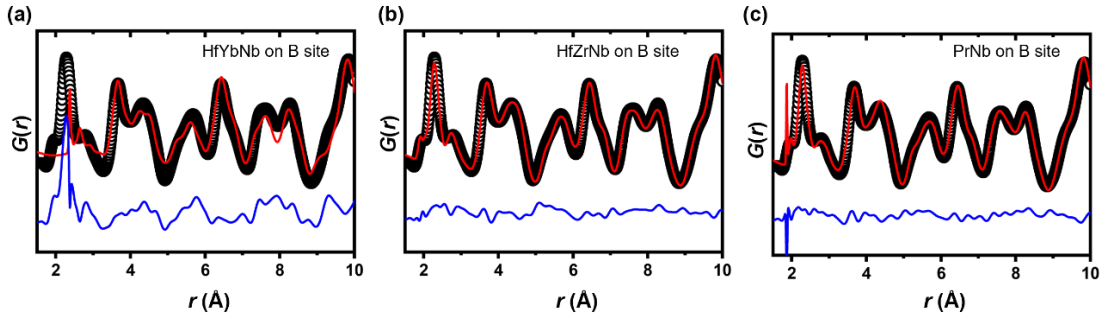

Figure 3. 12 Simuated G(r) curves assuming different atmoic structures in weberite-type ordering
(a) $(Pr_{0.0625}Nd_{0.0625}Ti_{0.094}Dy_{0.25}Ho_{0.25}Er_{0.25}Zr_{0.0417})_3(Yb_{0.125}Hf_{0.125}Nb_{0.75})O_7$
(b) $(Pr_{0.0625}Nd_{0.0625}Ti_{0.094}Dy_{0.25}Ho_{0.25}Er_{0.25}Yb_{0.0417})_3(Zr_{0.125}Hf_{0.125}Nb_{0.75})O_7$, and
(c) $(Pr_{0.0625}Nd_{0.0625}Ti_{0.094}Dy_{0.25}Ho_{0.25}Er_{0.25}Hf_{0.0417}Zr_{0.0417}Yb_{0.0417})_3(Pr_{0.187}Nb_{0.75})O_7$

To investigate this local structural evolution, small-box modelling was conducted using the PDFgui software. For each composition, three structural models were used to fit the PDFs: (1) pyrochlore ($Fd\bar{3}m$), (2) defect fluorite ($Fm\bar{3}m$), and (3) weberite-type ($C222_1$) structures. The same pyrochlore and defect fluorite models from previous refinements of long-range structure were adapted here for small-box modelling as the initial structures. For the weberite-type structure (A_3BO_7), we tried several combinations. The best fitting is achieved with the smallest error when Ti and Nb occupied the B site with coordination number of 6. For example, $10CCFBO_{0.75Nb}$ can be modelled as: $(Pr_{0.0625}Nd_{0.0625}Yb_{0.0417}Dy_{0.25}Ho_{0.25}Er_{0.25}Hf_{0.0417}Zr_{0.0417})_3(Ti_{0.25}Nb_{0.75})O_7$. The modeling results of other combinations with substantially larger errors were documented in Figure 3.12 for comparison. Notably, only the weberite-type structure can depict the low *r* region (< 10 Å) with the small errors (Figure 3.13 and 3.14). Neither pyrochlore nor defect fluorite model can produce the 1.95 Å peak. This suggests the presence of short-range weberite-type orders.

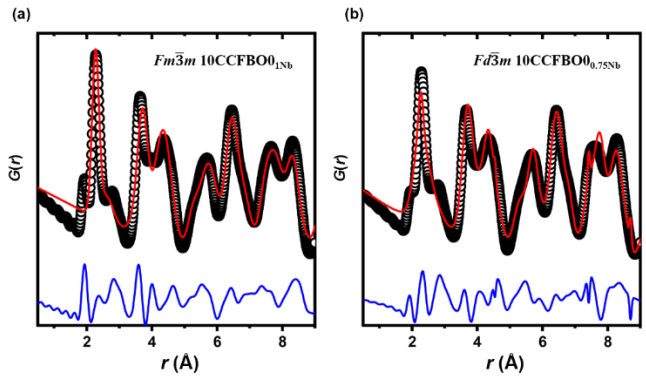

Figure 3. 13 Small-box modelling with defect fluorite and pyrochlore structure
(a) Small-box modeling of the PDF profile for $10CCFBO_{1Nb}$ fitted with the defect-fluorite ($Fm\bar{3}m$) structure. **(b)** Small-box modeling of the PDF profile for $10CCFBO_{0.75Nb}$ fitted with the pyrochlore ($Fd\bar{3}m$) structure.

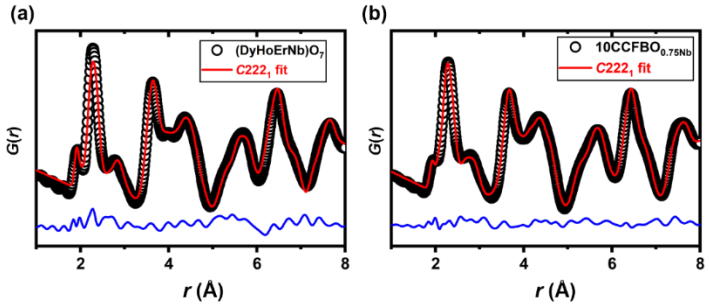

Figure 3. 14 Small-box modeling based on Weberite-type structure

Figure 3.10c displays the small-box modeling of all four compositions (x = 0.75, 0.8, 0.85, and 1) with the weberite-type $C222_1$ structure. The good fitting further confirmed the short-range ordering at smaller length scales (deviated from the long-range pyrochlore or defect fluorite ordering). Figure 3.10d shows the partial PDFs for several major bonds fitted with the weberite-type $C222_1$ structure in $10CCFBO_{0.75Nb}$, where M stands for all elements occupying the A site (Pr, Nd, Dy, Ho, Er, Yb, Hf and Zr) in A_3BO_7. The Nb-O and Ti-O signatures both locate at around 1.95 Å with opposite neutron scattering. As x decreases from 1 to 0.75, Ti gradually replaces with Nb on B site for weberite-type structure, which correlates well with the decreasing peak intensity at r = 1.95 Å. Additional partial PDFs results were shown in Figure 3.15. "Boxcar" refinement was applied to examine the short-range ordering deviation from the overall structure (Figure 3.16).[153,190] In general, the weberite-type $C222_1$ structure can produce better fitting results. In contrast, the exclusion of r-range below 5 Å that contained the first and second nearest neighbor polyhedral and

coordination substantially improved the R_w of the pyrochlore and defect fluorite structural fitting. As r_{min} further increases, both pyrochlore and defect fluorite fittings converge to values comparable to that of the weberite-type structure fitting. The pyrochlore structure fits better for $10CCFBO_{0.75Nb}$ and $10CCFBO_{0.8Nb}$, which is consistent with the analysis of long-range ordering above. For $10CCFBO_{0.85Nb}$, the pyrochlore and defect fluorite generated similar R_w values because this composition is near the ODT. Note that the defect fluorite endmember $(DyHoErNb)O_7$ (that has a long-range fluorite order with strong short-range weberite order) cannot be modeled as a pyrochlore structure with a reasonable error, which is consistent with our hypothesis.

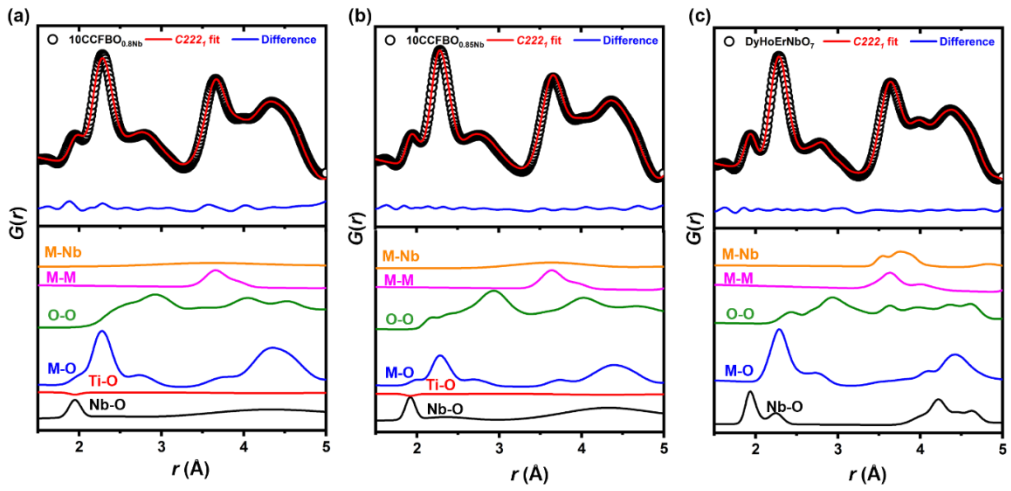

Figure 3. 15 Partial PDFs of $10CCFBO_{xNb}$
(a)$10CCFBO_{0.8Nb}$, **(b)**$10CCFBO_{0.85Nb}$, and **(c)** $(DyHoErNb)O_7$ modeled based on the weberite-type $C222_1$ structure. Here, M stands for other metal cations (Pr, Nd, Dy, Ho, Er, Zr and Hf; other than Nb). Black circles are the experimental data and red lines represent the model fittings. The partial PDFs for Nb-O and Ti-O show opposite neutron scattering at the same position. The peak around 1.95 Å gradually vanishes at decreasing x in $10CCFBO_{xNb}$ because of the decreasing Nb content and increasing Ti content.

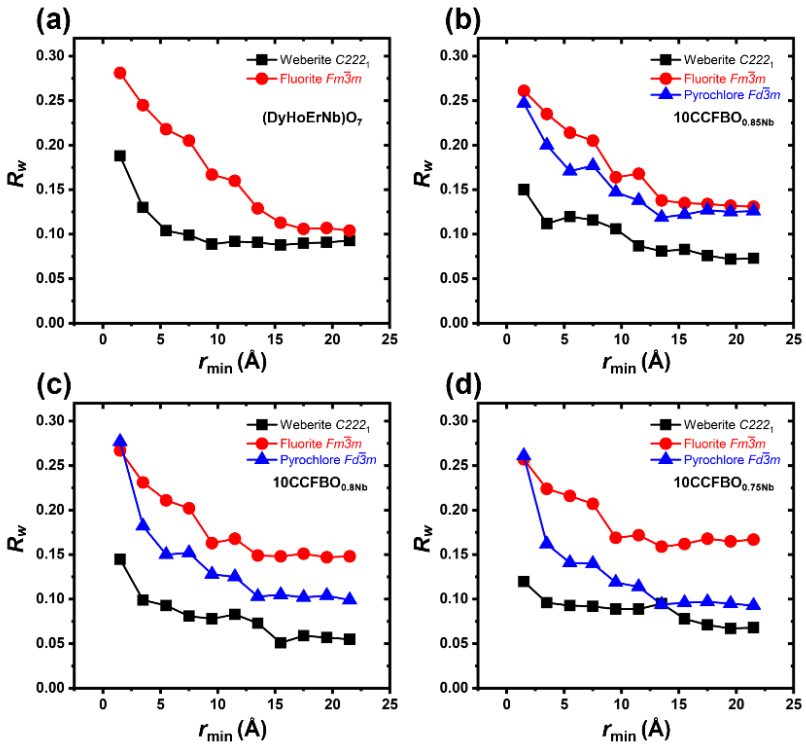

Figure 3. 16 Goodness-of-fit parameter (R_w) of four 10CCFBO$_{x}$Nb
(a) (DyHoErNb)O_7 (x = 1), **(b)** 10CCFBO$_{0.85}$Nb, **(c)** 10CCFBO$_{0.8}$Nb, and **(d)** 10CCFBO$_{0.75}$Nb *vs.* different r-values based on "boxcar" refinements of the neutron PDFs using three structural models ($Fd\bar{3}m$, $Fm\bar{3}m$ and $C222_1$). The r_{min} represents the minimum r-value of each 10 Å fit window (*e.g.*, 1.5-11.5 Å). For (DyHoErNb)O_7, pyrochlore model generates huge errors (R_w > 0.8) so it was excluded. In general, the $C222_1$ always generated better fitting compared other two structures (because of more fitting parameters), while the dependence on the r_{min} value provides more insights. As r_{min} increases, the fitting errors for the $Fd\bar{3}m$ (x = 0.75 and 0.8) and $Fm\bar{3}m$ (x = 0.85 and 1) tend to converge and approach to the $C222_1$ fitting.

As x increases in 10CCFBO$_{x}$Nb, the movement of O(48*f*) to vacant O(8*a*) can create a new local coordination environment. To accommodate the charge balance induced by this oxygen anion migration, some of the cations should adopt a change in the coordinated configuration, *e.g.* Zr adopts a 7-, instead of 6-, coordinated configuration, which can lead to the local weberite-type structure.[191–194] In the weberite-type order in the $C222_1$ ($A_1A_2BO_7$) structure, A_1 is 8-, A_2 is 7- and B is 6-fold coordinated. In niobate systems, Nb tends to occupy the 6-coordinated B site in local ordering. Ti also prefers the B site due to its smallest ionic radii. Other cations in 10CCFBO$_{x}$Nb likely distribute in the A_1 and A_2 sites evenly. Compared to pyrochlore and defect fluorite structures, weberite-type ordering has more flexibility to tune the atomic positions for both cations and oxygen anions, which enables more flexibility of the local coordination

environment change due to oxygen anion migration near the long-range ODT. In other words, the interplay of the short-range weberite-type ordering with long-range ODT is important.

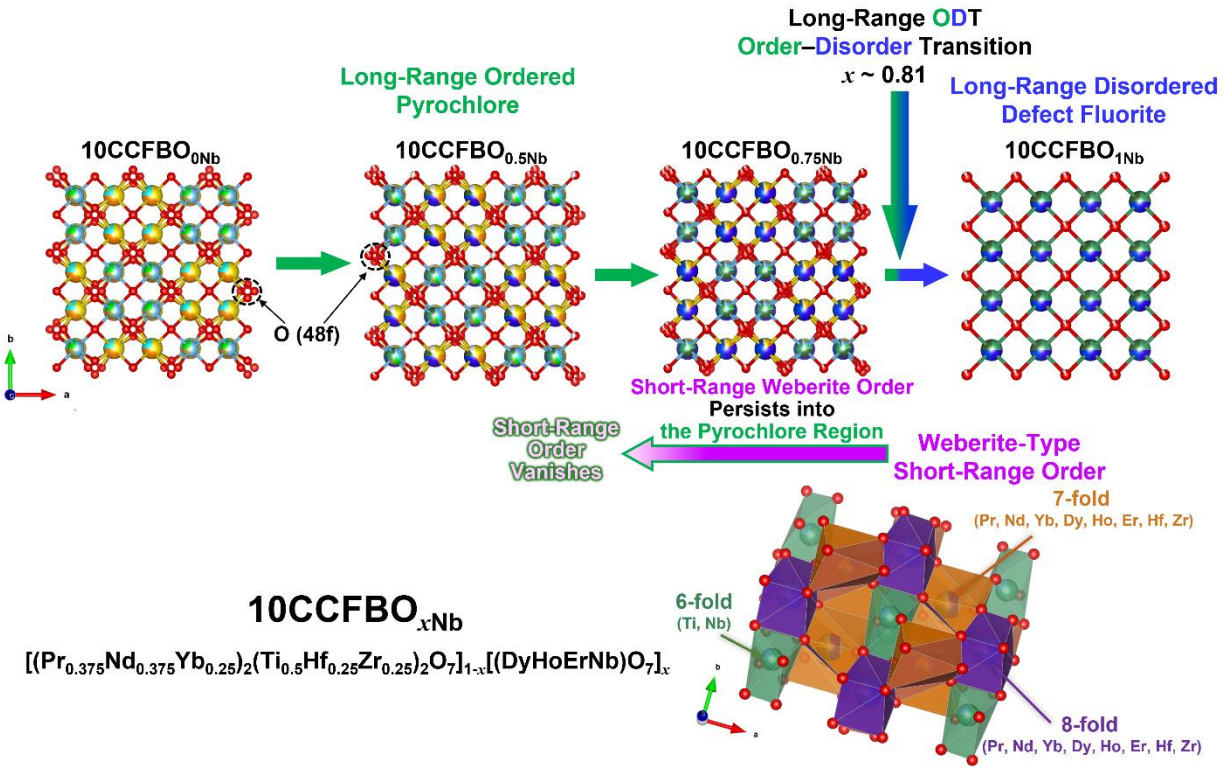

Figure 3. 17 Schematic of phase transformation in 10CCFBO$_{x\text{Nb}}$
Illustration of the transitions and competition of the long-range and short-range ordering *vs.* disordering in the 10CCFBO$_{x\text{Nb}}$ series. The crystal structures are plotted based on the refinements of the neutron diffraction patterns. The red spheres stand for oxygen anions and the white portion in red sphere shows the fractions of oxygen vacancies for the long-range structure.

The competition of long-range ODT and short-range ordering is schematically illustrated in Figure 3.17, based on the Rietveld refinements of the neutron diffraction patterns and small-box modelling of PDFs. In the 10CCFBO$_{x\text{Nb}}$ series, the ordering *vs.* disordering may be decoupled in two different length scales. For long-range ordering (x from 0 and 0.5 to 0.75), the migration of O(48*f*) gradually alters the pyrochlore structure (Figure 3.4d) and finally triggers a long-range ODT at around x = 0.81 to form disordered defect fluorite for the long-range order. As x increases from 0.5 to 0.75, where the long-range order is still ordered pyrochlore, weberite-type short-range order forms with Ti/Nb occupying the 6-coordinated site and all other

cations evenly distributed among 7- and 8-coordinated sites. The weberite-type short-range ordering persists into the long-range defect fluorite structure after the ODT, but gradually vanishes at smaller *x* values.

Here, we acknowledge the possible anti-site mixing of cations on the A *vs.* B sites, which is inevitable due to an entropy effect, and it can be pronouncing near the ODT. In our pyrochlore structure model for the Rietveld refinements, the cation position is fixed, which is a simplification since anti-site disordering can also occur during the ODT. However, it is infeasible to capture this scenario with 10 different cations (including similar rare earth elements) the Rietveld refinements.

3.3.5 Thermal Conductivity

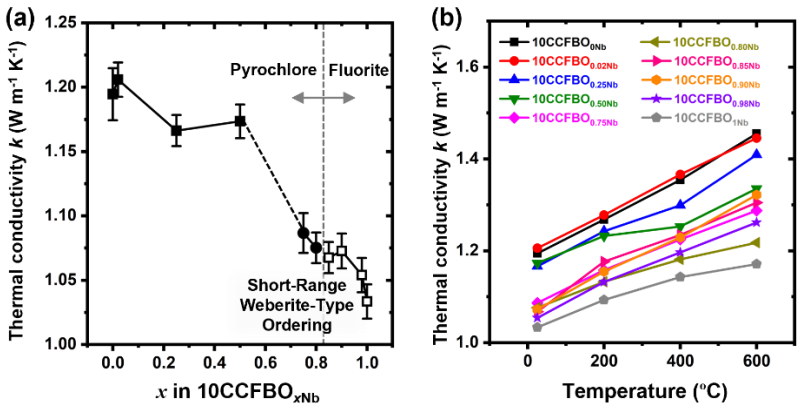

Figure 3. 18 Thermal conductivity measurements of $10CCFBO_{xNb}$
(a) Room temperature thermal conductivity *vs.* *x* in the $10CCFBO_{xNb}$ series of specimens. The solid squares stand for the long-range pyrochlore phases without short-range weberite-type ordering and solid circles represent the compositions with long-range pyrochlore phases with short-range weberite-type ordering. The hollow squares stand for long-range defect fluorite phases with short-range weberite-type ordering. The error bars are calculated based on the standard deviations of five individual measurements. **(b)** Temperature-dependent thermal conductivity curves for all $10CCFBO_{xNb}$ specimens.

Figure 3.18a shows the room temperature thermal conductivity of $10CCFBO_{xNb}$. In general, the thermal conductivity shows a decreasing trend with increasing *x*. Around the long-range ODT (for *x* between 0.8 and 0.85), the change of thermal conductivity was (surprisingly) small (comparable to the error bars). However, the short-range weberite-type ordering was present in $10CCFBO_{0.75Nb}$ and $10CCFBO_{0.8Nb}$, as shown by diffuse scattering and the following PDFs data analysis showed the phase transformation (Figure 3.4 and 3.10). No obvious diffuse scattering beneath $(331)_p$ diffraction peak of $10CCFBO_{0.5Nb}$ was observed (Figure 3.11), which suggests that the short-range transformation took place in between $10CCFBO_{0.5Nb}$ and

$10CCFBO_{0.75Nb}$. Interestingly, a larger drop in the thermal conductivity takes place in between $10CCFBO_{0.5Nb}$ and $10CCFBO_{0.75Nb}$ from 1.17 W $m^{-1}K^{-1}$ to 1.08 W $m^{-1}K^{-1}$ (in contrast to a smaller 1.05 W $m^{-1}K^{-1}$ to 1.07 W $m^{-1}K^{-1}$ change in between $10CCFBO_{0.8Nb}$ and $10CCFBO_{0.85Nb}$ for the long-range ODT). Thus, we hypothesize that the formation of weberite-type local structure (short-range ordering) can more appreciably alter thermal conductivity in $10CCFBO_{xNb}$ (in comparison with the long-range pyrochlore-to-fluorite ODT). It was proposed that the thermal conductivity can be significantly affected by the formation of dispersed nanodomains.[195] Prior studies also found that the weberite-type short-range ordering can lower the thermal conductivity in high-entropy rare earth niobates and tantalates.[158]

The temperature dependent thermal conductivity of $10CCFBO_{xNb}$ shows an amorphous-like trend (Figure 3.18b), where the thermal conductivity primarily increases with temperature due to increasing heat capacity.

3.4 Conclusion

In summary, we have investigated the long-range *vs.* short-range ordering and disordering, as well as the interplays between them, in a 10-component compositionally complex oxide system at different length scales by combining neutron diffraction and neutron total scattering. The synthesized compositions all exhibit nominally single high-entropy phases with either defect fluorite or pyrochlore in their long-range order. Rietveld refinements of long-range atomic configurations based on neutron diffraction shows a continuous oxygen anion migration from fully occupied 48*f* to vacant 8*a* sites with increasing x in $10CCFBO_{xNb}$, following a final jump during the long-range ODT at $x = 0.81 \pm 0.01$, while the 8*a* oxygen occupancy increases almost linearly without an apparent discontinuous jump at the ODT.

As a notable and interesting discovery, the long-range ODT takes place in the 10-component ultrahigh-entropy $10CCFBO_{xNb}$ without a detectable dual- or multi-phase region, in contrast to the simpler 3- and 4-component oxides. The pyrochlore *vs.* fluorite phase stability of the 10-component ultrahigh-entropy $10CCFBO_{xNb}$ does not follow the criteria that are well established based on simpler 3- and 4-compomnent oxides.

The coexistence of $(331)_p$ and diffuse scattering in $10CCFBO_{0.75Nb}$ and $10CCFBO_{0.8Nb}$ show the coexistence and competition of long-range pyrochlore order and short-range weberite-type order in these specimens. Four Nb-rich $10CCFBO_{xNb}$ (x = 0.75, 0.8, 0.85 and 1) near the ODT maintain similar local polyhedral environments when r < 10 Å, which can only be well fitted with the weberite-type structure $C222_1$ with the small-box modeling. The further "boxcar" refinements indicate that pyrochlore and defect fluorite can describe the structure well, if and only if the first and second nearest neighbor environment (r < 5 Å) is excluded. The combination of these analyses suggests the existence of short-range weberite-type order that overlaps and interplays with the long-range ODT in both ordered pyrochlore and disordered fluorite regions.

The room temperature thermal conductivity only has a negligible change during long-range ODT, but an appreciable drop when the short-range weberite-type ordering appears. This suggests that nanodomain structural distortion (short-range ordering) can reduce thermal conductivity more appreciably than the long-range ODT. In a broader context, elucidating and controlling the short- and long-range ordering *vs.* disordering may open a new window to tailor the structure, stability, and properties of HECs and CCCs with substantial compositional disorder (high configurational entropy).

Acknowledgement

Chapter 3, in full, is a reprint of the material as it appears in Advanced Powder Materials 2023. D. Zhang, Y. Chen, H. Vega, T. Feng, D. Yu, M. Everett, J. Neuefeind, K. An, R. Chen and J. Luo. The dissertation author was the primary investigator and author of this paper.

CHAPTER 4. Discovery of a reversible redox-induced order-disorder transition in a 10-component compositionally complex ceramic

4.1 Introduction

Disorder and order in fluorite-based oxides can influence a range of physical properties. For example, disorder can increase the ionic conductivities of yttria-stabilized zirconia (YSZ) and $Y_2(Zr_yTi_{1-y})_2O_{7,}$[149,186] enhance the catalytic activity and stability of Li-O_2 batteries,[196] and tailor the radiation resistance.[140,197] Long- or short-range pyrochlore and weberite orders can also exist in fluorite-based oxides.[198] The $A_2B_2O_7$ pyrochlore structure can be viewed as a $2 \times 2 \times 2$ superstructure of a base fluorite structure with ordered cations and oxygen vacancies and structural distortion.[199] Prior studies showed that the pyrochlore can transit to a defect fluorite structure, caused by composition[153,178,187,192,193,200–202] or temperature[144] induced disorder. In this work, we have further discovered a reversible redox-induced transition between the ordered pyrochlore and disordered fluorite structures.

In 2018, Gild *et al.* reported several single-phase YSZ-like high-entropy fluorite oxides (*e.g.*, $(Zr_{1/5}Hf_{1/5}Ce_{1/5}Y_{1/5}Yb_{1/5})O_{2-\delta}$ and $(Zr_{1/5}Hf_{1/5}Ce_{1/5}Y_{1/5}Gd_{1/5})O_{2-\delta}$) with high cation disorder and reduced thermal conductivities.[4] Since then, high-entropy fluorite oxides[159,203–205] (including rare-earth niobates RE_3NbO_7 in the defect fluorite structure[159,178,204,205]) and fluorite-based pyrochlore oxides[163,203,206–208] have been investigated for potential applications in thermal barrier coatings (TBCs). These high-entropy fluorite and pyrochlore oxides[163,175,203–205,207,208] belong to a broader class of high-entropy ceramics (HECs) that have attracted increasing research interests [175], which also include high-entropy rocksalt[209] and pervoskite[3] oxides, borides (of $MB_{2,}$[7] MB,[166] $M_3B_{4,}$[168] MB_4,[167] and MB_6[169,210] stoichiometries), silicides (of MSi_2 and M_5Si_5 stoichiometries), and carbides[2,8,170]. To date, most HEC studies are focused on equimolar compositions consisting of typically five (and sometimes four or six) metal cations.

In 2020, it was further proposed to broaden HECs to compositionally complex ceramics (CCCs) to include non-equimolar compositions that can outperform their equimolar counterparts.[10] Moreover, compositionally complex fluorite-based oxides (CCFBOs) can also possess points defects (oxygen

vacancies and aliovalent cations) and short- and long-range orders, which provide additional dimensions to tailor their thermomechanical properties.[161,175] Notably, a recent study reported a series of 11-cation single-phase CCFBOs with a composition-induced order-disorder (pyrochlore-fluorite) transition.[178] In a broad perspective, order and disorder can affect (or even control) many thermal and mechanical properties. However, it is not yet demonstrated that an order-disorder transition (ODT) can take place in a CCFBO (or any CCC and HEC in general) of a fixed composition.

In this study, we design a 10-cation oxide $(Nd_{0.15}Pr_{0.15}Dy_{0.8}Ho_{0.8}Er_{0.8}Ti_{0.2}Yb_{0.1}Hf_{0.1}Zr_{0.1}Nb_{0.8})O_{7-\delta}$. This composition is obtained by mixing 20% of a compositionally complex pyrochlore oxide $[(Nd_{0.375}Pr_{0.375}Yb_{0.25})_2(Ti_{0.5}Hf_{0.25}Zr_{0.25})_2O_7]$ with 80% of a high-entropy (fluorite-structured) rare-earth niobate $[(DyHoErNb)O_7]$. The mixture forms a single-phase pyrochlore structure when it is synthesized in air, with the nominal formula: $(Pr_{0.075}Nd_{0.075}Dy_{0.4}Ho_{0.4}Er_{0.05})_2(Ti_{0.1}Zr_{0.05}Hf_{0.05}Nb_{0.4}Er_{0.35}Yb_{0.05})_2O_7$ (with smaller cations on the B sites, albeit anti-site defects; see Supplementary Discussion). We denote this 10-cation CCFBO as "$10CCFBO_{0.8Nb}$" for brevity, where the subscript denotes the Nb (or niobate) content. The composition of this $10CCFBO_{0.8Nb}$ is selected so that it is a barely ordered pyrochlore phase (as it would become a disordered defect fluorite structure in air if we further increased the Nb or fluorite-structured niobate content). This composition design enables us to explore a disordering transition induced by oxygen vacancy generation under a reduced environment, which has not been reported previously, to explore a new route to tailor the order/disorder and properties of CCFBOs (or CCCs in general).

4.2 Experimental Section

4.2.1 Material Synthesis and Phase Characterization

All powders were purchased (from US Research Nanomaterials Inc., Houston, TX), ball milled, and uniaxially pressed into pellets, which were subsequently sintered at 1600 °C for 24 hours in air (following a standard recipe described in a prior report [178]). Specimen densities were measured by the Archimedes method to be ~98% of the theoretical density. We use "pristine" $10CCFBO_{0.8Nb}$ to refer to (oxidized) as-sintered samples. The pristine $10CCFBO_{0.8Nb}$ was annealed at 1600 °C for 2 hours in vacuum (10^{-3} mbar)

in a graphite furnace (RED DEVIL, RD WEBB, Cambridge, MA) to reduce it to induce an ODT. Subsequently, we re-annealed a reduced $10CCFBO_{0.8Nb}$ in air at 1600 °C for 12 hours to re-oxidize it to check whether the ODT is reversible. Specimens were characterized by using X-ray diffraction (Miniflex II XRD, Rigaku), a field emission scanning electron microscope (FE SEM, FEI Apero) in conjunction with energy dispersive X-ray spectroscopy (EDS), and an aberration-corrected scanning transmission electron microscope (STEM, JEOL 300CF) in conjunction with EDS and electron energy loss spectroscopy (EELS).

4.2.2 *In-situ* Neutron Diffraction Experiment

In-situ neutron diffraction was carried out at the Vulcan Engineering station of the Spallation Neutron Source (SNS) at the Oak Ridge National Laboratory (ORNL). Sintered pellets with ~10 mm diameters and ~2.5 mm thicknesses were used for neutron experiments. The synthesis conditions are the same as our other experiments. Due to the considerable neutron absorption from rare-earth elements in our materials, six pellets were stacked to reach a total of 15 mm in height to improve the data quality in *in-situ* heating neutron diffraction. The incident slits sizes were 5 mm × 12 mm. The 5 mm collimators excluded the signals of the furnace and crucible. Two rocking curves were measured and fitted along two horizontal orthogonal directions to determine the location of the neutron gauge volume ($5 \times 5 \times 12$ mm^3) in the bulk pellets that maximized the neutron counts in the detector Bank 2 at $2\theta = 90°$. The 30 Hz chopper setting with wavelength center at 2.5 Å and the high-intensity mode were used. At the beginning of the experiment, the samples were placed in a Nb crucible and heated up to 850 °C in 10^{-5} mbar high vacuum. Subsequently, the samples were held at 850 °C for 30 min and heated up again to 1000 °C, 1100 °C, 1200 °C, 1400 °C, 1450 °C, 1500 °C, and 1600 °C in a sequence. At each temperature, we kept the specimen isothermally for 30 minutes to collect high-quality neutron diffraction patterns.

4.2.3 Rietveld Refinements of Neutron Diffraction Patterns

For the $A_2B_2O_7$ pyrochlore ($Fd\bar{3}m$) structure, we need to maintain a site balance between A and B sites. The ratio of action radii (r_A/r_B) is a main factor determining pyrochlore *vs.* fluorite stability, where a pyrochlore structure is stable for $r_A/r_B > \sim 1.46$). Thus, larger ions should stay at the A sites and the smaller

ions are at the B sites. Following this principle, here we assume a formula $(Pr_{0.075}Nd_{0.075}Dy_{0.4}Ho_{0.4}Er_{0.05})_2(Ti_{0.1}Zr_{0.05}Hf_{0.05}Nb_{0.4}Er_{0.35}Yb_{0.05})_2O_{7-\delta}$ based on the ionic radii. In other words, the smallest Yb^{3+} cations all occupy the B sites, with the rest of the B sites are filled by the second smallest Er^{3+} actions; since we have more Er^{3+} than that can be accommodated at the B sites, the rest (a small fraction of) Er^{3+} cations go to the A sites. To verify this assumed formula based on the ion radii, we also tested some other chemical formulas; *e.g.*, placing large cations like Pr, Nd and Dy at the B sites led to substantially large fitting errors in the Rietveld refinements. The only exception is that if we put all Er^{3+} cations at the B sites, the alternative formula $(Pr_{0.075}Nd_{0.075}Dy_{0.4}Ho_{0.4}Yb_{0.05})_2(Ti_{0.1}Zr_{0.05}Hf_{0.05}Nb_{0.4}Er_{0.4})_2O_{7-\delta}$ produced similar fitting errors with the experimental neutron diffractions. Thus, we conducted the full Rietveld refinements for both formulae, which led to essentially the same conclusions on the oxygen ion deficiency and displacement. Thus, we adopted the most reasonable formula based on cation radii. Here, we acknowledge that there must be some cation mixing at the A *vs.* B sites (anti-site defects) at finite temperatures, which cannot be determined by Rietveld refinements or other methods.

The scattering data from Vulcan Bank 2 were used for the Rietveld refinements with the GSAS software because of its higher intensity. The refined parameters included the histogram scale factor, lattice parameter, 36 coefficients of Chebyshev polynomial background, isotropic thermal vibration coefficient for A/B site metal cations and oxygen anions (u_A, u_B, u_{O1}(48f), u_{O2} (8b), u_{O3} (8a) for the pyrochlore structure or u_O only for the fluorite structure), two coefficients describing Gaussian broadening (Sigma 1 and 2), and the neutron absorption factor. It is known that for the pyrochlore-to-fluorite transition, the 48f oxygen will gradually migrate to the originally vacant site 8a before reaching the ideal 0.875 occupancy for all oxygen sites and the positional parameter *x* of 48f oxygen (*x*, will gradually move to 0.375, which denotes the ideal position the 48f oxygen for the defect fluorite structure. For the pyrochlore structure, we also refined the lattice position *x* of the 48f oxygen, which is the only changeable positional parameter in the pyrochlore structure, and the oxygen anion site occupation.

4.2.4 Thermal Conductivity Measurement

The thermal diffusivity was measured using a laser flash analyzer (LFA 467 *HT HyperFlash*, NETZSCH, Germany). All the measurements were conducted from room temperature (25 °C) up to 1000 °C in an Ar gas environment, with five individual measurements at each temperature point. Due to the radiative heat transfer through the sample at high temperature, a transparent model was used to extract the thermal diffusivity by including a direct radiative heat transfer term in the boundary condition while neglecting the internal photon emission and absorption. With the one-dimensional assumption, the governing heat transfer equation and corresponding boundary conditions are:

$$\frac{\partial T}{\partial t} = \alpha \frac{\partial^2 T}{\partial x^2} \tag{4.1}$$

$$-k \frac{\partial T}{\partial x}\Big|_{x=0} = h\left(T_0 - T_{s,1}\right) - \eta h\left(T_{s,1} - T_{s,2}\right) \tag{4.2}$$

$$-k \frac{\partial T}{\partial x}\Big|_{x=d} = h\left(T_{s,2} - T_0\right) - \eta h\left(T_{s,1} - T_{s,2}\right) \tag{4.3}$$

where η is a fitting parameter describing the transparency, and h is another fitting parameter describing the heat loss coefficient on the top and bottom surfaces of the sample, T_0 is the ambient temperature (from room temperature to 1000 °C), $T_{s,1}$ and $T_{s,2}$ are the bottom and top surface temperatures, respectively, and d is the thickness of the sample.

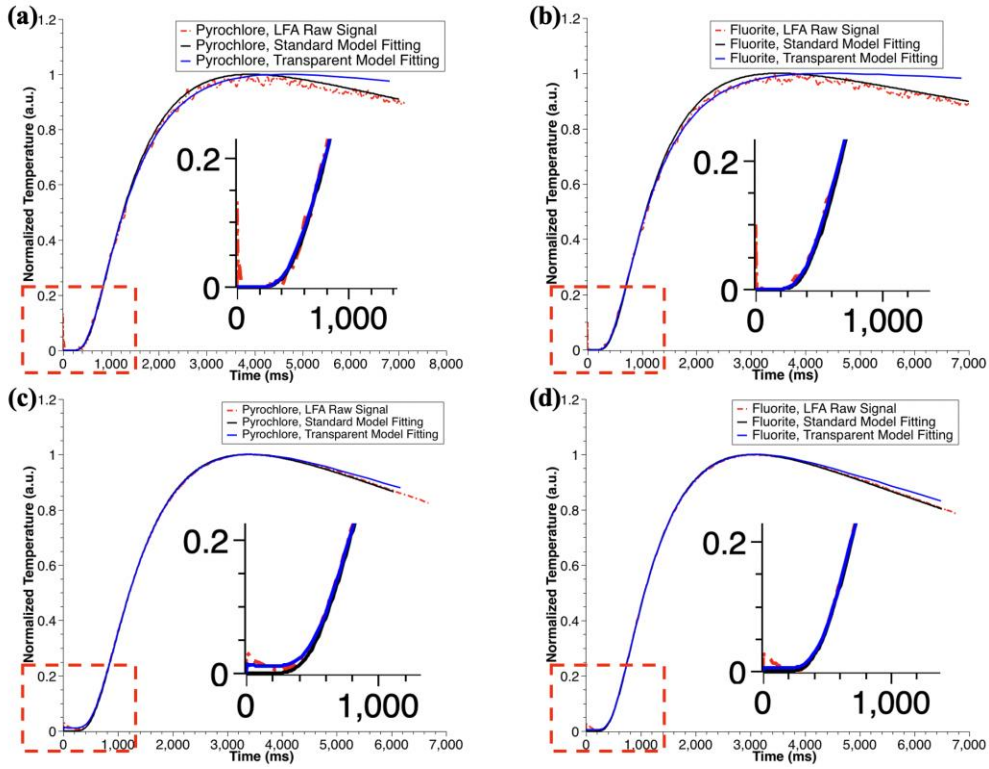

Figure 4. 1 Fitting of LFA raw data with different models
Fitting of LFA raw data (red dashed line) using the standard model (black solid line) and the transparent model (blue solid line) of (a) pyrochlore at 25 °C, (b) fluorite at 25 °C, (c) pyrochlore at 600 °C, (d) fluorite at 600 °C.

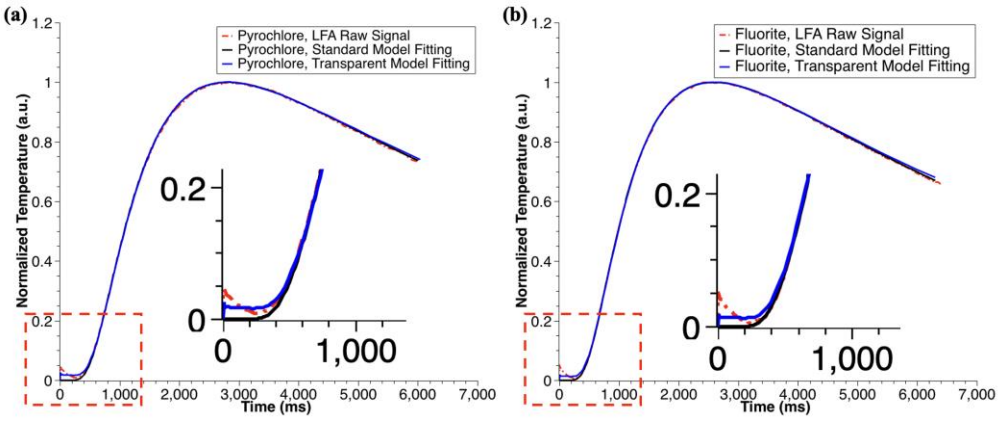

Figure 4. 2 Fitting of LFA raw data at 1000 °C
Fitting of LFA raw data at 1000 °C (red dashed line) using the standard model (black solid line) and the transparent model (blue solid line) of (a) pyrochlore and (b) fluorite.

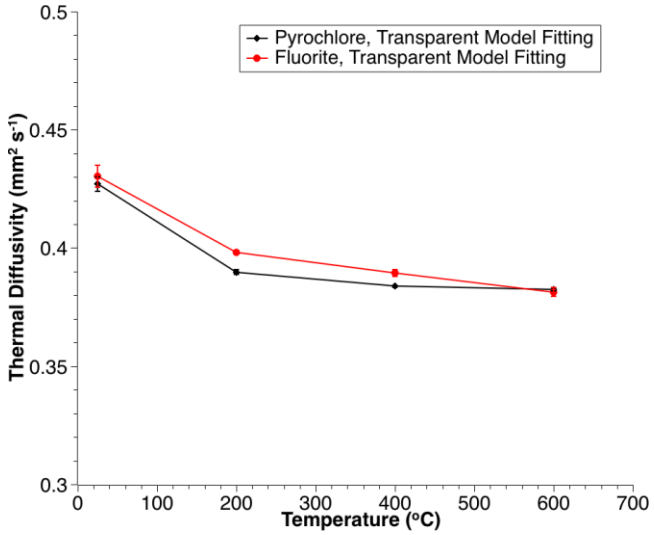

Figure 4. 3 Thermal diffusivity fitted by transparent model

After obtaining the raw data of backside temperature rise *vs.* time upon a pulsed heating on the front surface, the data were fitted with the transparent model with the three fitting parameters: α, η and h. The best fit with the experimental data, as determined by least square principle, gives the thermal diffusivity α. Figure 4.1 shows the fitting results of the two samples at 25 and 600 °C, pyrochlore (2.02 mm thick and 10 mm diameter) and fluorite (1.87 mm thick and 10 mm diameter) at different temperature, using the transparent model. The transparent model fits the data well up to 600 °C. Above 600 °C (*e.g.*, at 1000 °C), the fitting is not satisfactory, as shown in Figure 4.2. Therefore, we only report the thermal diffusivity (α) and thermal conductivity data within the temperature range of 25 to 600 °C. Figure 4.3 shows the fitting results of α of the two samples.

We note that the transparent model described here is necessary to obtain reasonable thermal diffusivity data. If the infrared photon transparency is neglected (*i.e.*, $\eta = 0$, or the "standard model" in the NETZSCH LFA software), the extracted thermal diffusivity would differ considerably. Figure 4.1 also shows the best fitting curves of the standard model for both samples at 25 and 600 °C. The standard model fits well at 25 °C due to the insignificant radiation contribution at this temperature but it does not capture the initial peak (at t = 0) of the temperature rise at all at 600 °C. Therefore, the standard model is inadequate at 600 °C. At even higher temperature (*e.g.*, 1000 °C) and for thicker samples, infrared photons that are scattering and/or

absorbed within the samples are also important to thermal conductivity. In this case, the samples are not completely transparent to these photons, and hence the transparent model does not work either, which is the case for the two samples measured here.

4.3 Results and Discussion

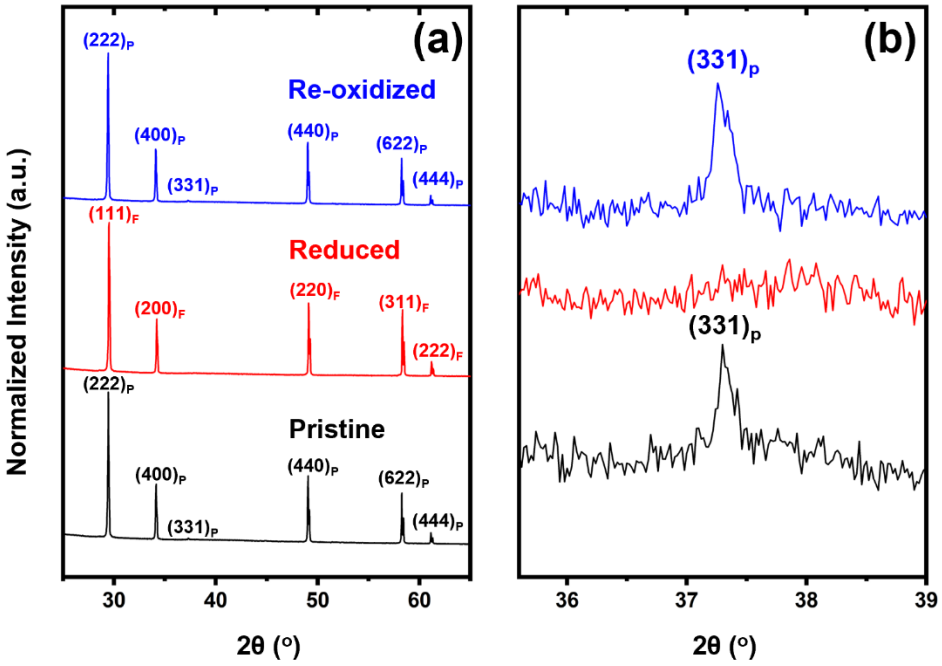

Figure 4. 4 XRD patterns of synthesized and annealed specimens
XRD patterns of (a) the pristine (synthesized in air), reduced, and re-oxidized specimens, and (b) an enlarged region showing the pyrochlore (331) superstructure peaks. The pristine sample was sintered in air at 1600 °C, which was then annealing at 1600 °C in vacuum (the reduced specimen) and subsequently in air at 1600 °C (the re-oxidized specimen). Here, the pyrochlore $(222)_P$ peak corresponds to the fluorite $(111)_F$ peak, where we use subscript "P" and "F" to denote the phase.

XRD patterns of the pristine, reduced, and re-oxidized specimens showed a reversible redox-induced ODT between ordered pyrochlore and disordered fluorite structures (Figure 4.4). All three XRD patterns suggested the formation of a single phase (without any detectable secondary phase, as shown in Figure 4.4) in each case. SEM EDS elemental mapping was used to confirm the compositional homogeneity in all three specimens (Figure 4.5). The pyrochlore and fluorite phases can be differentiated by the (331) superstructure peak, which were clearly evident for the pristine and re-oxidized specimens, but not detectable in the reduced specimen. Similar to the cases of weakly ordered $Gd_2Zr_2O_7$,[144,211] the pyrochlore superstructure peaks in the pristine and re-oxidized $10CCFBO_{0.8Nb}$ were weak because they were barely ordered. We also

noticed a reversible color change. As shown in the Figure 4.6, both the pristine and re-oxidized specimens were brown, but the reduced sample was black (presumably due to the formation of oxygen vacancies). The reduced sample was cross sectioned, grinded, and polished to confirm the color change (reduction) was uniform throughout the whole pellet. The atomic level structure and nanoscale compositional homogeneity were checked and verified by STEM HAADF imaging and EDS elemental mapping (Figure 4.7). In summary, the pristine specimen sintered in air at 1600 °C was ordered pyrochlore, which underwent an ODT to form a disordered defect fluorite phase after reduction at 1600 °C and transformed back to the ordered pyrochlore phase after re-oxidation at 1600 °C.

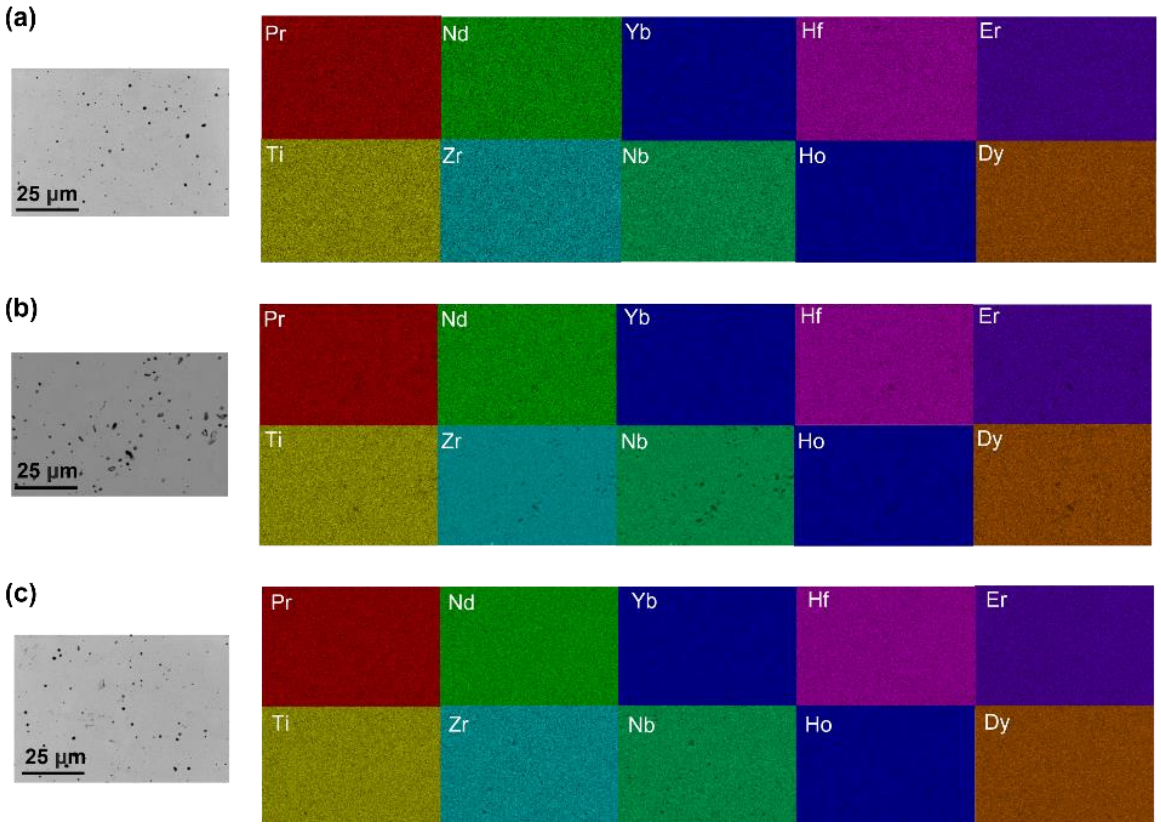

Figure 4. 5 SEM-EDS mapping
SEM EDS elemental maps of the pristine (a), reduced (b), and re-oxidized (c) specimens, showing that homogeneous single-phase solid solutions for all three cases. The SEM specimens were hot mounted in acrylic and final polished with 40 nm colloidal silica. The pristine sample was sintered in air at 1600 °C; the reduced and re-oxidized specimens were annealing at 1600 °C in vacuum and air, respectively.

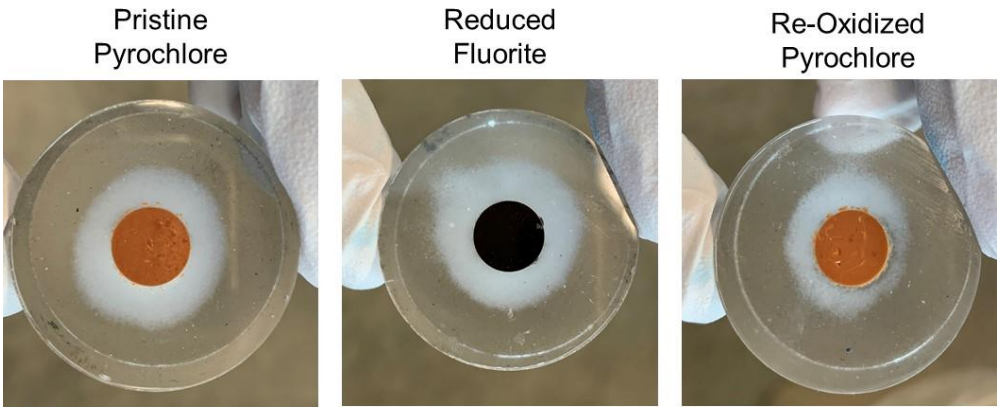

Figure 4. 6 Photos showing color changes

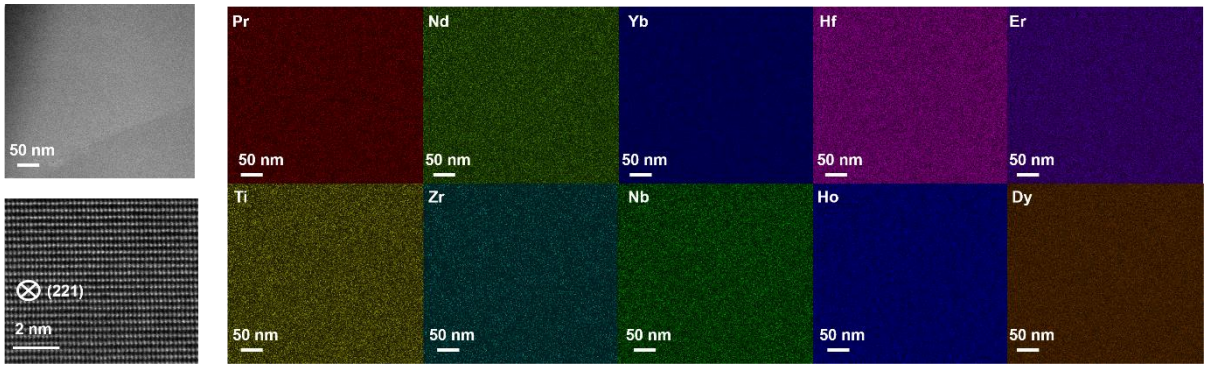

Figure 4. 7 STEM HAADF images and nanoscale EDS elemental mapping of the pristine $10CCFBO_{0.8Nb}$

Prior studies suggested that disordering of $A_2B_2O_7$ pyrochlore can be induced by altering ratio of ionic radii ($r_{A^{3+}}/r_{B^{4+}}$ < ~1.46 for ternary oxides [187]) or increasing temperature (*e.g.*, in weakly ordered $Gd_2Zr_2O_7$ [144]). In this study, we hypothesize a new redox-induced ODT mechanism where the observed reduction-induced disordering is attributed to the formation of the oxygen vacancies. Here, *ex-situ* benchtop XRD is insufficient to understand this new mechanism. Neutron diffraction can be used to probe structural changes with higher precisions [194,212–214], including those in high-entropy pyrochlores [180]. Thus, we conducted *in-situ* neutron diffraction experiments at the Vulcan station at the ORNL SNS. Specifically, we heated a pristine (oxidized) specimen in a vacuum furnace with a stepwise heating profile and collected neutron diffraction patterns at 850 °C, 1000 °C, 1100 °C, 1200 °C, 1400 °C, 1450 °C, 1500 °C, and 1600 °C in a sequence. During heating, the gas pressure was kept at 10^{-5} mbar to produce a reduced environment. Figure 4.8 shows the *in-situ* neutron diffraction patterns with an enlarged region showing the pyrochlore (331) and (511) superstructure peaks. With increasing temperature, the superstructure peaks gradually broadened;

they completely vanished at 1600 °C, indicating a reduction-induced disordering transition (ODT) to form a defect fluorite structure.

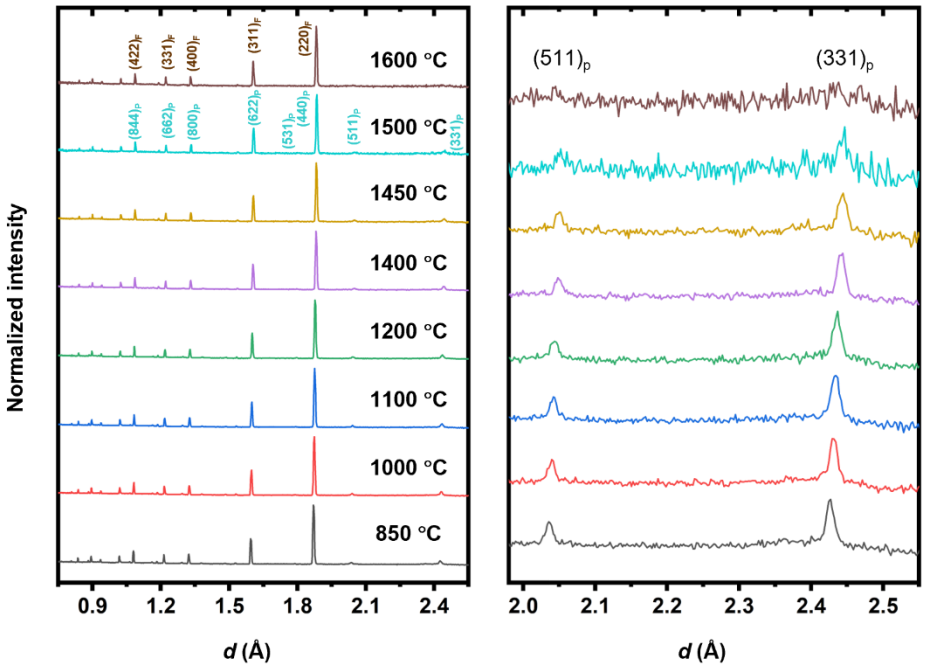

Figure 4. 8 *In-situ* heating (reduction) neutron diffraction patterns

Rietveld refinements were conducted to fit the neutron patterns. For the $A_2B_2O_7$ pyrochlore ($Fd\bar{3}m$) structure, we assume that Yb^{3+} and parts of Er^{3+} cations occupy the B site based on the ionic radii (by placing smaller cations on B sites, while maintaining the exact A:B stoichiometry) and the Rietveld refinement fittings (discussed in detail in Supplementary Discussion) so that the pyrochlore chemical formula is $(Pr_{0.075}Nd_{0.075}Dy_{0.4}Ho_{0.4}Er_{0.05})_2(Ti_{0.1}Zr_{0.05}Hf_{0.05}Nb_{0.4}Er_{0.35}Yb_{0.05})_2O_{7-\delta}$. For the disordered fluorite ($Fm\bar{3}m$) phase (for 1600 °C data only), all cations occupy at the same sublattice with the formula $(Nd_{0.15}Pr_{0.15}Dy_{0.8}Ho_{0.8}Er_{0.8}Ti_{0.2}Yb_{0.1}Hf_{0.1}Zr_{0.1}Nb_{0.8})O_{7-\delta}$. With these schemes, the refinement errors were lowered down to $R_w \approx 0.025$. One fitting example is given in Figure 4.9(a) and other refinement patterns are documented in Figure 4.10. In addition to the normal refinement parameters, two major parameters considered here were positional parameter *x* of the O1 (48*f*) site (at the position *x*, 1/8, 1/8) in the pyrochlore

unit cell and the oxygen deficiency δ (that is determined by the occupancies of the three oxygen sites for the pyrochlore structure, as documented and discussed in Table 4.1). As shown in prior reports [149,178], the positional parameter *x* of the O1 site will move to 0.375 in an ideal pyrochlore to fluorite ODT. The main fitted parameters of refinements are shown in Table 4.1.

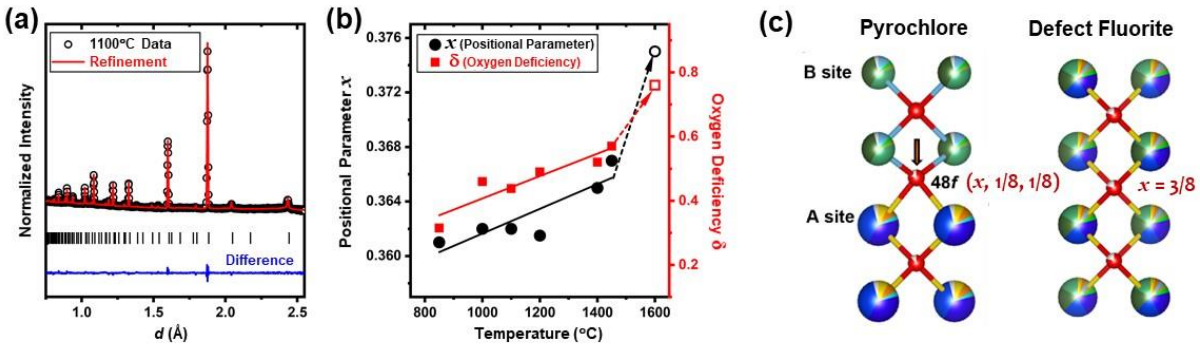

Figure 4. 9 Refinement results of the in-situ neutron diffraction patterns
(a) An example of the Rietveld refinement of the neutron diffraction pattern (for the measurement at 1100 °C). The fitting error $R_w \approx 2.5\%$. Additional cases are shown in the Figure 4.10. (b) Evolution of positional parameter *x* and oxygen deficiency δ *vs.* temperature, obtained via Rietveld refinements. The solid symbols were the values refined with the pyrochlore structure and the hollow ones were refined assuming the fluorite structure. The solid lines represent the best fittings for the pyrochlore structures while the dashed lines suggest the transition with the ODT. (c) Comparison of (the relevant sections of) pyrochlore and defect fluorite structures. In an ODT, the 48*f* oxygen, which is located at the position (*x*, 1/8, 1/8) in the ordered pyrochlore structure, moves gradually along the direction label by the arrow ($x \rightarrow 3/8$) to the position (3/8, 1/8, 1/8) in the defect fluorite structure. See full information of the $A_2B_2O_7$ pyrochlore structure and the positions of different atoms (A, B and O).

Table 4. 1 Parameters obtained via refinements of the neutron diffraction patterns.

The refinements were conducted based on the pyrochlore structure for measurements at 850-1450 °C. The structure became disordered (defect) fluorite at 1600 °C and the refinement was conducted based on the fluorite structure accordingly. The average occupancy of the oxygen sites is (O1 × 6 + O2 + O3)/8, where O1, O2, and O3 are the occupancies of the 48f, 8b, and 8a sites. The oxygen deficiency (the δ in $A_2B_2O_{7-\delta}$) is defined as: δ = 7 – (O1 × 6 + O2 + O3). It is interesting to note that the Rietveld refinements found virtually no oxygen vacancy ordering in this CCFBO$_{0.8Nb}$ ($Pr_{0.075}Nd_{0.075}Dy_{0.4}Ho_{0.4}Er_{0.05})_2(Ti_{0.1}Zr_{0.05}Hf_{0.05}Nb_{0.4}Er_{0.35}Yb_{0.05})_2O_7$, while there is strong oxygen vacancy ordering (i.e., O3 → 0) in the conventional pyrochlore compositions, including our pyrochlore endmember [$(Nd_{0.375}Pr_{0.375}Yb_{0.25})_2(Ti_{0.5}Hf_{0.25}Zr_{0.25})_2O_7$] (i.e., CCFBO$_{0Nb}$). In other words, CCFBO$_{0.8Nb}$ is a non-conventional pyrochlore composition with the addition of 80% $(DyHoErNb)O_7$ rare-earth niobate to the conventional pyrochlore CCFBO$_{0.8Nb}$, while it still maintains a long-range pyrochlore order in the oxidized environment (but with little or no oxygen vacancy ordering, as suggested by Rietveld refinements of neutron diffraction pattern).

Temperature (°C)	Lattice Parameter (Å)	48f (O1) Occupancy	8b (O2) Occupancy	8a (O3) Occupancy	Average O Site Occupancy	δ	Positional Parameter *x*	Fitting Error R_w
850	10.5755	0.800	0.885	0.993	0.835	0.322	0.361	0.028
1000	10.5921	0.790	0.860	0.939	0.817	0.461	0.362	0.028
1100	10.6033	0.793	0.854	0.950	0.820	0.438	0.362	0.025
1200	10.6149	0.775	0.852	0.982	0.811	0.510	0.3615	0.026
1400	10.6403	0.780	0.850	0.950	0.810	0.520	0.365	0.024
1450	10.6466	0.780	0.850	0.904	0.804	0.566	0.367	0.025

Temperature (°C)	Lattice Parameter (Å)	Oxygen Occupancy	Fitting Error R_w
1600 (Fluorite)	5.3332	0.780	0.03

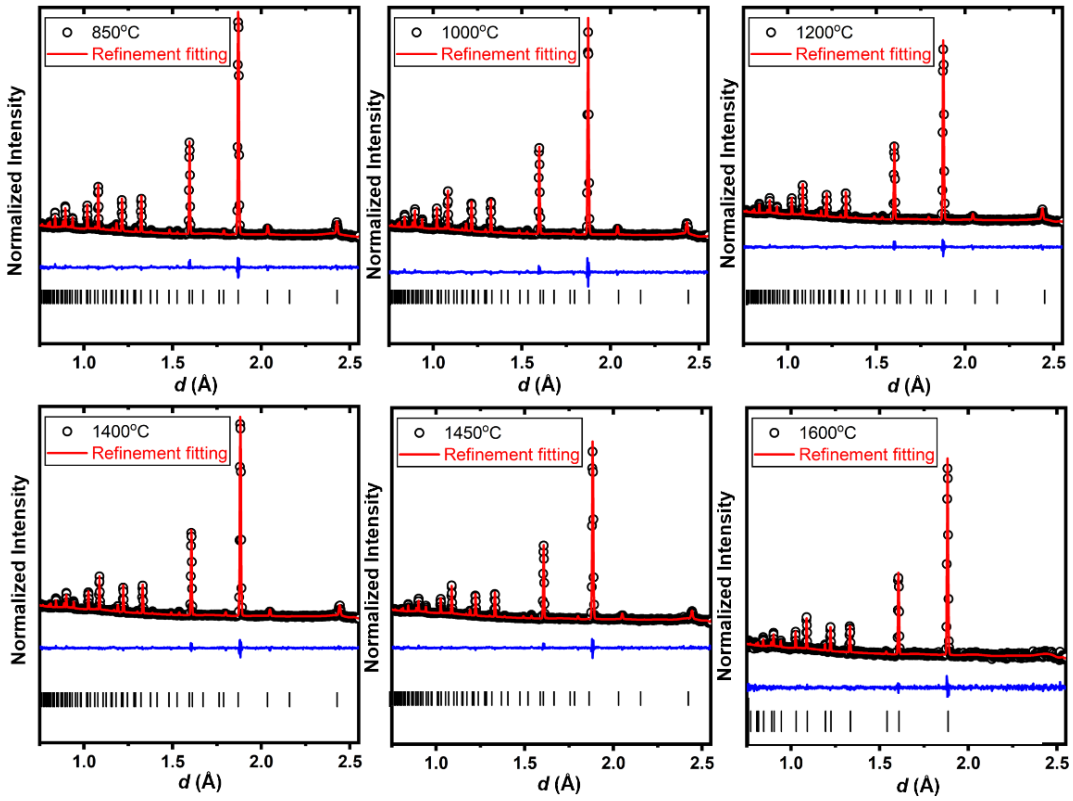

Figure 4. 10 Rietveld refinements of neutron diffraction patterns collected at different temperatures.

Figure 4.9b plots the fitted positional parameter *x* and oxygen deficiency δ *vs*. temperature. With increasing temperature, both *x* and δ increase. These trends are consistent with prior investigations of the compositionally induced ODT in in $Y_2(Ti_yZr_{1-y})_2O_7$ with increasing *y*.[149,186] Here, in addition to the displacement of the O1 site (changing of *x*), there are increases in oxygen deficiency. Our *in-situ* neutron experiments suggest that the positional parameter *x* of the O1 site approaches ~0.367 and oxygen deficiency δ reaches a significant value of ~0.57, just before the ODT. Here, the average occupancy of the oxygen sites (~0.80; see Table 4.1) is significantly below the nominal value of 0.875 in the defect fluorite structure, creating a large driving force for disordering. A schematic of oxygen migration in an ODT was shown in Figure 4.9c, where the 48*f* oxygen located at the position (*x*, 1/8, 1/8) in the ordered pyrochlore structure moves gradually to the position (3/8, 1/8, 1/8) in the defect fluorite structure.

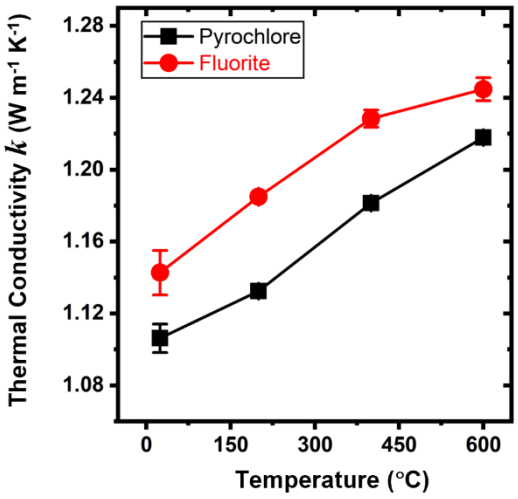

Figure 4. 11 Temperature-dependent thermal conductivities of pyrochlore vs. fluorite specimens.

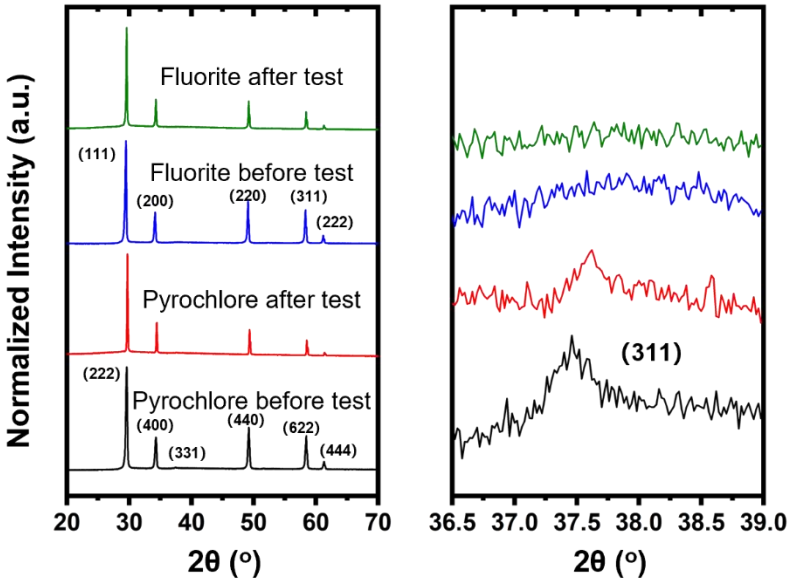

Figure 4. 12 XRD patterns before and after thermal conductivity measurements.

The thermal diffusivity was measured using a Laser Flash Analyzer (LFA 467 *HT HyperFlash*, NETZSCH, Germany). All measurements were conducted from room temperature (25 °C) up to 1000 °C in an Ar gas environment, with five individual measurements at each temperature point. Due to the direct radiative heat transfer through the sample at high temperature, a transparent model was used to fit the raw LFA data to extract the thermal diffusivity by including the radiative heat transfer term in the boundary

conditions while neglecting the internal photon emission and absorption. Figure 4.11 shows that both ordered pyrochlore and disordered fluorite 10CCFBO$_{0.8Nb}$ exhibit low thermal conductivities and amorphous-like temperature dependence (increasing thermal conductivity at higher temperature). The disordered fluorite 10CCFBO$_{0.8Nb}$ has a slightly higher room temperature thermal conductivity of ~1.14 W·m^{-1}·K^{-1} (*vs.* ~1.11 W·m^{-1}·K^{-1} for ordered pyrochlore 10CCFBO$_{0.8Nb}$) and similar slope with increasing temperature. At 600 °C, the disordered fluorite 10CCFBO$_{0.8Nb}$ also maintains a slightly higher thermal conductivity of ~1.24 W·m^{-1}·K^{-1}, compared to ~1.22 W·m^{-1}·K^{-1} for the ordered pyrochlore 10CCFBO$_{0.8Nb}$. XRD characterization after the thermal conductivity measurements in Ar up to 1000 °C showed that the measurements did not change the pyrochlore *vs.* fluorite structures of these two specimens (Figure 4.12). In other words, the order *vs.* disordered structure obtained via redox at 1600 °C can be quenched and preserved during thermal cycling from room temperature to 1000 °C, which offered a unique opportunity to investigate the effects of order *vs.* disorder on thermal conductivity on specimens of an identical composition.

4.4 Conclusion

In summary, we have discovered a reversible redox-induced pyrochlore-to-fluorite transition in a 10-cation CCFBO from the ordered pyrochlore to the disordered fluorite structure, while maintaining a single high-entropy solid solution phase before and after this ODT. *In-situ* neutron diffraction revealed that this ODT is induced by the generation of oxygen vacancies. An ODT can alter the physical properties, *e.g.*, thermal conductivity; specifically, the disordered fluorite 10CCFBO$_{0.8Nb}$ has a slightly higher thermal conductivity than the ordered pyrochlore 10CCFBO$_{0.8Nb}$ from room temperature to 600 °C.

Acknowledgement

Chapter 4, in full, is a reprint of the material as it appears in Scripta Materials 2022. D. Zhang, Y. Chen, T. Feng, D. Yu, K. An, R. Chen and J. Luo. The dissertation author was the primary investigator and author of this paper.

Dissertation Summary

In this dissertation, compositionally complex ceramics (CCCs) – as an extension of the emergent high-entropy ceramics (HECs) – were designed to achieve excellent STCH performance via utilizing non-equimolar compositional designs to attain an optimal balance of thermodynamic and kinetic properties. In addition, we achieved in-depth mechanistic understanding of redox behaviors (preferred redox sequence) and the thermodynamic and kinetic trade-off via combining measurements of intrinsic thermodynamic and kinetic properties, in situ characterization of the redox reaction, and the utilization of a new parallel Monte Carlo and density functional theory computation method.

Moreover, we discovered normal *vs.* abnormal aliovalent doping effects on oxygen non-stoichiometry in two series of medium-entropy compositionally complex perovskite oxides. The mechanism was investigated by analysis of the energy loss near edge structure (ELNES) and density functional theory (DFT) calculations. The unusual V-shape in oxygen non-stoichiometry *vs.* aliovalent doping is caused by the stable Ti^{4+} with a V-shape Mn/Fe valency evolution.

Neutron diffraction and total scattering was applied to investigate the long-range *vs.* short-range ordering and disordering, as well as the interplays between them, in a 10-component compositionally complex oxide system at different length scales. As a notable and interesting discovery, the long-range ODT takes place in the 10-component ultrahigh-entropy $10CCFBO_{xNb}$ without a detectable dual- or multi-phase region, in contrast to the simpler 3- and 4-component oxides. The pyrochlore *vs.* fluorite phase stability of the 10-component ultrahigh-entropy $10CCFBO_{xNb}$ does not follow the criteria that are well established based on simpler 3- and 4-compomnent oxides. Four Nb-rich $10CCFBO_{xNb}$ (x = 0.75, 0.8, 0.85 and 1) near the ODT maintain similar local polyhedral environments when r < 10 Å, which can only be well fitted with the weberite-type structure $C222_1$ with the small-box modeling. The combination of these analyses suggests the existence of short-range weberite-type order that overlaps and interplays with the long-range ODT in both ordered pyrochlore and disordered fluorite regions.

A reversible redox-induced pyrochlore-to-fluorite transition in a 10-cation CCFBO from the ordered pyrochlore to the disordered fluorite structure was discovered, while maintaining a single high-entropy solid solution phase before and after this ODT. *In-situ* neutron diffraction revealed that this ODT is induced by the generation of oxygen vacancies.

REFERENCES

1 C. M. Rost, E. Sachet, T. Borman, A. Moballegh, E. C. Dickey, D. Hou, J. L. Jones, S. Curtarolo and J. P. Maria, *Nat. Commun.*, 2015, **6**, 8485.

2 T. J. Harrington, J. Gild, P. Sarker, C. Toher, C. M. Rost, O. F. Dippo, C. McElfresh, K. Kaufmann, E. Marin, L. Borowski, P. E. Hopkins, J. Luo, S. Curtarolo, D. W. Brenner and K. S. Vecchio, *Acta Mater.*, 2019, **166**, 271–280.

3 S. Jiang, T. Hu, J. Gild, N. Zhou, J. Nie, M. Qin, T. Harrington, K. Vecchio and J. Luo, *Scr. Mater.*, 2018, **142**, 116–120.

4 J. Gild, M. Samiee, J. L. Braun, T. Harrington, H. Vega, P. E. Hopkins, K. Vecchio and J. Luo, *J. Eur. Ceram. Soc.*, 2018, **38**, 3578–3584.

5 K. Zhang, W. Li, J. Zeng, T. Deng, B. Luo, H. Zhang and X. Huang, *J. Alloys Compd.*, 2020, **817**, 153328.

6 Z. Zhao, H. Chen, H. Xiang, F. Z. Dai, X. Wang, W. Xu, K. Sun, Z. Peng and Y. Zhou, *J. Adv. Ceram.*, 2020, **9**, 303–311.

7 J. Gild, Y. Zhang, T. Harrington, S. Jiang, T. Hu, M. C. Quinn, W. M. Mellor, N. Zhou, K. Vecchio and J. Luo, *Sci. Rep.*, 2016, **6**, 37946.

8 X. Yan, L. Constantin, Y. Lu, J. F. Silvain, M. Nastasi and B. Cui, *J. Am. Ceram. Soc.*, 2018, **101**, 4486–4491.

9 J. Gild, J. Braun, K. Kaufmann, E. Marin, T. Harrington, P. Hopkins, K. Vecchio and J. Luo, *J. Mater.*, 2019, 337–343.

10 A. J. Wright, Q. Wang, C. Huang, A. Nieto, R. Chen and J. Luo, *J. Eur. Ceram. Soc.*, 2020, **40**, 2120–2129.

11 A. J. Wright and J. Luo, *J. Mater. Sci.*, 2020, **55**, 8812–9827.

12 J. H. Wee, *Renew. Sustain. Energy Rev.*, 2007, **11**, 1720–1738.

13 K. Jiao, J. Xuan, Q. Du, Z. Bao, B. Xie, B. Wang, Y. Zhao, L. Fan, H. Wang, Z. Hou, S. Huo, N. P. Brandon, Y. Yin and M. D. Guiver, *Nature*, 2021, **595**, 361–369.

14 D. Banham, T. Kishimoto, Y. Zhou, T. Sato, K. Bai, J. I. Ozaki, Y. Imashiro and S. Ye, *Sci. Adv.*, 2018, **4**, 7180.

15 C. Ampelli, S. Perathoner and G. Centi, *Philos. Trans. R. Soc. A*, 2015, **373**, 201401.

16 G. Centi, E. A. Quadrelli and S. Perathoner, *Energy Environ. Sci.*, 2013, **6**, 1711–1731.

17 J. E. Miller, A. H. McDaniel and M. D. Allendorf, *Adv. Energy Mater.*, 2014, **4**, 1300469.

18 R. Schäppi, D. Rutz, F. Dähler, A. Muroyama, P. Haueter, J. Lilliestam, A. Patt, P. Furler and A. Steinfeld, *Nature*, 2022, **601**, 63–68.

19 A. Steinfeld, *Sol. Energy*, 2005, **78**, 603–615.

20 T. Kodama and N. Gokon, *Chem. Rev.*, 2007, **107**, 4048–4077.

21 J. R. Scheffe and A. Steinfeld, *Mater. Today*, 2014, **17**, 341–348.

22 B. Bulfin, J. Vieten, C. Agrafiotis, M. Roeb and C. Sattler, *J. Mater. Chem. A*, 2017, **5**, 18951–18966.

23 W. C. Chueh and S. M. Haile, *ChemSusChem*, 2009, **2**, 735–739.

24 W. C. Chueh, C. Falter, M. Abbott, D. Scipio, P. Furler, S. M. Haile and A. Steinfeld, *Science*, 2010, **330**, 1797.

25 Christopher Muhich and Aldo Steinfeld, *J. Mater. Chem. A*, 2017, **5**, 15578–15590.

26 F. A. C. Oliveira, M. Alexandra Barreiros, Anita Haeussler, A. P. F. Caetano, A. I. Mouquinho, P. M. O. e Silva, R. M. Novais, R. C. Pullar and Stéphane Abanades, *Sustain. Energy Fuels*, 2020, **4**, 3077–3089.

27 I. Ermanoski, J. E. Miller and M. D. Allendorf, *Phys. Chem. Chem. Phys.*, 2014, **16**, 8418–8427.

28 A. A. Emery and C. Wolverton, *Sci. Data*, 2017, **4**, 170153.

29 A. A. Emery, J. E. Saal, S. Kirklin, V. I. Hegde and C. Wolverton, *Chem. Mater.*, 2016, **28**, 5621–5634.

30 X. Qian, J. He, E. Mastronardo, B. Baldassarri, W. Yuan, C. Wolverton and S. M. Haile, *Matter*, 2021, **4**, 688–708.

31 A. H. McDaniel, E. C. Miller, D. Arifin, A. Ambrosini, E. N. Coker, R. O'Hayre, W. C. Chueh and J. Tong, *Energy Environ. Sci.*, 2013, **6**, 2424–2428.

32 Z. Chen, Q. Jiang, F. Cheng, J. Tong, M. Yang, Z. Jiang and C. Li, *J. Mater. Chem. A*, 2019, **7**, 6099–6112.

33 L. Wang, M. Al-Mamun, P. Liu, Y. Wang, H. G. Yang and H. Zhao, *Chinese J. Catal.*, 2017, **38**, 1079–1086.

34 M. Kubicek, A. H. Bork and J. L. M. Rupp, *J. Mater. Chem. A*, 2017, 5, 11983.

35 R. D. Barcellos, M. D. Sanders, J. Tong, A. H. McDaniel and R. P. O'Hayre, *Energy Environ. Sci.*, 2018, **11**, 3256–3265.

36 J. E. Park, Z. J. L. Bare, R. J. Morelock, M. A. Rodriguez, A. Ambrosini, C. B. Musgrave, A. H. McDaniel and E. N. Coker, *Front. Energy Res.*, 2021, **9**, 750600.

37 M. Orfila, M. Linares, A. Pérez, I. Barras-García, R. Molina, J. Marugán, J. A. Botas and R. Sanz, *Int. J. Hydrogen Energy*, 2022, **47**, 41209–41222.

38 L. Wang, M. Al-Mamun, Y. L. Zhong, P. Liu, Y. Wang, H. G. Yang and H. Zhao, *Chempluschem*, 2018, **83**, 924–928.

39 A. Pérez, M. Orfila, M. Linares, R. Sanz, J. Marugán, R. Molina and J. A. Botas, *Catal. Today*, 2022, **390**–**391**, 22–33.

40 A. Demont, S. Abanades and E. Beche, *J. Phys. Chem. C*, 2014, **118**, 12682–12692.

41 A. Haeussler, A. Julbe and S. Abanades, *Mater. Chem. Phys.*, 2022, **276**, 125358.

42 L. Wang, M. Al-Mamun, P. Liu, Y. Wang, H. G. Yang and H. Zhao, *J. Mater. Sci.*, 2018, **53**, 6796–6806.

43 S. Dey, B. S. Naidu, A. Govindaraj and C. N. R. Rao, *Phys. Chem. Chem. Phys.*, 2015, **17**, 122–125.

44 R. J. Carrillo, C. M. Hill, K. J. Warren and J. R. Scheffe, *J. Phys. Chem. C*, 2020, **124**, 4448–4458.

45 J. A. Trindell, A. H. Mcdaniel, T. Ogitsu, A. Ambrosini and J. D. Sugar, *Chem. Mater.*, 2022, **34**, 7712–7720.

46 S. Zhai, J. Rojas, N. Ahlborg, K. Lim, M. F. Toney, H. Jin, W. C. Chueh and A. Majumdar, *Energy Environ. Sci.*, 2018, **11**, 2172–2178.

47 A. J. Wright, Q. Wang, S.-T. Ko, K. M. Chung, R. Chen and J. Luo, *Scr. Mater.*, 2020, 76–81.

48 X. Qian, J. He, E. Mastronardo, B. Baldassarri, C. Wolverton and S. M. Haile, *Chem. Mater.*, 2020, **32**, 9335–9346.

49 Y. Li, K. Gerdes, H. Diamond and X. Liu, *Solid State Ionics*, 2011, **204**–**205**, 104–110.

50 M. Takacs, J. R. Scheffe and A. Steinfeld, *Phys. Chem. Chem. Phys.*, 2015, **17**, 7813–7822.

51 J. R. Scheffe, D. Weibel and A. Steinfeld, *Energy and Fuels*, 2013, **27**, 4250–4257.

52 A. Sharan and S. Lany, *J. Chem. Phys.*, 2021, **154**, 234706.

53 D. Joubert, *Phys. Rev. B - Condens. Matter Mater. Phys.*, 1999, **59**, 1758–1775.

54 J. P. Perdew, K. Burke and M. Ernzerhof, *Phys. Rev. Lett.*, 1996, **77**, 3865–3868.

55 I. D. Brown and R. D. Shannon, *Acta Crystallogr. Sect. A*, 1973, **29**, 266–282.

56 I. D. Brown, *Chem. Rev.*, 2009, **109**, 6858–6919.

57 B. Y. R. D. Shannon, M. H, N. H. Baur, O. H. Gibbs, M. Eu and V. Cu, *Acta Crystallogr. Sect. A*, 1976, **A32**, 751–767.

58 X. Hou, K. Ohta, Y. Kimura, Y. Tamenori, K. Tsuruta, K. Amezawa and T. Nakamura, *Adv. Energy Mater.*, 2021, **11**, 2101005.

59 A. Y. Zuev, A. I. Vylkov, A. N. Petrov and D. S. Tsvetkov, *Solid State Ionics*, 2008, **179**, 1876–1879.

60 J. Vieten, B. Bulfin, F. Call, M. Lange, M. Schmücker, A. Francke, M. Roeb and C. Sattler, *J. Mater. Chem. A*, 2016, **4**, 13652–13659.

61 M. D. Sanders, A. M. Bergeson-Keller, E. N. Coker and R. P. O'Hayre, *Front. Energy Res.*, 2022, **10**, 856943.

62 E. J. Crumlin, E. Mutoro, W. T. Hong, M. D. Biegalski, H. M. Christen, Z. Liu, H. Bluhm and Y. Shao-Horn, *J. Phys. Chem. C*, 2013, **117**, 16087–16094.

63 M. Niania, R. Podor, T. Ben Britton, C. Li, S. J. Cooper, N. Svetkov, S. Skinner and J. Kilner, *J. Mater. Chem. A*, 2018, **6**, 14120–14135.

64 W. Jung and H. L. Tuller, *Energy Environ. Sci.*, 2012, **5**, 5370–5378.

65 L. Lukashuk, N. Yigit, R. Rameshan, E. Kolar, D. Teschner, M. Hävecker, A. Knop-Gericke, R. Schlögl, K. Föttinger and G. Rupprechter, *ACS Catal.*, 2018, **8**, 8630–8641.

66 K. Guse and H. Papp, *Fresenius. J. Anal. Chem.*, 1993, **346**, 84–91.

67 L. Lukashuk, K. Föttinger, E. Kolar, C. Rameshan, D. Teschner, M. Hävecker, A. Knop-Gericke, N. Yigit, H. Li, E. McDermott, M. Stöger-Pollach and G. Rupprechter, *J. Catal.*, 2016, **344**, 1–15.

68 J. R. Scheffe, A. H. McDaniel, M. D. Allendorf and A. W. Weimer, *Energy Environ. Sci.*, 2013, **6**, 963–973.

69 Z. Chen, Q. Jiang, J. Tong, M. Yang, Z. Jiang and C. Li, *Sol. Energy*, 2017, **144**, 643–659.

70 T. C. Davenport, M. Kemei, M. J. Ignatowich and S. M. Haile, *Int. J. Hydrogen Energy*, 2017, **42**, 16932–16945.

71 H. Qi, Y. L. Lee, T. Yang, W. Li, W. Li, L. Ma, S. Hu, Y. Duan, G. A. Hackett and X. Liu, *ACS Catal.*, 2020, **10**, 5567–5578.

72 Y. Cao, M. J. Gadre, A. T. Ngo, S. B. Adler and D. D. Morgan, *Nat. Commun.*, 2019, **10**, 1346.

73 B. Bulfin, M. Miranda and A. Steinfeld, *Front. Energy Res.*, 2021, **9**, 677980.

74 C. K. Yang, Y. Yamazaki, A. Aydin and S. M. Haile, *J. Mater. Chem. A*, 2014, **2**, 13612–13623.

75 J. Cong, T. Ma, Z. Chang, J. S. Akhatov, M. Fu and X. Li, *Inorg. Chem. Front.*, 2022, **9**, 5714.

76 A. H. Bork, M. Kubicek, M. Struzik and J. L. M. Rupp, *J. Mater. Chem. A*, 2015, **3**, 15546.

77 R. K. Patel, S. K. Ojha, S. Kumar, A. Saha, P. Mandal, J. W. Freeland and S. Middey, *Appl. Phys. Lett.*, 2020, **116**, 071601.

78 A. Sarkar, Q. Wang, A. Schiele, M. R. Chellali, S. S. Bhattacharya, D. Wang, T. Brezesinski, H. Hahn, L. Velasco and B. Breitung, *Adv. Mater.*, 2019, **31**, 1806236.

79 A. Sarkar, R. Djenadic, D. Wang, C. Hein, R. Kautenburger, O. Clemens and H. Hahn, *J. Eur. Ceram. Soc.*, 2018, **38**, 2318–2327.

80 Z. Li, B. Guan, F. Xia, J. Nie, W. Li, L. Ma, W. Li, L. Zhou, Y. Wang, H. Tian, J. Luo, Y. Chen, M. Frost, K. An and X. Liu, *ACS Appl. Mater. Interfaces*, 2022, **14**, 24363–24373.

81 Y. Ma, Y. Ma, Q. Wang, S. Schweidler, M. Botros, T. Fu, H. Hahn, T. Brezesinski and B. Breitung, *Energy Environ. Sci.*, 2021, **14**, 2883–2905.

82 Q. Wang, A. Sarkar, D. Wang, L. Velasco, R. Azmi, S. S. Bhattacharya, T. Bergfeldt, A. Düvel, P. Heitjans, T. Brezesinski, H. Hahn and B. Breitung, *Energy Environ. Sci.*, 2019, **12**, 2433–2442.

83 J. Wang, Z. Cao, X. Zhu and W. Yang, *J. Membr. Sci. Lett.*, 2022, **2**, 100026.

84 H. Mahon, D. O'Connor, D. Friedrich and B. Hughes, *Energy*, 2022, **239**, 122207.

85 S. Kuravi, J. Trahan, D. Y. Goswami, M. M. Rahman and E. K. Stefanakos, *Prog. Energy Combust. Sci.*, 2013, **39**, 285–319.

86 M. I. Khan, F. Asfand and S. G. Al-Ghamdi, *J. Energy Storage*, 2022, **55**, 105860.

87 U. Ash-Kurlander, O. Martin, L. D. Fontana, V. R. Patil, M. Bernegger, C. Mondelli, J. Pérez-Ramírez and A. Steinfeld, *Energy Technol.*, 2016, **4**, 565–572.

88 A. H. Mcdaniel, R. Bell, J. Martinek, Z. Ma and D. Ginley, *Sandia Rep. SAND2022-7670*.

89 W. Li, N. Jiang, B. Hu, X. Liu, F. Song, G. Han, T. J. Jordan, T. B. Hanson, T. L. Liu and Y. Sun, *Chem*, 2018, **4**, 637–649.

90 L. A. King, M. K. A. Hubert, C. Capuano, J. Manco, N. Danilovic, E. Valle, T. R. Hellstern, K. Ayers and T. F. Jaramillo, *Nat. Nanotechnol.*, 2019, **14**, 1071–1074.

91 A. Weiß, A. Siebel, M. Bernt, T.-H. Shen, V. Tileli and H. A. Gasteiger, *J. Electrochem. Soc.*, 2019, **166**, F487–F497.

92 T. E. Mallouk, *Nat. Chem.*, 2013, **5**, 362–363.

93 E. Mastronardo, X. Qian, J. M. Coronado and S. M. Haile, *J. Mater. Chem. A*, 2020, **8**, 8503–8517.

94 K. J. Warren, J. T. Tran and A. W. Weimer, *Energy Environ. Sci.*, 2022, **15**, 806–821.

95 X. Qian, S. M. Haile, T. C. Davenport and E. Mastronardo, *J. Am. Ceram. Soc.*, 2022, **105**, 4375–4386.

96 J. Mizusaki, Y. Mima, S. Shigeru, Y. And and K. Fuekir, *J. Solid State Chem.*, 1989, **80**, 102–111.

97 M. Takacs, M. Hoes, M. Caduff, T. Cooper, J. R. Scheffe and A. Steinfeld, *Acta Mater.*, 2016, **103**, 700–710.

98 Y. Hao, C. K. Yang and S. M. Haile, *Chem. Mater.*, 2014, **26**, 6073–6082.

99 J. E. Garnier, R. N. Blumenthal, R. J. Panlener and R. K. Sharma, *J. Phys. Chem. Solids*, 1976, **37**, 368–378.

100 M. Ezbiri, M. Takacs, D. Theiler, R. Michalsky and A. Steinfeld, *J. Mater. Chem. A*, 2017, **5**, 4172–4182.

101 M. J. Ignatowich, A. H. Bork, T. C. Davenport, J. L. M. Rupp, C. K. Yang, Y. Yamazaki and S. M. Haile, *MRS Commun.*, 2017, **7**, 873–878.

102 B. Meredig and C. Wolverton, *Phys. Rev. B*, 2009, **80**, 245119.

103 E. Bakken, T. Norby and S. Stølen, *J. Mater. Chem.*, 2002, **12**, 317–323.

104 C. Wolverton and S. Haile, .

105 S. S. Naghavi, A. A. Emery, H. A. Hansen, F. Zhou, V. Ozolins and C. Wolverton, *Nat. Commun.*, 2017, **8**, 285.

106 J. Vieten, B. Bulfin, P. Huck, M. Horton, D. Guban, L. Zhu, Y. Lu, K. A. Persson, M. Roeb and C. Sattler, *Energy Environ. Sci.*, 2019, **12**, 1369–1384.

107 T. Das, J. D. Nicholas and Y. Qi, *J. Mater. Chem. A*, 2017, **5**, 4493–4506.

108 D. Marrocchelli, S. R. Bishop and J. Kilner, *J. Mater. Chem. A*, 2013, **1**, 7673–7680.

109 D. S. Aidhy, B. Liu, Y. Zhang and W. J. Weber, *Comput. Mater. Sci.*, 2015, **99**, 298–305.

110 O. C. Gagné and F. C. Hawthorne, *Acta Crystallogr. Sect. B*, 2015, **71**, 562–578.

111 S. Zoller, E. Koepf, D. Nizamian, M. Stephan, A. Patané, P. Haueter, M. Romero, J. González-Aguilar, D. Lieftink, E. de Wit, S. Brendelberger, A. Sizmann and A. Steinfeld, *Joule*, 2022, **6**, 1606–1616.

112 F. Rubio-Marcos, A. Del Campo, P. Marchet and J. F. Fernández, *Nat. Commun.*, 2015, **6**, 6594.

113 N. Horchidan, A. C. Ianculescu, C. A. Vasilescu, M. Deluca, V. Musteata, H. Ursic, R. Frunza, B. Malic and L. Mitoseriu, *J. Eur. Ceram. Soc.*, 2014, **34**, 3661–3674.

114 L. L. Zhang and Y. N. Huang, *Sci. Rep.*, 2020, **10**, 1–18.

115 Z. Shao and S. M. Haile, *Nature*, 2004, **431**, 170–173.

116 N. Tsvetkov, Q. Lu, L. Sun, E. J. Crumlin and B. Yildiz, *Nat. Mater.*, 2016, **15**, 1010–1016.

117 Y. Chen, Y. Chen, D. Ding, Y. Ding, Y. Choi, L. Zhang, S. Yoo, D. Chen, B. deGlee, H. Xu, Q. Lu, B. Zhao, G. Vardar, J. Wang, H. Bluhm, E. J. Crumlin, C. Yang, J. Liu, B. Yildiz and M. Liu, *Energy Environ. Sci.*, 2017, **10**, 964–971.

118 D. Lee, R. Jacobs, Y. Jee, A. Seo, C. Sohn, A. V. Ievlev, O. S. Ovchinnikova, K. Huang, D. Morgan and H. N. Lee, *J. Phys. Chem. C*, 2017, **121**, 25651–25658.

119 A. Jun, J. Kim, J. Shin and G. Kim, *ChemElectroChem*, 2016, **3**, 511–530.

120 Y. Li, R. Gemmen and X. Liu, *J. Power Sources*, 2010, **195**, 3345–3358.

121 F. Bridges, C. H. Booth, M. Anderson, G. H. Kwei, J. J. Neumeier, J. Snyder, J. Mitchell, J. S. Gardner and E. Brosha, *Phys. Rev. B - Condens. Matter Mater. Phys.*, 2001, **63**, 214405.

122 Z. L. Wang, J. S. Yin, Y. D. Jiang and J. Zhang, *Appl. Phys. Lett.*, 1997, **70**, 3362–3364.

123 G. S. Gautam, E. B. Stechel and E. A. Carter, *Chem. Mater.*, 2020, **32**, 9964–9982.

124 X. Wang, Y. Gao, E. Krzystowczyk, S. Iftikhar, J. Dou, R. Cai, H. Wang, C. Ruan, S. Ye and F. Li, *Energy Environ. Sci.*, 2022, **15**, 1512–1528.

125 Y. Sun and S. Dai, *Sci. Adv.*, 2021, **7**, 1–24.

126 C. Oses, C. Toher and S. Curtarolo, *Nat. Rev. Mater.*, 2020, **5**, 295–309.

127 T. X. Nguyen, Y. C. Liao, C. C. Lin, Y. H. Su and J. M. Ting, *Adv. Funct. Mater.*, 2021, **31**, 2101632.

128 G. Kresse and J. Furthmüller, *Phys. Rev. B*, 1996, **54**, 11169.

129 V. Stevanović, S. Lany, X. Zhang and A. Zunger, *Phys. Rev. B - Condens. Matter Mater. Phys.*, 2012, **85**, 115104.

130 S. Tariq, A. A. Mubarak, B. Kanwal, F. Hamioud, Q. Afzal and S. Zahra, *Chinese J. Phys.*, 2020, **63**, 84–91.

131 M. T. Curnan and J. R. Kitchin, *J. Phys. Chem. C*, 2014, **118**, 28776–28790.

132 H. Tan, J. Verbeeck, A. Abakumov and G. Van Tendeloo, *Ultramicroscopy*, 2012, **116**, 24–33.

133 D. Qian, B. Xu, M. Chi and Y. S. Meng, *Phys. Chem. Chem. Phys.*, 2014, **16**, 14665–14668.

134 D. Ding, X. Li, S. Y. Lai, K. Gerdes and M. Liu, *Energy Environ. Sci.*, 2014, **7**, 552.

135 N. Mahato, A. Banerjee, A. Gupta, S. Omar and K. Balani, *Prog. Mater. Sci.*, 2015, **72**, 141–337.

136 E. R. Andrievskaya, *J. Eur. Ceram. Soc.*, 2008, **28**, 2363–2388.

137 V. Ponnilavan, A. Aravind, M. Ezhilan and S. Kannan, *Ceram. Int.*, 2019, **45**, 16450–16457.

138 C. Xiaoge, T. An, Z. Hongsong, L. Yanxu, Z. Haoming and Z. Yongde, *Ceram. Int.*, 2016, **42**, 13491–13496.

139 J. Shamblin, M. Feygenson, J. Neuefeind, C. L. Tracy, F. Zhang, S. Finkeldei, D. Bosbach, H. Zhou, R. C. Ewing and M. Lang, *Nat. Mater.*, 2016, **15**, 507–511.

140 K. E. Sickafus, R. W. Grimes, J. A. Valdez, A. Cleave, M. Tang, M. Ishimaru, S. M. Corish, C. R. Stanek and B. P. Uberuaga, *Nat. Mater. 2007 63*, 2007, **6**, 217–223.

141 K. E. Sickafus, L. Minervini, R. W. Grimes, J. A. Valdez, M. Ishimaru, F. Li, K. J. McClellan and T. Hartmann, *Science*, 2000, **289**, 748–751.

142 Z. Zhang, S. C. Middleburgh, M. De Los Reyes, G. R. Lumpkin, B. J. Kennedy, P. E. R. Blanchard, E. Reynolds and L. Y. Jang, *J. Phys. Chem. C*, 2013, **117**, 26740–26749.

143 P. S. Maram, S. V. Ushakov, R. J. K. Weber, C. J. Benmore and A. Navrotsky, *Sci. Reports 2018 81*, 2018, **8**, 1–11.

144 L. Zhou, Z. Huang, J. Qi, Z. Feng, D. Wu, W. Zhang, X. Yu, Y. Guan, X. Chen, L. Xie, K. Sun and T. Lu, *Metall. Mater. Trans. A 2015 471*, 2015, **47**, 623–630.

145 E. C. O'Quinn, C. L. Tracy, W. F. Cureton, R. Sachan, J. C. Neuefeind, C. Trautmann and M. K. Lang, *J. Mater. Chem. A*, 2021, **9**, 16982–16997.

146 C. Karthik, T. J. Anderson, D. Gout and R. Ubic, *J. Solid State Chem.*, 2012, **194**, 168–172.

147 P. E. R. Blanchard, R. Clements, B. J. Kennedy, C. D. Ling, E. Reynolds, M. Avdeev, A. P. J. Stampfl, Z. Zhang and L.-Y. Jang, *Inorg. Chem.*, 2012, **51**, 13237–13244.

148 M. Shafique, B. J. Kennedy, Y. Iqbal and R. Ubic, *J. Alloys Compd.*, 2016, **671**, 226–233.

149 S. T. Norberg, S. Hull, S. G. Eriksson, I. Ahmed, F. Kinyanjui and J. J. Biendicho, *Chem. Mater.*, 2012, **24**, 4294–4300.

150 R. Clements, J. R. Hester, B. J. Kennedy, C. D. Ling and A. P. J. Stampfl, *J. Solid State Chem.*, 2011, **184**, 2108–2113.

151 J. Shamblin, C. L. Tracy, R. I. Palomares, E. C. O'Quinn, R. C. Ewing, J. Neuefeind, M. Feygenson, J. Behrens, C. Trautmann and M. Lang, *Acta Mater.*, 2018, **144**, 60–67.

152 R. Sherrod, E. C. O'Quinn, I. M. Gussev, C. Overstreet, J. Neuefeind and M. K. Lang, *npj Mater. Degrad.*, 2021, **5**, 1–7.

153 D. L. Drey, E. C. O'Quinn, T. Subramani, K. Lilova, G. Baldinozzi, I. M. Gussev, A. F. Fuentes, J. C. Neuefeind, M. Everett, D. Sprouster, A. Navrotsky, R. C. Ewing and M. Lang, *RSC Adv.*, 2020, **10**, 34632–34650.

154 W. Hong, F. Chen, Q. Shen, Y.-H. Han, W. G. Fahrenholtz and L. Zhang, *J. Am. Ceram. Soc.*, 2019, **102**, 2228–2237.

155 S. Zhou, Y. Pu, X. Zhang, Y. Shi, Z. Gao, Y. Feng, G. Shen, X. Wang and D. Wang, *Chem. Eng. J.*, 2022, **427**, 131684.

156 Q. Yang, G. Wang, H. Wu, B. A. Beshiwork, D. Tian, S. Zhu, Y. Yang, X. Lu, Y. Ding, Y. Ling, Y. Chen and B. Lin, *J. Alloys Compd.*, 2021, **872**, 159633.

157 J. Gild, M. Samiee, J. L. Braun, T. Harrington, H. Vega, P. E. Hopkins, K. Vecchio and J. Luo, *J. Eur. Ceram. Soc.*, 2018, **38**, 3578–3584.

158 A. J. Wright, Q. Wang, Y.-T. Yeh, D. Zhang, M. Everett, J. Neuefeind, R. Chen and J. Luo, *Acta Mater.*, 2021, **235**, 118056.

159 J. Zhu, X. Meng, J. Xu, P. Zhang, Z. Lou, M. J. Reece and F. Gao, *J. Eur. Ceram. Soc.*, 2021, **41**, 1052–1057.

160 A. J. Wright, Q. Wang, C. Huang, A. Nieto, R. Chen and J. Luo, *J. Eur. Ceram. Soc.*, 2020, **40**, 2120–2129.

161 A. J. Wright, C. Huang, M. J. Walock, A. Ghoshal, M. Murugan and J. Luo, *J. Am. Ceram. Soc.*, 2021, **104**, 448–462.

162 K. Zhang, W. Li, J. Zeng, T. Deng, B. Luo, H. Zhang and X. Huang, *J. Alloys Compd.*, 2020, **817**, 153328.

163 Z. Teng, L. Zhu, Y. Tan, S. Zeng, Y. Xia, Y. Wang and H. Zhang, *J. Eur. Ceram. Soc.*, 2019, **40**, 1639–1643.

164 M. Qin, H. Vega, D. Zhang and S. Adapa, *J. Adv. Ceram.*, 2022, **11**, 641–655.

165 J. Dąbrowa, M. Stygar, A. Mikuła, A. Knapik, K. Mroczka, W. Tejchman, M. Danielewski and M. Martin, *Mater. Lett.*, 2018, **216**, 32–36.

166 M. Qin, Q. Yan, H. Wang, C. Hu, K. S. Vecchio and J. Luo, *Scr. Mater.*, 2020, **189**, 101–105.

167 M. Qin, Q. Yan, H. Wang, K. S. Vecchio and J. Luo, *J. Eur. Ceram. Soc.*, 2021, **41**, 2968–2973.

168 M. Qin, Q. Yan, Y. Liu and J. Luo, 2021, **10**, 166–172.

169 M. Qin, Q. Yan, Y. Liu, H. Wang, C. Wang, T. Lei, K. S. Vecchio, H. L. Xin, T. J. Rupert and J. Luo, *J. Eur. Ceram. Soc.*, 2021, **41**, 5775–5781.

170 E. Castle, T. Csanádi, S. Grasso, J. Dusza and M. Reece, *Sci. Rep.*, 2018, **8**, 8609.

171 Y. Qin, J. X. Liu, F. Li, X. Wei, H. Wu and G. J. Zhang, *J. Adv. Ceram.*, 2019, **8**, 148–152.

172 O. F. Dippo, N. Mesgarzadeh, T. J. Harrington, G. D. Schrader and K. S. Vecchio, *Sci. Rep.*, 2020, **10**, 21288.

173 D. Moskovskikh, S. Vorotilo, V. Buinevich, A. Sedegov, K. Kuskov, A. Khort, C. Shuck, M. Zhukovskyi and A. Mukasyan, *Sci. Rep.*, 2020, **10**, 1–8.

174 X. Chen and Y. Wu, *J. Am. Ceram. Soc.*, 2019, **103**, 750–756.

175 A. J. Wright and J. Luo, *J. Mater. Sci.*, 2020, **55**, 9812–9827.

176 H. Xiang, Y. Xing, F. zhi Dai, H. Wang, L. Su, L. Miao, G. Zhang, Y. Wang, X. Qi, L. Yao, H. Wang, B. Zhao, J. Li and Y. Zhou, *J. Adv. Ceram.*, 2021, **10**, 385–441.

177 S. Shivakumar, M. Qin, D. Zhang, C. Hu, Q. Yan and J. Luo, *Scr. Mater.*, 2022, **212**, 114557.

178 A. J. Wright, Q. Wang, C. Hu, Y. T. Yeh, R. Chen and J. Luo, *Acta Mater.*, 2021, **211**, 116858.

179 D. Zhang, Y. Chen, T. Feng, D. Yu, K. An, R. Chen and J. Luo, *Scr. Mater.*, 2022, **215**, 114699.

180 B. Jiang, C. A. Bridges, R. R. Unocic, K. C. Pitike, V. R. Cooper, Y. Zhang, D. Y. Lin and K. Page, *J. Am. Chem. Soc.*, 2021, **143**, 4193–4204.

181 K. An, Y. Chen and A. D. Stoica, *MRS Bull.*, 2019, **44**, 878–885.

182 Rice RW., *Porosity of ceramics: properties and applications*, CRC Press, 1998.

183 D. B. Miracle and O. N. Senkov, *Acta Mater.*, 2017, **122**, 448–511.

184 J. W. Yeh, *Jom*, 2013, **65**, 1759–1771.

185 Y. Zhang, T. T. Zuo, Z. Tang, M. C. Gao, K. A. Dahmen, P. K. Liaw and Z. P. Lu, *Prog. Mater. Sci.*, 2014, **61**, 1–93.

186 C. Heremans, B. J. Wuensch, J. K. Stalick and E. Prince, *J. Solid State Chem.*, 1995, **117**, 108–121.

187 A. F. Fuentes, S. M. Montemayor, M. Maczka, M. Lang, R. C. Ewing and U. Amador, *Inorg. Chem.*, 2018, **57**, 12093–12105.

188 E. Reynolds, P. E. R. Blanchard, Q. Zhou, B. J. Kennedy, Z. Zhang and L. Y. Jang, *Phys. Rev. B - Condens. Matter Mater. Phys.*, 2012, **85**, 1–5.

189 V. Kocevski, G. Pilania and B. P. Uberuaga, *Front. Chem.*, 2021, **9**, 1–10.

190 C. L. Farrow, P. Juhas, J. W. Liu, D. Bryndin, E. S. Boin, J. Bloch, T. Proffen and S. J. L. Billinge, *J. Phys. Condens. Matter*, 2007, **19**, 335219.

191 G. Pilania, B. Puchala and B. P. Uberuaga, *npj Comput. Mater.*, 2019, **5**, 1–9.

192 E. C. O'quinn, K. E. Sickafus, R. C. Ewing, G. Baldinozzi, J. C. Neuefeind, M. G. Tucker, A. F. Fuentes, D. Drey and M. K. Lang, *Sci. Adv*, 2020, **6**, ebac2758.

193 D. Drey, E. O'Quinn, S. Finkeldei, J. Neuefeind and M. Lang, *Acta Mater.*, 2021, **225**, 117590.

194 F. P. Marlton, Z. Zhang, Y. Zhang, T. E. Proffen, C. D. Ling and B. J. Kennedy, *Chem. Mater.*, 2021, **33**, 1407–1415.

195 S. Il Kim, K. H. Lee, H. A. Mun, H. S. Kim, S. W. Hwang, J. W. Roh, D. J. Yang, W. H. Shin, X. S. Li, Y. H. Lee, G. J. Snyder and S. W. Kim, *Science*, 2015, **348**, 109–114.

196 S. H. Oh, R. Black, E. Pomerantseva, J. H. Lee and L. F. Nazar, *Nat. Chem.*, 2012, **4**, 1004–1010.

197 K. E. Sickafus, L. Minervini, R. W. Grimes, J. A. Valdez, M. Ishimaru, F. Li, K. J. McClellan and T. Hartmann, *Science (80-.).*, 2000, **289**, 748–751.

198 J. Shamblin, C. L. Tracy, R. I. Palomares, E. C. O'Quinn, R. C. Ewing, J. Neuefeind, M. Feygenson, J. Behrens, C. Trautmann and M. Lang, *Acta Mater.*, 2018, **144**, 60–67.

199 M. A. Subramanian, G. Aravamudan and G. V. Subba Rao, *Prog. Solid State Chem.*, 1983, 15, 55–143.

200 C. Wan, Z. Qu, A. Du and W. Pan, *J. Am. Ceram. Soc.*, 2011, **94**, 592–596.

201 Y. H. Lee, H. S. Sheu, J. P. Deng and H. C. I. Kao, *J. Alloys Compd.*, 2009, **487**, 595–598.

202 Y. Liu, R. L. Withers and L. Norén, *J. Solid State Chem.*, 2004, **177**, 4404–4412.

203 K. Ren, Q. Wang, G. Shao, X. Zhao and Y. Wang, *Scr. Mater.*, 2020, **178**, 382–386.

204 L. Chen, J. Guo, Y. Zhu, M. Hu and J. Feng, *J. Am. Ceram. Soc.*, 2020, **104**, 404–412.

205 L. Chen, Y. Wang, M. Hu, L. Zhang, J. Wang, Z. Zhang, X. Liang, J. Guo and J. Feng, *Appl. Phys. Lett.*, 2021, **118**, 071905.

206 F. Li, L. Zhou, J.-X. Liu, Y. Liang and G.-J. Zhang, *J. Adv. Ceram.*, 2019, 1–7.

207 H. Junjie, H. Guo, L. Jing and T. Jingchao, *J. Eur. Ceram. Soc.*, 2021, **41**, 6080–6086.

208 L. Zhou, F. Li, J. X. Liu, Q. Hu, W. Bao, Y. Wu, X. Cao, F. Xu and G. J. Zhang, *J. Eur. Ceram. Soc.*, 2020, **40**, 5731–5739.

209 C. M. Rost, E. Sachet, T. Borman, A. Moballegh, E. C. Dickey, D. Hou, J. L. Jones, S. Curtarolo and J. P. Maria, *Nat. Commun.*, 2015, **6**, 8485.

210 H. Chen, Z. Zhao, H. Xiang, F. Z. Dai, J. Zhang, S. Wang, J. Liu and Y. Zhou, *J. Mater. Sci. Technol.*, 2020, **38**, 80–85.

211 J. Wu, X. Wei, N. P. Padture, P. G. Klemens, M. Gell, E. García, P. Miranzo and M. I. Osendi, *J. Am. Ceram. Soc.*, 2002, **85**, 3031–3035.

212 J. E. Greedan, D. Gout, A. D. Lozano-Gorrin, S. Derahkshan, T. Proffen, H.-J. Kim, E. Božin and S. J. L. Billinge, *Phys. Rev. B*, 2009, **79**, 014427.

213 B. J. Kennedy, *J. Solid State Chem.*, 1996, **123**, 14–20.

214 I. M. Gussev, E. C. O'Quinn, G. Baldinozzi, J. Neuefeind, R. C. Ewing, F. Zhang and M. Lang, *Acta Mater.*, 2020, **196**, 704–709.